

University of Alberta

Library Release Form

NAME OF AUTHOR: Martin Snajdr

TITLE OF THESIS: Interaction of Cosmic Strings and
Branes with Black Holes

DEGREE: Doctor of Philosophy

YEAR THIS DEGREE GRANTED: 2003

Permission is hereby granted to the University of Alberta Library to reproduce single copies of this thesis and to lend or sell such copies for private, scholarly or scientific research purposes only.

The author reserves all other publication and other rights in association with the copyright in the thesis, and except as hereinbefore provided neither the thesis nor any substantial portion thereof may be printed or otherwise reproduced in any material form whatever without the author's prior written permission.

Martin Snajdr
Dept. of Physics
412, Avadh Bhatia Physics Laboratory
University of Alberta
Edmonton, AB
Canada T6G 2J1

University of Alberta

**Interaction of Cosmic Strings and Branes with Black
Holes**

by

Martin Snajdr

A thesis submitted to the Faculty of Graduate Studies and Research in partial
fulfillment of the requirements for the degree of Doctor of Philosophy

Department of Physics

Edmonton, Alberta

2003

University of Alberta

Faculty of Graduate Studies and Research

The undersigned certify that they have read, and recommend to the Faculty of Graduate Studies and Research for acceptance, a thesis entitled **Interaction of Cosmic Strings and Branes with Black Holes** submitted by **Martin Snajdr** in partial fulfillment of the requirements for the degree of Doctor of Philosophy.

Dr. V.P. Frolov (Supervisor)

Dr. R. Marchand (Chair)

Dr. M.W. Choptuik (External)

Dr. B.A. Campbell

Dr. D.N. Page

Dr. E. Woolgar

DATE:

Abstract

In this thesis we investigate the interaction of cosmic strings and branes with black holes. First, the scattering of a straight, infinitely long cosmic string by a rotating black hole is considered. We assume that a string is moving with velocity v and that initially the string is parallel to the axis of rotation of the black hole. We demonstrate that as a result of scattering, the string is displaced in the direction perpendicular to the velocity by an amount $\kappa(v, b)$, where b is the impact parameter. The late-time solution is represented by a kink and anti-kink, propagating in opposite directions with the speed of light, leaving behind them the string in a new “phase”. We present the results of the numerical study of the string scattering and their comparison with the weak field approximation, valid where the impact parameter is large, $b/M \gg 1$, and also with the scattering by a non-rotating black hole which was studied in earlier works. Next we study critical scattering and capture of a cosmic string — we demonstrate that there exists a critical value of the impact parameter $b_c(v)$ which separates scattering from the capture regime. Using numerical simulations we obtain the critical impact parameter curve for different values of the rotation parameter a . We show that for the prograde motion of the string this curve lies below the curve for

the retrograde motion. Moreover, for ultrarelativistic strings moving in the prograde direction and nearly extremal black holes the critical impact parameter curve is found to be a multiply valued function of v . We obtain real-time profiles of the scattered strings in the regime close to the critical. We also study the relativistic and ultrarelativistic regime, especially such effects as coil formation and wrapping effect. Finally, we analyse the interaction of an n -dimensional topological defect (n -brane) described by the Nambu-Goto action with a higher-dimensional Schwarzschild black hole moving in the bulk spacetime. We derive the general form of the perturbation equations for an n -brane in the weak field approximation and solve them analytically in the most interesting cases. We specially analyze applications to brane world models. We calculate the induced geometry on the brane generated by a moving black hole. From the point of view of a brane observer, this geometry can be obtained by solving $(n + 1)$ -dimensional Einstein's equations with a non-vanishing right hand side. We calculate the effective stress-energy tensor corresponding to this 'shadow-matter'. We explicitly show that there exist regions on the brane where a brane observer sees an apparent violation of energy conditions. We also study the deflection of light propagating in the region of influence of this 'shadow matter'.

Acknowledgements

It has been a great pleasure to work under the supervision of Dr. Valeri Frolov who offered me a great project to work on and guided me throughout my studies. I would also like to thank Dr. Don Page for sharing his insights into the problematic of black holes and cosmic strings. I have very much enjoyed discussions with Dr. Dejan Stojkovic about all sorts of topics. My thanks go to the teachers of all the courses I have the privilege to attend. Last but not least I would like to thank Ron Senda and the Computer and Network Services research support group of the University of Alberta for allowing me to access the CNS and MACI/Westgrid computer infrastructure.

Table of Contents

Abstract

Acknowledgements

Table of Contents

List of Tables

List of Figures

1	Introduction	1
2	Physics of Topological Defects	8
2.1	General Theory	8
2.2	Cosmic Strings	12
2.2.1	Global strings	13
2.2.2	Local strings	14
2.3	Domain Walls	16
2.4	The Nambu-Goto Effective Action	17
2.5	Dynamics of Topological Defects	19
2.6	Cosmic Strings in Cosmology	20

TABLE OF CONTENTS

3	Cosmic Strings in Kerr Geometry	27
3.1	Kerr Geometry	27
3.2	Cosmic String Scattering	29
3.2.1	Weak field approximation to the scattering of a string moving in a Kerr spacetime	29
3.2.2	Scattering of particles by a Kerr black hole	37
3.2.3	Initial and boundary conditions	38
3.2.4	Solving dynamical equations and constraints	40
4	Scattering of Cosmic String by a Rotating Black Hole: Strong Field Regime	42
4.1	String Profiles for Strong Field Scattering	43
4.1.1	General picture	43
4.1.2	“Real-time profiles” of the string for strong field scattering	46
4.2	Late Time Scattering Data	46
4.2.1	Displacement parameter	46
4.2.2	Form of the kinks	54
5	Critical Scattering and Capture	58
5.1	String Capture and Critical Impact Parameter	59
5.2	Critical Scattering	64
5.2.1	Real-time string profiles	64
5.2.2	Late time scattering data	68
5.3	Coil Formation	71
6	Interaction of a Brane with a Moving Bulk Black Hole	77
6.1	Brane Worlds and Large Extra Dimensions	79
6.2	Higher-dimensional Non-rotating Black Holes	81

TABLE OF CONTENTS

6.3	A Moving Flat Brane in a Spacetime with a Fixed Point	83
6.4	Brane Perturbation Equations of Motion. Gauge Fixing	86
6.5	Solutions of the Brane Perturbation Equations	89
6.5.1	Generators of solutions	89
6.5.2	Generating solutions for $n = 3$ brane	90
6.5.3	Energy loss	92
6.6	‘Shadow Matter’ Effect	95
6.7	Deflection of Light	99
7	Conclusions and Discussions	103
7.1	Summary of Findings	103
7.2	Future Research	107
A	Details of the Numerical Scheme	108
A.1	Coordinate Choice	108
A.2	Discretization of the Equations of Motion	109
A.3	Structure of the Numerical Grid	112
A.3.1	Mesh refinement for non-critical scattering	113
A.3.2	Mesh refinement for capture and critical scattering	114
A.3.3	Practical implementation of adaptive mesh refinement	115
A.4	Calculating κ_1 and κ_2	118
A.5	Obtaining the Real-time Profiles	120
B	Spherically-Symmetric Solutions of D’Alambert Equation	124
	Bibliography	127

List of Tables

- 4.1 Values of fitted parameters from equation (4.2.12) and (4.2.13) . 53

List of Figures

1.1	A straight cosmic string scattered by a black hole.	5
2.1	$\ell(\ell + 1)c_\ell/2\pi$ versus ℓ for three different models.	25
3.1	Y -profile for Newtonian scattering	34
3.2	Y -profile for Lense-Thirring scattering	36
3.3	Initial setup for prograde and retrograde string motion. The part of the string depicted by the dashed line lies below the XY -plane.	39
3.4	Scheme of time domains for scattering problem	40
4.1	Displacement in Y -direction as a function of (τ, σ) for given ve- locity $v/c = 0.762$ in the weak (a) and strong (b-d) field regime. .	43
4.2	“Real-time profiles” of the string and their XZ - and YZ - pro- jection for the strong field scattering by the Schwarzschild black hole.	44
4.3	“Real-time profiles” of the string and their XZ - and YZ - pro- jection for the strong field retrograde scattering by the extremal Kerr black hole.	45
4.4	“Real-time profiles” of the string and their XZ - and YZ - pro- jection for the strong field prograde scattering by the extremal Kerr black hole.	45

LIST OF FIGURES

4.5	Displacement parameter κ as a function of the impact parameter b for different velocities $v/c = 0.762$	47
4.6	Displacement parameter κ as a function of the impact parameter b for $v/c = 0.964$	48
4.7	Displacement parameter κ as a function of the impact parameter b for $v/c = 0.995$	48
4.8	Plot of κ_1 for different velocities v and impact parameters b . The straight lines represent a linear fit.	52
4.9	Plot of κ_2 for different velocities v and impact parameters b . The straight lines represent a linear fit.	53
4.10	Plot of κ_1/κ for different velocities v and impact parameters b . The straight lines represent a linear fit.	54
4.11	Profiles of the kinks for different impact parameters	56
4.12	Comparison of kink widths for $v/c = 0.462, 0.762, 0.964, 0.995$ and impact parameters $b/M = 9, 12, 15, 18, 25, 40$ obtained from simulation (circles) and the analytic approximation (4.2.15). The data shown are taken for $a/M = 0$	57
5.1	Critical impact parameter b_c as a function of the string's initial velocity v . The solid line represents Page's approximation for Schwarzschild black hole (formula (5.1.2)).	60
5.2	Critical impact parameter b_c and its fitted approximation b_c^{fit} as functions of the string's initial velocity v for different values of the rotation parameter a/M	62
5.3	Critical impact parameter curve for a prograde scattering of a relativistic cosmic string by a rapidly rotating black hole.	63
5.4	Real-time profiles of the cosmic string: $v/c = 0.995, a/M = 1$ and $b/M = 2.9$	65

LIST OF FIGURES

5.5	Real-time profiles of the cosmic string: $v/c = 0.995$, $a/M = 1$ and $b/M = 2.55$	66
5.6	Real-time profiles of the cosmic string: $v/c = 0.995$, $a/M = 1$ and $b/M = 2.4125$	67
5.7	Late time profiles of the cosmic string: $v/c = 0.995$, $a/M = 1$ and $b/M = 2.9$, $T/M = 7446.47$	68
5.8	Late time profiles of the cosmic string: $v/c = 0.995$, $a/M = 1$ and $b/M = 2.55$, $T/M = 7448.56$	69
5.9	Late time profiles of the cosmic string: $v/c = 0.995$, $a/M = 1$ and $b/M = 2.4125$, $T/M = 4991.53$	70
5.10	Late time profiles of the cosmic string: $v/c = 0.995$, $a/M = 0$ and $b/M = 5.17$, $T/M = 5209.56$	71
5.11	Coil formation regions for prograde and retrograde scattering of the string.	76
6.1	It is equivalent to integrate over the two regions on the left as it is to integrate over the one region on the right.	91
6.2	Plot of χ_- for $\beta = 1$, $R_0 = 1$, $b = 10$, $k = 2$	92
6.3	Plot of χ_+ for $\beta = 1$, $R_0 = 1$, $b = 10$, $k = 2$	93
6.4	Asymptotic shape of the fields Φ_- and Φ_+	94
6.5	Plots of the components of the Einstein tensor of the induced geometry on the brane. The parameters are $R_0 = 1$, $\beta = 1$, $b = 10$, $k = 2$	98
A.1	An example of a (non-uniform) grid. It highlights three grid points (marked by a cross) together with all the points needed for the calculation of the derivatives (marked by full circles).	111
A.2	Structure of the numerical grid	113

LIST OF FIGURES

A.3 Part of the numerical grid showing the $T = T_{\text{save}} = \text{const}$ line and
the points stored in AS and AX at this time step. 121

A.4 The left profile represents a part of the string with all the grid
points while the right profile represents the approximation with
smaller number of grid points. In reality, of course, the string has
a three-dimensional structure. 123

Chapter 1

Introduction

The thesis consists of two related parts. In the first part we study different aspects of interactions of cosmic strings with rotating black holes. In the second part we study an interaction of a brane with higher-dimensional black hole in the framework of recently proposed models of gravity in a spacetime with large extra dimensions. In both cases we use similar methods that allow us to discover interesting new physical effects.

The study of cosmic strings and other topological defects and their motion in an external gravitational field is an interesting problem. Cosmic strings are topologically stable one-dimensional objects which are predicted by unified theories. Cosmic strings (as well as other topological defects) may appear during a phase transition in the early universe. A detailed discussion of cosmic strings and other topological defects can be found in the book by Shellard and Vilenkin [1]. Cosmic strings are naturally predicted by many realistic models of particle physics. The formation of cosmic strings helps to successfully exit the inflationary era in a number of the inflation models motivated by particle physics [2, 3]. The formation of cosmic strings is also predicted in most classes of superstring compactification involving the spontaneous breaking of a pseudo-anomalous $U(1)$

gauge symmetry (see e.g. [4] and references therein). Recent measurements of the Cosmic Microwave Background (CMB) anisotropy and especially the position of the acoustic peaks exclude some of the earlier proposed scenarios where the cosmic strings are the main origin of CMB fluctuations. On the other hand, recent analysis shows that a mixture of inflation and topological defects is consistent with current CMB data [5–9].

Recent astrophysical observations give strong evidence of the existence stellar mass and supermassive black holes (see, e.g., [10, 11] and [12] for a review). There is also growing evidence, although much weaker, for the existence of intermediate-size black holes (see, e.g., [13] for a review). In this thesis we study the interaction of cosmic strings and other topological defects with a black hole.

A black hole interacting with a cosmic string is a quite rare example of interaction of two relativistic non-local gravitating systems which allows rather complete analysis. This makes this system interesting from pure theoretical point of view. From more "pragmatic" viewpoint, this system might be a strong source of gravitational waves. But in order to be able to study this effect one needs first to obtain information on the motion of the string in the black hole background. The situation here is very similar to the case of gravitational radiation from bodies falling into a black hole.

This thesis is based on the publications [14–16]. It is organized as follows.

Chapter 1 provides an introduction to the subjects studied in this thesis and fixes the notation used later on.

In **chapter 2** we give a general introduction to the physics of topological defects focusing in more details on cosmic strings. We also review the present status of cosmic strings in cosmology.

In **chapters 3,4 and 5** we study in detail the interaction of cosmic strings with black holes. We focus mainly on effects connected with the rotation of the

black hole. The scattering and capture of a cosmic string by a *non-rotating* black hole was previously studied both numerically and analytically [17–22].

In our setup of the problem we use the thin string approximation and neglect its gravitational back reaction. This approximations are expected to be very good for the following reasons. If η is a characteristic energy scale of a phase transition responsible for a string formation then the thickness of a string is $\rho \sim \eta^{-1}$ while its dimensionless mass per unit length parameter $\mu^* = G\mu/c^2 \sim \eta^2$. For example, for GUT strings $\rho_{GUT} \approx 10^{-29}\text{cm}$ and $\mu_{GUT}^* \approx 10^{-6}$, and for the electroweak phase transitions $\rho_{EW} \approx 10^{-14}\text{cm}$ and $\mu_{EW}^* \approx 10^{-34}$. Since $\mu^* \ll 1$ one can neglect (at least in the lowest order approximation) effects connected with gravitational wave radiation during the scattering of the string by a black hole.

In our setup we also assume that the size of the string is much larger than the Schwarzschild gravitational radius $r_S = 2GM/c^2$ of a black hole and its total mass is much smaller than the black hole mass. The latter condition together with $\mu^* \ll 1$ means that we can consider a string as a test object. In order to specify the scattering problem we consider the simplest setup, with the string initially far away from the black hole, so that the string has the form of a straight line. We assume that the string is initially moving with velocity v towards the black hole and is lying in the plane parallel to the rotation axis of the black hole. This plane is located at a distance b with respect to the parallel “plane” passing through the rotation axis. In analogy with particle scattering we call b the *impact parameter*.

Chapter 3 provides a general framework which is common for the consequent two chapters. For $b \gg r_S$ the string moves in the region where the gravitational potential GM/r is always small, and one can use a weak field approximation where the string equation of motion can be solved analytically [19, 20, 22]. The

weak field approximation is reviewed in the last section of chapter 3. We include analysis of Lense-Thirring scattering, i.e., scattering due to the linear angular momentum term in Kerr metric.

String scattering can be described in qualitative terms. In the reference frame of the string the gravitational field of the black hole is time dependent and it excites the string's transversal degrees of freedom. This effect occurs mainly when the central part¹ of the string passes close to the black hole. Since information is propagating along the string with the velocity of light, there always exist two distant regions, 'right' and 'left', which have not yet felt this excitation. These asymptotic regions of the string continue their motion in the initial plane ('old phase'). After scattering, when string is moving again far from the black hole, its central part moves in a plane which is parallel to the initial plane but is shifted towards the black hole by a distance κ ('new phase'). There exist two symmetric kink-like regions separating the 'new' phase from the 'old' one. These kinks move out of the central region with the velocity of light and preserve their form. Besides the amplitude κ , the kinks are characterized by a width w which depends on the impact parameter and the initial velocity of the string. Figure 1.1 schematically illustrates this behavior².

In **chapter 4** we analyze the scattering of a cosmic string by a rotating black hole in the strong field regime. Our focus is to obtain the quantities κ and w , and to study how black hole rotation modifies the earlier results for a non-rotating black hole presented in [19]. We present the results for string spacetime evolution, real profiles of a string at different external observer times T , as well as asymptotic scattering data.

When a cosmic string, in its motion, passes close to a black hole it can be

¹We call center of the string the center of the symmetry $Z \rightarrow -Z$.

²The figure is taken from [21]. In the picture the quantity we call κ is labeled as A_∞ . The rotational axis of the black hole is parallel to the straight string.

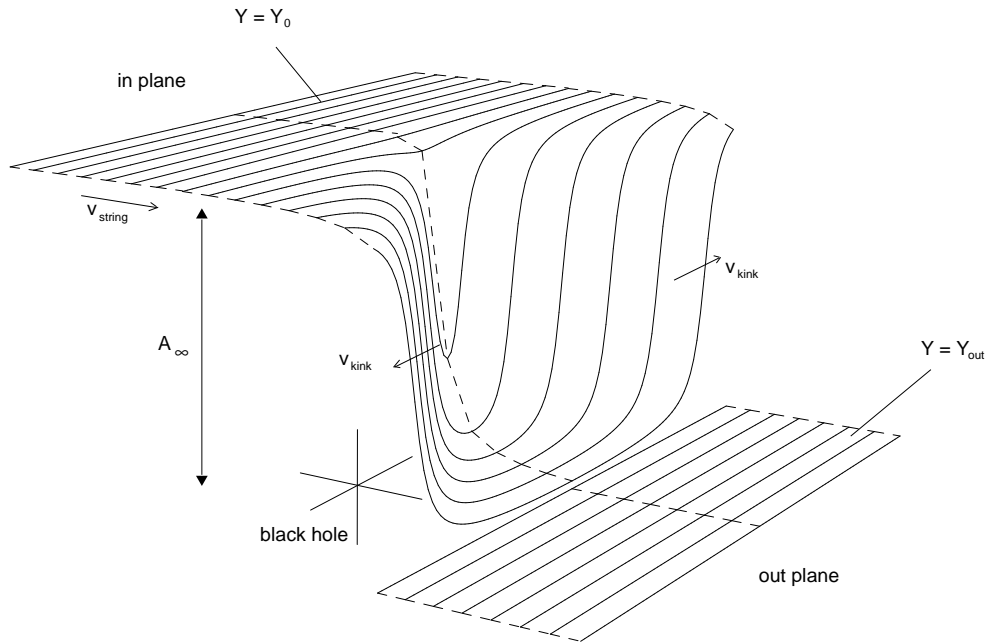


Figure 1.1: A straight cosmic string scattered by a black hole.

captured. In **chapter 5** we study this phenomenon. For a given velocity v there exists a critical value of the impact parameter, $b_c(v)$, which separates capture and scattering regimes.

Using numerical simulations we obtain the critical impact parameter curve $b_c(v)$ for different values of the rotation parameter a . We show that for prograde motion of the string this curve lies below the curve for the retrograde motion³. Moreover, for ultrarelativistic strings moving in the prograde direction in a space-time of nearly extremal black holes the critical impact parameter curve is found to be a multiply valued function of v .

As we shall show, scattering of strings with impact parameters slightly greater than b_c has a number of interesting features. We call this regime *critical scattering*. We obtain real time profiles of scattered strings in the regime close to

³See section 3.2.2 for explanation of terms *prograde* and *retrograde*.

the critical. We also study critical scattering and capture in the relativistic and ultrarelativistic regimes and especially such relativistic effects as coil formation and wrapping effect.

In **chapter 6** the methods developed for the string scattering problem are generalized to the case when a topological defect (brane) has more than one spatial dimension and is moving in a higher-dimensional bulk spacetime with a black hole. This problem is technically very similar to the cosmic string scattering. On the other hand it has interesting applications to the so-called brane world models.

It was proposed recently that the whole universe could just be a three-dimensional domain wall (brane) embedded in a higher dimensional space with large or infinite extra dimensions. In these models, all the standard model particles are localized on the brane while gravity can propagate everywhere. In particular, black holes being gravitational solitons can propagate in a higher dimensional bulk space. One possible mechanism for the particle localization was proposed in [23], where it was shown that fermion interaction with a scalar domain wall (in five dimensions) can lead to localizations of chiral fermions.

In our approach we generalize the weak field approximation scheme developed for cosmic strings to a case where both a brane and a bulk space in which the brane is moving may have an arbitrary number of dimensions. We use the Nambu-Goto action to describe the motion of the higher-dimensional brane. We study the motion of such $(n+1)$ -dimensional object in a background of $(n+k+1)$ -dimensional Schwarzschild black hole.

We will keep our analysis as general as possible, however we will devote special attention to the so-called brane world model in which the brane has three spatial dimensions while the number of bulk dimensions is arbitrary.

Finally, in **chapter 7** we summarize the results and suggest potential direc-

tions for future research.

Throughout the thesis we use units in which $c = \hbar = G_N = 1$ and the metric sign convention of Misner, Thorne, and Wheeler [24] $(-1, 1, 1, 1)$ or its higher-dimensional equivalent.

In general, capital Latin letters (A, B, \dots) are reserved for indices of quantities related to bulk space, whereas Greek indices (μ, ν, \dots) are used for quantities restricted to the n -brane. The following list provides some examples:

$X^A(x^\mu)$	parametric description of an n -brane or cosmic string
g_{AB}	metric of the bulk space
$\Gamma^A_{BC}, \Gamma_{ABC}$	Christoffel symbols for the bulk metrics
$\gamma_{\mu\nu}$	induced metric on a brane or string

Chapter 2

Physics of Topological Defects

The first part of this chapter reviews the basic theory of topological defects, focusing mainly on cosmic strings. We then introduce the Nambu-Goto effective action which is the leading approximation governing the dynamics of topological defects. Finally, we review the present status of the role of cosmic strings in cosmology.

2.1 General Theory

Quantum field theories generally possess two kind of symmetries: spacetime and internal. The former are associated with the symmetries of the four-dimensional spacetime manifold, and are described by the Poincaré group. The latter can be considered as those relating fields to each other. They are characterized by a compact Lie group.

The most important internal symmetries are local (gauge) symmetries, i.e., those that depend on spacetime location. All gauge theories require spin 1 fields in order to cancel the extra derivative terms arising due to the local character of the transformation. However, in order for this to work, the spin 1 fields must be

massless. This is in disagreement with observation — the mediators of the weak interaction W^+, W^-, Z^0 are massive.

The solution to this problem is the Higgs mechanism. It introduces masses to the gauge fields by spontaneously breaking the symmetry of the vacuum. A necessary ingredient is a spin 0 Higgs field, which at certain critical temperature acquires a non-vanishing vacuum expectation value (VEV) ¹. The theory is then invariant only under the subgroup of G which leaves the vacuum unchanged. We say that G is broken into H ($G \rightarrow H$).

The new ground state of the theory is a uniform non-zero field $\Phi(x) = \Phi_0$. There are, however, other conceivable (more energetic) configurations containing regions where the Higgs field vanishes. These highly energetic regions form the core of the topological effects. Whether such configurations are stable or not depends on the topology of the vacuum manifold.

The type of defect we get for a particular case depends on the internal dimension n and the spatial dimension. In three-dimensional space there are four different possibilities

- **n = 1.** *Domain Walls.* The symmetry is discrete. Space is divided into regions in different phases separated by walls of false vacuum.
- **n = 2.** *Strings.* Linear defects characterized by their mass per unit length.
- **n = 3.** *Monopoles.* Massive point-like defects. The field points radially outward from the defect.
- **n = 4.** *Textures.* These defects are not well localized in space. They do not possess a core of false vacuum and their energy originates from the field gradients.

¹The coupling constants in the effective Lagrangian are temperature dependent.

To be more concrete, let us consider a gauge theory with a scalar field Φ acted upon by a gauge symmetry group G , with hermitian generators T_a such that

$$[T_a, T_b] = if_{abc}T_c . \quad (2.1.1)$$

The question is whether strings-like defects can form, i.e., whether there is a stable axisymmetric static solution of the field equations with finite energy per unit length². This means that we assume the field configuration to be independent of X^0, X^3 , with $A_0^a = A_3^a = 0$.

The energy density has the form

$$\mathcal{E} = \int d^2X \left(\frac{1}{4} F_{ij}^a F_{ij}^a + |D_k \Phi|^2 + V(\Phi) \right), \quad (2.1.2)$$

where $F_{ij}^a = \partial_i A_j^a - \partial_j A_i^a - ef^{abc} A_i^b A_j^c$ and $D_k = \partial_k + ieA_k$, with $A_k = A_k^a T_a$ (we also absorbed a factor of $\sqrt{4\pi}$ into the field strengths). The potential is generally a quartic function of Φ , and we can always set $V = 0$ at its minimum.

Let M be the vacuum manifold and Φ_0 a point on it. Gauge invariance asserts that

$$g\Phi_0 = \Phi', \quad g \in G, \Phi' \in M . \quad (2.1.3)$$

Let H be the subgroup³ which leaves Φ_0 invariant, i.e., $h\Phi_0 = \Phi_0$.

Then to each element Φ of M we can assign an equivalence class $[g] \in G/H$ such that

$$\Phi = g\Phi_0 . \quad (2.1.4)$$

Each two elements $g', g'' \in [g]$ “differ” only by some element $h \in H$, i.e., $g' = g''h$. The opposite is also true — each equivalence class corresponds to one point of

²As it will be explained in the next section these types of strings belong to a class of so-called local strings.

³It is trivial to check that H is indeed a group.

M . This establishes an isomorphism from M to G/H which we denote by writing

$$M = G/H . \quad (2.1.5)$$

In order to have a finite energy solution of (2.1.2), we demand that each term of the integrand must approach zero sufficiently fast as $\rho \rightarrow \infty$ (we use standard polar coordinates (ρ, φ) in the X^1X^2 -plane). From $V(\rho, \varphi) \xrightarrow{\rho \rightarrow \infty} 0$ it follows that the scalar field at infinity $\Phi_\infty(\varphi) \in M$ and hence

$$\Phi_\infty(\varphi) = g(\varphi)\Phi(0) = g(\varphi)\Phi_0, \quad \Phi_0 \in M, \quad g(\varphi) \in G . \quad (2.1.6)$$

Vanishing of $F_{ij}^a F_{ij}^a$ implies that A_k at infinity must be just a gauge transformed vacuum

$$A_k(x) \longrightarrow \frac{i}{e} \partial_k g(\varphi) g^{-1}(\varphi) \quad \text{as } \rho \rightarrow \infty . \quad (2.1.7)$$

Finally, from the condition $D_k \Phi \xrightarrow{\rho \rightarrow \infty} 0$ we have

$$\partial_k \Phi_\infty(\varphi) - \partial_k g'(\varphi) g'^{-1}(\varphi) \Phi_\infty(\varphi) = 0 . \quad (2.1.8)$$

Substituting (2.1.6) into (2.1.8) we get

$$(\partial_k g(\varphi)) \Phi_0 = (\partial_k g'(\varphi)) g'^{-1}(\varphi) g(\varphi) \Phi_0 , \quad (2.1.9)$$

which is clearly satisfied if $g'(\varphi) = g(\varphi)$. It is convenient to set $g(0) = \mathbf{e}$ (the identity element).

We also demand that $\Phi_\infty(2\pi) = \Phi_\infty(0)$, which implies $g(2\pi) \in H$. $\Phi_\infty(\varphi)$ then defines a closed loop in M , or, equivalently, $[g(\varphi)]$ defines a closed loop in G/H .

If all loops in M are smoothly contractable to a point (Φ_0), then the vortex solution is not stable, and dynamically “decays” into the true vacuum. If, however, there are non-contractable loops in M , Φ cannot reach the ground state without

going through a state with infinite energy. In other words, there is an infinite energy “barrier” which stabilizes the vortex solution on topological grounds.

In mathematics, non-contractable loops at a point $\Phi \in M$ are classified by the elements of the fundamental group (also known as the first homotopy group $\pi_1(\Phi, M)$). If M is a connected manifold, π_1 is independent of the point Φ . Thus $\pi_1(M)$ contains information about the global structure of the manifold.

We say that two loops are homotopic if they can be smoothly transformed into each other. Homotopic loops form equivalence classes with a group structure (identity is the class of loops contractable to a point, inverse element is the class of loops traversed in reverse direction, and the product is defined by traveling the two loops in succession).

If $\pi_1(M)$ is trivial, i.e., contains only the identity, we say that M is simply connected. Otherwise it is multiply connected. Since Lie groups are also manifolds, the homotopy theory is also applicable to them.

There is a useful theorem which says that if the gauge group G is simply connected, then $\pi_1(M) = \pi_0(H)$, where $\pi_0(H)$ “counts” the number of disconnected pieces of H (this theorem can be generalized for higher homotopy groups).

2.2 Cosmic Strings

In this section we take a closer look at the two most basic classes of strings — global and local strings. We will see that global strings have infinite energy per unit length and thus are not very realistic. Local strings, on the other hand, have finite energy per unit length and are very well localized in space. In the following chapters we will always consider local strings as our model.

Global and local strings are not by far the only permitted type of strings. There is a whole “ZOO” of theories with a string solution. The most studied are semilocal strings (only a subgroup of the global symmetry is gauged) and

superconducting bosonic and fermionic strings (carrying the appropriate current in their cores).

2.2.1 Global strings

Global strings arise from theories invariant under global transformations. The simplest such theory is described by Lagrangian density

$$L = -\partial_A \Phi^* \partial^A \Phi - V(\Phi), \quad V = \frac{1}{2} \lambda (|\Phi|^2 - \frac{1}{2} \eta^2)^2, \quad (2.2.10)$$

where Φ is a complex scalar field. This theory is clearly invariant under global $U(1)$ transformations $\Phi \rightarrow e^{i\alpha} \Phi$.

The Euler-Lagrange equation of motion for the field is

$$[\nabla^2 + \lambda(|\Phi|^2 - \frac{1}{2} \eta^2)] \Phi = 0. \quad (2.2.11)$$

The ground state is given by

$$\Phi_0 = \frac{\eta}{\sqrt{2}} \exp(i\alpha_0), \quad \alpha_0 \in \mathbb{R} \quad (2.2.12)$$

therefore the vacuum manifold is topologically equivalent to a circle S^1 . The first homotopy group $\pi_1(S^1)$ is non-trivial

$$\pi_1(S^1) = \mathbb{Z}. \quad (2.2.13)$$

Each homotopy class is labeled by an integer number n called the winding number. It counts how many times the loop “wraps” around the circle S^1 .

It is convenient to work in cylindrical coordinates (ρ, φ, z) in which our ansatz for the solution has the form

$$\Phi = \frac{\eta}{\sqrt{2}} f(\xi) e^{in\varphi}, \quad \xi = m_s \rho, \quad (2.2.14)$$

where m_s is the mass of the massive particle in the broken vacuum

$$m_s^2 = \lambda\eta^2 . \quad (2.2.15)$$

The equation of motion (2.2.11) then takes the form

$$f'' + \frac{1}{\xi}f' - \frac{n^2}{\xi^2}f - \frac{1}{2}(f^2 - 1)f = 0 , \quad (2.2.16)$$

which is a non-linear second order ordinary differential equation. The equation can be solved numerically (e.g., using relaxation method), with the boundary conditions $f(0) = 0, f(\infty) = 1$. For practical purposes it is convenient to change coordinates to deal only with finite interval.

A Taylor series expansion shows that for large ξ , $f \sim 1 - n^2/\xi^2$. Because of the slow n^2/ξ^2 decay, the energy per unit length is infinite. This is a direct consequence of the presence of the massless Goldstone boson.

2.2.2 Local strings

Let us now investigate what happens if the Lagrangian is invariant under a local gauge symmetry. In the simplest case the gauge group is the Abelian $U(1)$.

The Lagrangian density is then given by

$$L = -|D_A\Phi|^2 - \frac{1}{4}F_{AB}F^{AB} - V(\Phi) , \quad (2.2.17)$$

where $D_B = \partial_B + ieA_B$ and $F_{CD} = \partial_C A_D - \partial_D A_C$. Under the action of $U(1)$ the fields transform according to

$$\Phi \rightarrow e^{i\Lambda(x)}, \quad A_B \rightarrow A_B - \frac{1}{e}\partial_B\Lambda(x) . \quad (2.2.18)$$

The equations of motion for the fields are

$$[D^2 + \lambda(|\Phi|^2 - \frac{1}{2}\eta^2)]\Phi = 0 , \quad (2.2.19)$$

$$\partial_B F^{AB} + ie (\Phi^* D^A \Phi - D^A \Phi^* \Phi) = 0 . \quad (2.2.20)$$

We, again, switch to cylindrical coordinates, and choose the radial gauge $A_\rho = 0$. The ansatz now has the form

$$\Phi = \frac{\eta}{\sqrt{2}} f(\rho) e^{in\varphi}, \quad A_\varphi = \frac{n}{e} a(\rho) . \quad (2.2.21)$$

After the substitution into the equations of motion (2.2.19)–(2.2.20), we obtain two non-linear second order differential equations

$$f'' + \frac{f'}{\rho} - \frac{m_s^2}{2} (f^2 - 1) - \frac{n^2}{\rho^2} f (a^2 - 1) = 0 , \quad (2.2.22)$$

$$a'' - \frac{a'}{\rho} - m_v^2 f^2 (a - 1) = 0 . \quad (2.2.23)$$

They can be solved only numerically, but it is possible to obtain their asymptotic behavior (see, e.g., [1])

$$f \simeq \begin{cases} f_0 \xi^{|n|}, \\ 1 - f_1 \xi^{-1/2} \exp(-\sqrt{\beta} \xi), \end{cases} \quad a \simeq \begin{cases} a_0 \xi^2 - \frac{|n| f_0^2}{4(|n|+1)} \xi^{2|n|+2}, & \text{as } \xi \rightarrow 0; \\ 1 - a_1 \xi^{1/2} \exp(-\xi), & \text{as } \xi \rightarrow \infty. \end{cases} \quad (2.2.24)$$

Here, $\xi = m_v \rho$ and $\beta = \lambda/e^2 = (m_s/m_v)^2$. If $\beta > 4$, $\xi^{-1/2} \exp(-\sqrt{\beta} \xi)$ is replaced by $\xi^{-1} \exp(-2\xi)$.

Since now the vector boson is massive, the energy is much better localized, with the energy per unit length given by

$$\mu = \int \mathcal{E}(\rho) \rho d\rho d\varphi = \pi \eta^2 \epsilon(\beta) . \quad (2.2.25)$$

The function $\epsilon(\beta)$ must be obtained numerically. For the critical coupling $\beta = 1$ it is possible to show that $\epsilon(1) = 1$.

The magnetic flux through the string is given by

$$\int \vec{B} \cdot d\vec{S} = \oint_{S_\infty} d\vec{l} \cdot \vec{A} = \frac{2\pi n}{e} . \quad (2.2.26)$$

The vortices are stable for any n if $\beta < 1$, and split into n vortices each carrying a unit flux $2\pi/e$ for $\beta > 1$. This can be understood from the fact that there are two competing forces acting on the vortices. The repulsive force is due to the repulsion of magnetic flux lines. The range of this force is controlled by the Compton wavelength $\lambda_v \sim 1/m_v$ of the vector boson. The attractive force is due to the tendency to minimize the area of the vanishing scalar field, and its range is controlled by the Compton wavelength $\lambda_s \sim 1/m_s$. The winner is the one with longer range. Since $\beta = \lambda_v^2/\lambda_s^2$, the results make sense.

2.3 Domain Walls

Domain walls arise from models in which a discrete symmetry is broken. In general, they form when the vacuum manifold M has two or more disconnected pieces. This is classified by the homotopy group $\pi_0(M)$, which counts the disconnected parts of M . The simplest such model is described by Lagrangian density

$$L = -\frac{1}{2}\partial_A\Phi\partial^A\Phi - \frac{1}{2}\lambda(\Phi^2 - \eta^2)^2, \quad (2.3.27)$$

where Φ is a real scalar field. The discrete symmetry is \mathbb{Z}_2 , i.e., $\Phi \rightarrow -\Phi$. The vacuum manifold consists of two points, $\Phi = \pm\eta$.

Suppose that our solution is such that $\Phi \rightarrow -\eta$ as $z \rightarrow -\infty$ and $\Phi \rightarrow \eta$ as $z \rightarrow \infty$. We assume that the solution is antisymmetric in the z coordinate and thus $\Phi = 0$ at $z = 0$. This means that a plain wall of false vacuum is created in the XY -plane. It is easy to check that the exact solution has the form

$$\Phi(Z) = \eta \tanh\left(\frac{Z}{\delta}\right), \quad (2.3.28)$$

where $\delta = \lambda^{-1/2}\eta^{-1}$ is the thickness of the domain wall. The surface density σ can be estimated as $\sigma \sim \delta\rho_V$. The density of the false vacuum $\rho_V \sim \lambda\eta^4$ and

thus $\sigma \sim \lambda^{1/2} \eta^3$. The exact density can be calculated from the stress-energy tensor

$$T_{AB} = \partial_A \Phi \partial_B \Phi - g_{AB} L, \quad (2.3.29)$$

where g_{AB} is the Minkowski metric. The result is

$$T^A{}_B = \lambda \eta^4 \left[\cosh \left(\frac{Z}{\delta} \right) \right]^{-4} \text{diag}(1, 1, 1, 0). \quad (2.3.30)$$

The exact energy per surface area is then given by

$$\sigma = \int_{-\infty}^{\infty} T^0{}_0 dZ = \frac{4}{3} \lambda^{1/2} \eta^3. \quad (2.3.31)$$

2.4 The Nambu-Goto Effective Action

So far we considered only static configurations of topological defects. In order to study their dynamics, we need some sort of effective action which would allow us to derive the equations of motion. Of course, the action for the fields is known, and thus we can, in principle, calculate everything we need. But such treatment is neither practical nor necessary⁴.

It is legitimate in planetary astronomy to treat Earth as a point-like particle. It happens when the other scales entering the problem are much larger than the Earth size. In a similar way it is legitimate to consider n -brane⁵ as an n -dimensional object when the radius of the (extrinsic) curvature of the brane R is much larger than its characteristic thickness δ , and the geometry of spacetime itself varies on much larger length scales than δ . In this approximation the motion of the brane in the $(n+k+1)$ -dimensional spacetime is described by the

⁴Although sometimes this approach is used in order to answer more subtle questions, e.g., what happens when strings intercommute etc.. One then needs to perform numerical lattice field theory simulations.

⁵Here the term n -brane denotes a generic n -dimensional topological defect.

Nambu-Goto effective action

$$S[X^A] = \sigma \int d^{n+1}x \sqrt{-\gamma} , \quad (2.4.32)$$

where σ is the tension of the brane.

Let us show now how one can derive the effective action from the field action

$$S_F = \int d^{n+k+1}X \sqrt{-g} L , \quad (2.4.33)$$

where k is the number of extra dimensions and L is the Lagrangian of the underlying field theory. For our purposes we do not need to know its form exactly. If $R \gg \delta$ the solution for a moving and distorted brane can be obtained by “gluing” together static solutions (analogous to those described for local strings in subsection 2.2.2) and integrating out the transverse degrees of freedom. To do this, we use the construction described in [1].

We parameterize the worldsheet of the brane (defined by the zeros of the Higgs field) by x^μ ($\mu = 0, \dots, n$), with x^0 being timelike and the remaining x^i -s spacelike. At each point of the brane we erect a k -plane perpendicular to the tangent vectors to the worldsheet, $X_{,\mu}^A$. This plane is spanned by k orthonormal spacelike vectors n_a^A ($a = 1, \dots, k$). Thus we have

$$g_{AB} n_a^A X_{,\mu}^B = 0 , \quad (2.4.34)$$

$$g_{AB} n_a^A n_b^B = \delta_{ab} . \quad (2.4.35)$$

By defining k new coordinates ρ^a corresponding to n_a^A we can reparameterize any point near the worldsheet

$$X^A(\xi^B) = (X^A(x^\mu), \rho^a n_a^A(x^\mu)) . \quad (2.4.36)$$

Note that the new coordinates $\xi^A = (x^\mu, \rho^a)$ are single valued only if the point X^A is closer to the brane than its curvature radius R .

The participating fields are defined by the static solution of a straight brane in flat spacetime. We identify the coordinates ρ^a with the extra k dimensions.

In order to write the action (2.4.33) in the new coordinates ξ^A , we need to evaluate the Jacobian

$$\sqrt{-\det g} \det \left(\frac{\partial X}{\partial \xi} \right) = \sqrt{-\det \left\{ g \left(\frac{\partial X}{\partial \xi} \right) \left(\frac{\partial X}{\partial \xi} \right) \right\}} = \sqrt{-\det M} , \quad (2.4.37)$$

where the matrix M has the form

$$M_{\alpha\beta} = g_{AB} \frac{\partial X^A}{\partial \xi^\alpha} \frac{\partial X^B}{\partial \xi^\beta} = \text{diag}(\gamma_{\mu\nu}, \delta_{ab}) + O(\rho/R) . \quad (2.4.38)$$

The higher order ‘‘curvature’’ terms arise from the derivatives of n_a^A with respect to x^μ .

To the lowest order then we have $\det M = \det \gamma$. Since the fields are (to the lowest order) independent of x^μ we can perform the partial $d^k \rho$ integration of the action. This yields the brane energy density factor σ in front of the Nambu-Goto effective action

$$S[X^A] = \sigma \int d^{n+1}x \sqrt{-\gamma} . \quad (2.4.39)$$

It is also possible to work with a slightly different but equivalent form of the action. The idea is to introduce an additional auxiliary field on the worldsheet — a so-called internal metric $h_{\mu\nu}$. The resulting Polyakov action has the form [25]

$$S_P[X^A, h_{\mu\nu}] = -\mu \int d^{n+1}x \sqrt{-h} h^{\mu\nu} \gamma_{\mu\nu} . \quad (2.4.40)$$

2.5 Dynamics of Topological Defects

To obtain the equations of motion for an n -brane in a fixed background spacetime, we use the standard procedure of varying the action (2.4.32) with respect to the fields X^A . The variation yields

$$\frac{\delta S[X^A]}{\delta X^A} = \square X^A + \gamma^{\mu\nu} \Gamma^A_{BC} X^B_{,\mu} x^C_{,\nu} = 0 . \quad (2.5.41)$$

The box operator \square has the form

$$\square = \frac{1}{\sqrt{-\gamma}} \partial_\mu (\sqrt{-\gamma} \gamma^{\mu\nu} \partial_\nu) , \quad (2.5.42)$$

and $\Gamma^A{}_{BC}$ are the standard Christoffel symbols associated with the background metric.

For the string the induced two-dimensional metric $\gamma_{\mu\nu}$ is conformal to the flat metric $\eta_{\mu\nu}$, so it is always (at least locally) possible to write it in the form

$$\gamma_{\mu\nu} = e^{2\omega(\tau,\sigma)} \eta_{\mu\nu} . \quad (2.5.43)$$

Here, $\tau \equiv x^0$ and $\sigma \equiv x^1$. In this gauge $\sqrt{-\gamma} \gamma^{\mu\nu} = \eta^{\mu\nu}$, and the equations of motion reduce to a simpler form. After multiplying (2.5.41) by $\sqrt{-\gamma}$ we obtain

$$\square X^A + \Gamma^A{}_{BC} \left\{ -\frac{\partial X^B}{\partial \tau} \frac{\partial X^C}{\partial \tau} + \frac{\partial X^B}{\partial \sigma} \frac{\partial X^C}{\partial \sigma} \right\} . \quad (2.5.44)$$

In the above the box operator is the flat two-dimensional wave operator $\square = -\partial_\tau^2 + \partial_\sigma^2$. The constraint equations (2.5.43) have the form

$$\gamma_{01} = g_{AB} \frac{\partial X^A}{\partial \tau} \frac{\partial X^B}{\partial \sigma} = 0 , \quad (2.5.45)$$

$$\gamma_{00} + \gamma_{11} = g_{AB} \left(\frac{\partial X^A}{\partial \tau} \frac{\partial X^B}{\partial \tau} + \frac{\partial X^A}{\partial \sigma} \frac{\partial X^B}{\partial \sigma} \right) = 0 . \quad (2.5.46)$$

The system of equations (2.5.44) is semi-linear. For $n > 1$ such simple choice of gauge is impossible so that in general case the equations of motion for branes are non-linear. We discuss the gauge fixing for branes in the weak field approximation in section 6.4.

2.6 Cosmic Strings in Cosmology

Although topological defects have never been observed so far, they may have played important role in cosmology, especially in the process of structure formation. Studies show that domain walls and monopoles are in contradiction with cosmological models not considering inflation.

If domain walls existed in our universe they would soon dominate the energy density of the universe. For example a wall of size H_0^{-1} (H_0 is the Hubble constant) would have a mass $M_{\text{wall}} \sim \sigma H_0^{-2} \sim 10^{65} \lambda^{1/2} (\eta/100\text{GeV})^3$ grams which is about $10^{10} \lambda^{1/2} (\eta/100\text{GeV})^3$ times more than is observed in the present Hubble volume. Furthermore, domain walls would cause large temperature fluctuations in CMB $\delta T/T \simeq G\sigma H_0^{-1} \simeq 10^{10} \lambda^{1/2} (\eta/100\text{GeV})^3$.

It is not difficult to estimate the mass density and flux of monopoles created at the GUT scale (see, e.g., [26]). The lower bound can be set by assuming the presence of one monopole per Hubble volume at the time of creation. The estimated values are much higher than the observational upper bounds (see e.g. [27]). This inconsistency is in fact rather serious since there exists a proof by t'Hooft and Polyakov that monopoles will exist in most spontaneously broken non-Abelian theories.

The monopole problem can be avoided by introducing the concept of *inflation* [28, 29]. Inflation is considered to be the initial phase of the evolution of our universe during which the scale factor changes by many orders of magnitude while the energy density and pressure change slowly.

Inflation also helps to solve a variety of other problems present in the standard cosmological model. For example, the inflated quantum fluctuations of the scalar field could constitute the initial inhomogeneities needed for galaxy formation.

A competing theory of structure formation assigns the leading role for inhomogeneity creation to cosmic strings. Cosmic strings are the only topological defects compatible with observations. A naive estimate shows that the energy density of a static string network scales as $\rho_S \sim a(t)^{-2}$, where $a(t)$ is the scale factor present in the Friedman-Fermi-Walker (FRW) model of expanding universe⁶. This scaling would be disastrous since cosmic strings would dominate the

⁶Since the string tension equals to the string energy per unit length, the energy density of a string in expanding universe stays constant. Therefore the energy of a static string network

energy density of the universe similarly to the domain walls case.

Fortunately, it was shown that it does not occur and there is a mechanism which changes the scaling behavior so that the result is compatible with observations. In particular, it has been shown that when two strings cross, they “change partners”, i.e., intercommute. This mechanism leads to loop formation. Loops are closed string segments which typically oscillate and later decay by emitting gravitational radiation. Loop decay is responsible for a $a(t)^{-4}$ string scaling, i.e., the string density maintains a constant ratio to the matter density in a radiation dominated universe. It is generally believed that the evolution of string networks converges to a so-called *scaling solution*. This means that the network properties, when normalized to the Hubble radius, remain (statistically) unchanged.

Numerical simulations also show that during dynamical evolution strings develop fine structure (wiggles) superimposed on the straight string. This effectively changes the string’s stress-energy tensor and consequently the spacetime around the string. Wiggly strings therefore affect differently the surrounding matter and thus models taking into account the wiggleness predict a slightly different matter density fluctuations than models using “ordinary” strings [5].

Matter density fluctuations in the early universe are responsible for the temperature fluctuations in CMB. Much work has been done to calculate the effect of cosmic strings on the CMB. The calculations are complicated and approximations must be made in order to render the calculations tractable. Moreover, the string model is not unique and various parameters are introduced to allow for different models. Since measurements of CMB fluctuations are one of the most promising experimental tools for understanding the initial conditions for structure formation, we briefly review the fundamentals of the CMB radiation.

As we go backward in time the universe becomes hotter and denser. When enclosed in a comoving volume V increases linearly whereas the physical volume $\sim a(t)^3$. Therefore $\rho_S \sim a(t)^{-2}$. Analogous arguments for domain walls give $\rho_W \sim a(t)^{-1}$.

the universe was about thousand times smaller than today, its temperature was high enough to ionize atoms (mostly hydrogen and some helium). The universe then consisted of an ionized plasma of protons, electrons and photons. Due to Thomson scattering of photons by electrons the mean free photon path was short, and the photons were in thermal equilibrium with the surrounding matter. As the universe expands photons become less energetic and at about $T \simeq 4000K$ they can no longer ionize the hydrogen atoms. At that point (also called *recombination*) photons decoupled from matter and continued their journey virtually undisturbed by matter. The recombination epoch completed very rapidly. The CMB we observe today originated at the surface of last scattering — a sphere with radius $\sim 10^{10}$ light years. Because the universe is expanding the temperature of the CMB radiation dropped to the today's value of $2.728K \pm 0.004$.

The fluctuations of the CMB mirror the conditions of the universe at the recombination epoch when the universe was about 300,000 years old. Due to initial inhomogeneities the baryon-photon fluid underwent oscillations. Gravity served as the driving force and photons provided the restoring force. It can be shown ([30–32]) that each Fourier mode k obeys the harmonic-oscillator-like equation

$$[m_{\text{eff}} \Delta T_k']' + \frac{k^2}{3} \Delta T_k = -F_k , \quad (2.6.47)$$

where m_{eff} is the effective mass of the fluid, F_k is the driving force due to fluctuations in gravitational potential and primes denote derivatives with respect to the conformal time $\eta = \int dt/a(t)$. The main contribution to the temperature fluctuation in CMB is due to the difference in gravitational redshift of photons climbing from different gravitational potentials ⁷(Sachs-Wolfe effect).

What is in practice measured is the correlation function of the temperature

⁷There are many other (secondary) effects which affect the photons during the recombination and on their long way to our detectors.

fluctuations between points in the sky separated by a certain angular distance θ . Since the surface of last scattering is a sphere it is natural to expand the correlation function into spherical harmonics

$$\left\langle \frac{\Delta T}{T}(\mathbf{n}) \frac{\Delta T}{T}(\mathbf{n}') \right\rangle_{\mathbf{n} \cdot \mathbf{n}' = \cos \theta} = \sum_{l, l', m, m'} \langle a_{lm} a_{l'm'}^* \rangle Y_{lm}(\mathbf{n}) Y_{l'm'}^*(\mathbf{n}') . \quad (2.6.48)$$

Since we assume that the initial disturbances are statistically isotropic

$$\langle a_{lm} a_{l'm'}^* \rangle = \delta_{ll'} \delta_{mm'} c_l . \quad (2.6.49)$$

After substituting (2.6.49) into (2.6.48) and using the identity

$$\sum_{m=-l}^l Y_{lm}(\mathbf{n}) Y_{lm}^*(\mathbf{n}') = \frac{2l+1}{4\pi} P_l(\mathbf{n} \cdot \mathbf{n}') \quad (2.6.50)$$

we get

$$\left\langle \frac{\Delta T}{T}(\mathbf{n}) \frac{\Delta T}{T}(\mathbf{n}') \right\rangle_{\mathbf{n} \cdot \mathbf{n}' = \cos \theta} = \frac{1}{4\pi} \sum_l (2l+1) c_l P_l(\cos \theta) , \quad (2.6.51)$$

where P_l -s are the Legendre polynomials.

Figure 2.1 shows data combined from different experiments together with three theoretical curves. The picture and description is taken from [9]. The upper dot-dashed line represents the prediction of a Λ CDM model, with cosmological parameters set as $n_s = 1$, $\Omega_\Lambda = 0.7$, $\Omega_m = 0.3$, $\Omega_b = 0.05$ and $h = 0.6$ in agreement with all other data but CMB's. The lower dashed line is a typical string spectrum. Both of these are seen not to fit the new BOOMERanG [33], MAXIMA [34] and DASI [35] data (circles, triangles and diamonds respectively) and are normalized at the COBE scale (crosses). Combining both curves with the extra-parameter α produces the solid curve, with a χ^2 per degree of freedom slightly above unity. The string contribution turns out to be some 18% of the total. With the former BOOMERanG data which produced a much lower second peak, the string content was raised to 38% of the total.

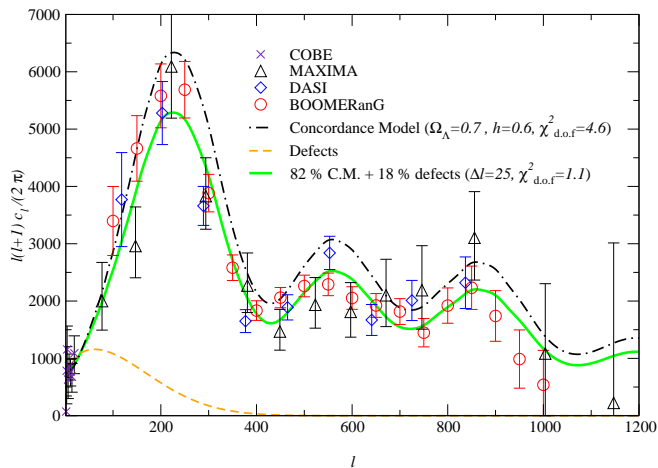


Figure 2.1: $l(l+1)c_l/2\pi$ versus l for three different models.

We see that the spectrum consists of a strong acoustic peak centered around $l = 250$ and few secondary peaks slowly decaying as we approach smaller angular scales (large l -s). At those scales the finite time of recombination smears out the effect caused by density fluctuations.

As illustrated by figure 2.1, it is clear that pure topological defects without inflation are incompatible with the observational data. However, it is also clear that superposition of cosmic strings and inflation does not contradict the observations either. The superposition is calculated simply as

$$c_l = \alpha c_l^I + (1 - \alpha) c_l^S, \quad (2.6.52)$$

where the superscripts indicate either inflation or strings.

Future, more precise measurements can clarify the situation, since strings and inflation leave different signatures in the CMB. In particular, theory predicts a non-Gaussian component in the power spectrum induced by strings. At present there is no consensus whether the actual data contain this component.

Besides the temperature anisotropy, we also expect anisotropy in the photon polarizations. Measurements of these anisotropies can help us to identify important parameters in cosmological models since it happens that the temperature

anisotropy is sensitive to a combination of parameters and thus it is impossible to deduce the value of each individual parameter even from a very precise measurements. Since polarization anisotropy is sensitive to different combinations of the parameters it can split this parameter “degeneracy”.

To conclude this section about the recent state of cosmic strings we cite the summary of [9]: “In conclusion, we have found that a mixture of inflation and topological defects can perfectly well accommodate the current CMB data, with standard values of the cosmological parameters”.

Chapter 3

Cosmic Strings in Kerr Geometry

In this chapter we present a solution for the string motion in the weak field approximation and discuss the setup for scattering and capture of infinitely long straight cosmic string in the Kerr spacetime. We introduce the basic terminology and explain how we execute the numerical experiments.

3.1 Kerr Geometry

Our aim is to study string motion in the Kerr spacetime. The Kerr metric in Boyer-Lindquist coordinates (t, r, θ, ϕ) has the form

$$ds^2 = -\left(1 - \frac{2Mr}{\Sigma}\right)dt^2 + \frac{\Sigma}{\Delta}dr^2 + \Sigma d\theta^2 + \frac{A \sin^2 \theta}{\Sigma}d\phi^2 - \frac{4aMr \sin^2 \theta}{\Sigma}dt d\phi, \quad (3.1.1)$$

$$\Sigma = r^2 + a^2 \cos^2 \theta, \quad (3.1.2)$$

$$\Delta = r^2 - 2Mr + a^2, \quad (3.1.3)$$

$$A = (r^2 + a^2)^2 - a^2 \Delta \sin^2 \theta, \quad (3.1.4)$$

where M is the mass of the black hole, and $J = aM$ is its angular momentum ($0 \leq a \leq M$).

In order to be able to deal with the case where part of the string crosses the event horizon for the numerical simulation we also adopt the so-called Kerr (in-going) coordinates $(\tilde{v}, r, \theta, \tilde{\phi})$

$$ds^2 = -\left(1 - \frac{2Mr}{\Sigma}\right)d\tilde{v}^2 + 2d\tilde{v}dr - \frac{4aMr \sin^2 \theta}{\Sigma}d\tilde{v}d\tilde{\phi} - a \sin^2 \theta dr d\tilde{\phi} + \Sigma d\theta^2 + \frac{A \sin^2 \theta}{\Sigma}d\tilde{\phi}^2, \quad (3.1.5)$$

with

$$\tilde{v} = t + r + M \ln \left| \frac{\Delta}{4M^2} \right| + \frac{M^2}{\sqrt{M^2 - a^2}} \ln \left| \frac{r - M - \sqrt{M^2 - a^2}}{r - M + \sqrt{M^2 - a^2}} \right| + M, \quad (3.1.6)$$

$$\tilde{\phi} = \phi + \frac{a}{2\sqrt{M^2 - a^2}} \ln \left| \frac{r - M - \sqrt{M^2 - a^2}}{r - M + \sqrt{M^2 - a^2}} \right|. \quad (3.1.7)$$

The metric (3.1.1) has the asymptotic form

$$ds^2 = -dt^2 + dr^2 + r^2(d\theta^2 + \sin^2 \theta d\phi^2) + \frac{2M}{r}(dt^2 + dr^2) - \frac{4aM}{r} \sin^2 \theta dt d\phi. \quad (3.1.8)$$

Let us introduce new “quasi-Cartesian” coordinates

$$T = t, \quad (3.1.9)$$

$$X = R \sin \theta \cos \phi, \quad (3.1.10)$$

$$Y = R \sin \theta \sin \phi, \quad (3.1.11)$$

$$Z = R \cos \theta, \quad (3.1.12)$$

where

$$r = R + M. \quad (3.1.13)$$

One can easily check that the metric (3.1.8) in the quasi-Cartesian coordinates (3.1.9)–(3.1.12) has the asymptotic form

$$ds^2 = -\left(1 - \frac{2M}{R}\right)dT^2 + \left(1 + \frac{2M}{R}\right)(dX^2 + dY^2 + dZ^2) - \frac{4J}{R^3}(XdY - YdX)dT, \quad (3.1.14)$$

where $R^2 = X^2 + Y^2 + Z^2$, and M and $J = aM$ are the mass and angular momentum of the black hole, respectively.

It should be emphasized that without the shift (3.1.13) of the radial coordinate one does not recover (3.1.14). The reason for this is easy to understand if one considers the same problem for the Schwarzschild geometry. The asymptotic limit of (3.1.14) with $J = 0$ can be found in the isotropic coordinates with $r = \tilde{R}(1 + M/2\tilde{R})^2$ in which the spatial part of the metric is conformal to the flat metric. Asymptotically, it is sufficient to use (3.1.13) which is the leading part of r at large \tilde{R} .

In what follows we shall use these quasi-Cartesian coordinates for representing the position and the form of the string in the Kerr spacetime even if we are not working in the weak field regime. It should be emphasized that since the space in the Kerr geometry is not flat, plots constructed in these coordinates do not give a “real picture”. This is a special case of a general problem of the visualization of physics in a four-dimensional curved spacetime.

3.2 Cosmic String Scattering

3.2.1 Weak field approximation to the scattering of a string moving in a Kerr spacetime

In the absence of the external gravitational field $g_{AB} = \eta_{AB}$, where η_{AB} is the flat spacetime metric. In Cartesian coordinates (T, X, Y, Z) , $\eta_{AB} = \text{diag}(-1, 1, 1, 1)$ and $\Gamma^A_{BC} = 0$, and it is easy to verify that

$$\mathcal{X}^A = \mathcal{X}_0^A(\tau, \sigma) \equiv (\tau \cosh \beta, \tau \sinh \beta + X_0, b, \sigma), \quad (3.2.15)$$

$$\gamma_{\mu\nu} = \eta_{\mu\nu} \equiv \text{diag}(-1, 1), \quad (3.2.16)$$

satisfy equations (2.5.44)–(2.5.46). This solution describes a straight string oriented along the Z -axis which moves in the X -direction with constant velocity $v = \tanh \beta$. Initially, at $\tau_0 = 0$, the string is found at $\mathcal{X}^A(0, \sigma) = (0, X_0, b, \sigma)$. Later when we use this solution as initial data for a string scattering by a black hole, b will play the role of impact parameter. For definiteness we choose $b > 0$ and $X_0 < 0$, so that $\beta > 0$.

Let us consider how this solution is modified when the straight string is moving in a weak gravitational field. We assume

$$g_{AB} = \eta_{AB} + q_{AB}, \quad (3.2.17)$$

$$\mathcal{X}^A(x^\mu) = \mathcal{X}_0^A(x^\mu) + \chi^A(x^\mu), \quad (3.2.18)$$

where q_{AB} is the metric perturbation and χ^A is the string perturbation. By making the perturbation of the equation of motion one gets

$$\square \chi^A = f^A, \quad (3.2.19)$$

where

$$f^A = f^A(x^\mu) = -\Gamma^A_{BC}(\mathcal{X}_0) \mathcal{X}_{0,\mu}^B \mathcal{X}_{0,\nu}^C \eta^{\mu\nu}. \quad (3.2.20)$$

We use Cartesian coordinates for the background metric so that Γ^A_{BC} is simply the Christoffel symbol for q_{AB} .

The linearized constraint equations (2.5.45)–(2.5.46) are

$$\eta_{AB} \frac{\partial \mathcal{X}_0^A}{\partial \tau} \frac{\partial \chi^B}{\partial \sigma} + \eta_{AB} \frac{\partial \chi^A}{\partial \tau} \frac{\partial \mathcal{X}_0^B}{\partial \sigma} + q_{AB} \frac{\partial \mathcal{X}_0^A}{\partial \tau} \frac{\partial \mathcal{X}_0^B}{\partial \sigma} = 0, \quad (3.2.21)$$

$$2\eta_{AB} \left(\frac{\partial \mathcal{X}_0^A}{\partial \tau} \frac{\partial \chi^B}{\partial \tau} + \frac{\partial \mathcal{X}_0^A}{\partial \sigma} \frac{\partial \chi^B}{\partial \sigma} \right) + q_{AB} \left(\frac{\partial \mathcal{X}_0^A}{\partial \tau} \frac{\partial \mathcal{X}_0^B}{\partial \tau} + \frac{\partial \mathcal{X}_0^A}{\partial \sigma} \frac{\partial \mathcal{X}_0^B}{\partial \sigma} \right) = 0. \quad (3.2.22)$$

As in the exact non-linear case, if these linearized constraints are satisfied at the initial moment of time τ they are also valid for any τ for a solution χ^A of the dynamical equations (3.2.19).

The linearized equations can be used to study string motion in the case where it is far away from the black hole. In this case the gravitational field can be approximated by the metric (3.1.14). In fact the asymptotic form of the metric is valid for any arbitrary stationary localized distribution of matter, provided that the observer is located far from it. In agreement with (3.1.14) the gravitational field perturbation can be presented as

$$q_{AB} = q_{AB}^N + q_{AB}^{LT}, \quad (3.2.23)$$

where the Newtonian and Lense-Thirring parts are

$$q_{AB}^N = 2\varphi\delta_{AB}, \quad \varphi = \frac{M}{R}, \quad q_{AB}^{LT} = \frac{4J}{R^3} \delta_{(A}^0 \epsilon_{B)C03} X^C. \quad (3.2.24)$$

Here ϵ_{ABCD} is the antisymmetric symbol. The Lense-Thirring part q_{AB}^{LT} of the metric [24, 36] is produced by the rotation of the source of the gravitational field and it is responsible for frame dragging.

Newtonian scattering

In the linear approximation we can study the action of each of the parts of the metric perturbations independently. For the Newtonian part one has the following expression for the force f_N^A

$$f_N^0 = 2 \sinh \beta \cosh \beta \varphi_{,1}, \quad (3.2.25)$$

$$f_N^1 = 0, \quad (3.2.26)$$

$$f_N^2 = -2 \sinh^2 \beta \varphi_{,2}, \quad (3.2.27)$$

$$f_N^3 = -2 \cosh^2 \beta \varphi_{,3}, \quad (3.2.28)$$

and the constraint equations read

$$\chi_{,\tau}^3 - \cosh \beta \chi_{,\sigma}^0 + \sinh \beta \chi_{,\sigma}^1 = 0, \quad (3.2.29)$$

$$\chi_{,\sigma}^3 - \cosh \beta \chi_{,\tau}^0 + \sinh \beta \chi_{,\tau}^1 = -2\varphi \cosh^2 \beta . \quad (3.2.30)$$

The result $f^1 = 0$ means that in the first order approximation the string lies in the YZ -plane at any fixed time $\tau = \text{const.}$ The dynamical equations (3.2.19) can be easily integrated by using the retarded Green's function (see, e.g., [19]).

The solutions read

$$\begin{aligned} \chi^0/M &= \ln(F_+ F_-) + \frac{1}{2} \cosh \beta [\text{sgn}(s_+) \ln(G_+) + \text{sgn}(s_-) \ln(G_-)] \\ &+ \cosh \beta \ln \left(\frac{(s_+ + \sqrt{s_+^2 + \rho^2})(s_- + \sqrt{s_-^2 + \rho^2})}{\rho^2} \right) , \end{aligned} \quad (3.2.31)$$

$$\chi^1/M = 0 , \quad (3.2.32)$$

$$\chi^2/M = -\sinh \beta (H_+ + H_-) , \quad (3.2.33)$$

$$\chi^3/M = \cosh \beta \ln \left(\frac{F_+}{F_-} \right) , \quad (3.2.34)$$

where

$$\begin{aligned} H_{\pm} &= \arctan \left[\frac{b^2 + (X_0 + \tau \sinh \beta)(X_0 + s_{\pm} \sinh \beta)}{bR \sinh \beta} \right] \\ &- \arctan \left[\frac{X_0(X_0 + s_{\pm} \sinh \beta) + b^2}{b \sinh \beta \sqrt{\rho^2 + s_{\pm}^2}} \right] , \end{aligned} \quad (3.2.35)$$

$$F_{\pm} = \frac{R \cosh \beta + \tau \cosh^2 \beta + X_0 \sinh \beta - s_{\pm}}{\cosh \beta \sqrt{\rho^2 + s_{\pm}^2} + X_0 \sinh \beta - s_{\pm}} , \quad (3.2.36)$$

$$G_{\pm} = \frac{\sqrt{\rho^2 + s_{\pm}^2} - |s_{\pm}|}{\sqrt{\rho^2 + s_{\pm}^2} + |s_{\pm}|} , \quad (3.2.37)$$

$$R^2 = (X_0 + \tau \sinh \beta)^2 + b^2 + \sigma^2 , \quad \rho^2 = X_0^2 + b^2 , \quad s_{\pm} = \tau \pm \sigma . \quad (3.2.38)$$

We focus now our attention on the behavior of χ^2 which describes the string deflection in the plane orthogonal to its motion. It is easy to show that the asymptotic value of $\chi^2(\tau \rightarrow \infty, \sigma)$ is the same for any fixed σ . We denote it $-\kappa$. The following expression is valid for κ

$$\kappa = -\frac{1}{2 \sinh \beta} \int_{\Pi_0} dX dZ f^2, \quad (3.2.39)$$

where Π_0 is the two-dimensional worldsheet swept by the undisturbed string in its motion in the background spacetime. This integral can be easily calculated since

$$\int_{\Pi_0} dX dZ \varphi_{,Y} = 2\pi M \quad (3.2.40)$$

is the flux of the Newtonian field strength through the plane Π_0 . Thus we have

$$\kappa = 2\pi M \sinh \beta. \quad (3.2.41)$$

At any late moment of time τ the central part of the string is a straight line moving in the plane $Y = b - \kappa$, while its far distant parts move in the original plane $Y = b$. These different “phases” are connected by kinks propagating in the direction from the center with the velocity of light. (For details, see [21]). We call κ the *displacement parameter*. Figure 3.1 shows the Y-direction displacement for the Newtonian scattering as a function of τ and σ .

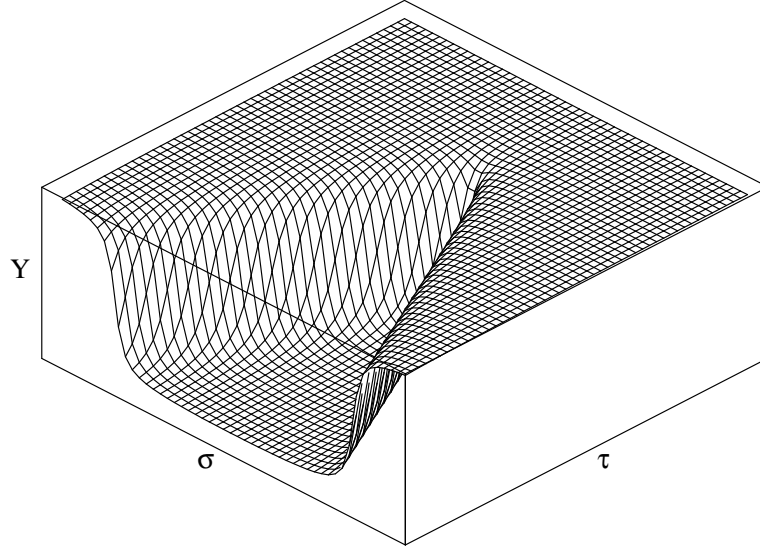
Lense-Thirring scattering

In the presence of rotation the Lense-Thirring force acting on the string in the linearized approximation is

$$f_{LT}^0 = 6J \sinh^2 \beta \frac{b(X_0 + \tau \sinh \beta)}{\mathcal{R}^5}, \quad (3.2.42)$$

$$f_{LT}^1 = 0, \quad (3.2.43)$$

$$f_{LT}^2 = 2J \sinh \beta \cosh \beta \left(\frac{1}{\mathcal{R}^3} - \frac{3\sigma^2}{\mathcal{R}^5} \right), \quad (3.2.44)$$

Figure 3.1: Y -profile for Newtonian scattering

$$f_{LT}^3 = 6J \sinh \beta \cosh \beta \frac{b\sigma}{\mathcal{R}^5}, \quad (3.2.45)$$

where $\mathcal{R} = \sqrt{(X_0 + \tau \sinh \beta)^2 + b^2 + \sigma^2}$. Note that as before, $f^1 = 0$.

The constraint equations now take the form

$$\chi_{,\tau}^3 - \cosh \beta \chi_{,\sigma}^0 + \sinh \beta \chi_{,\sigma}^1 = 0, \quad (3.2.46)$$

$$\chi_{,\sigma}^3 - \cosh \beta \chi_{,\tau}^0 + \sinh \beta \chi_{,\tau}^1 = -2J \sinh \beta \cosh \beta \frac{b}{\mathcal{R}^3}. \quad (3.2.47)$$

The dynamical equations can be solved analytically. For the initial conditions

$$\chi^0|_{\tau=0} = 0, \quad (3.2.48)$$

$$\chi^2|_{\tau=0} = \frac{\partial \chi^2}{\partial \tau}|_{\tau=0} = 0, \quad (3.2.49)$$

$$\chi^3|_{\tau=0} = \frac{\partial \chi^3}{\partial \tau}|_{\tau=0} = 0, \quad (3.2.50)$$

the solution is

$$\chi^0 = Jb \sinh \beta \left(\frac{(X_0 + \tau \sinh \beta) \sinh \beta + \sigma}{\Delta_{(+ -)} \mathcal{R}} + \frac{(X_0 + \tau \sinh \beta) \sinh \beta - \sigma}{\Delta_{(++)} \mathcal{R}} \right)$$

$$- \frac{X_0 \sinh \beta - (\tau - \sigma)}{\Delta_{(+-)\rho_-}} - \frac{X_0 \sinh \beta - (\tau + \sigma)}{\Delta_{(++)\rho_+}} \Big), \quad (3.2.51)$$

$$\chi^1 = 0, \quad (3.2.52)$$

$$\begin{aligned} \chi^2 = -J \sinh \beta \cosh \beta \Big(& \frac{(X_0 + \tau \sinh \beta)^2 + \sigma \sinh \beta (X_0 + \tau \sinh \beta) + b^2}{\Delta_{(++)\mathcal{R}}} \\ & + \frac{(X_0 + \tau \sinh \beta)^2 - \sigma \sinh \beta (X_0 + \tau \sinh \beta) + b^2}{\Delta_{(--)\mathcal{R}}} \\ & + \frac{X_0 \sinh \beta (\tau + \sigma) + X_0^2 + b^2}{\Delta_{(++)\rho_+}} \\ & + \frac{X_0 \sinh \beta (\tau - \sigma) + X_0^2 + b^2}{\Delta_{(--)\rho_-}} \Big), \quad (3.2.53) \end{aligned}$$

$$\begin{aligned} \chi^3 = Jb \sinh \beta \cosh \beta \Big(& \frac{(X_0 + \tau \sinh \beta) \sinh \beta - \sigma}{\Delta_{(++)\mathcal{R}}} - \frac{(X_0 + \tau \sinh \beta) \sinh \beta + \sigma}{\Delta_{(--)\mathcal{R}}} \\ & - \frac{X_0 \sinh \beta - (\tau + \sigma)}{\Delta_{(++)\rho_+}} + \frac{X_0 \sinh \beta - (\tau - \sigma)}{\Delta_{(--)\rho_-}} \Big), \quad (3.2.54) \end{aligned}$$

$$\Delta_{\pm\pm} = (X_0 \pm (\tau \pm \sigma) \sinh \beta)^2 + b^2 \cosh^2 \beta, \quad (3.2.55)$$

$$\rho_{\pm} = \sqrt{X_0^2 + b^2 + (\tau \pm \sigma)^2}. \quad (3.2.56)$$

From these relations it is possible to see that the displacement parameter $\kappa = \lim_{\tau \rightarrow \infty} \chi^2(\tau, \sigma = 0)$ vanishes for this solution. The reason is the following.

Using (3.2.44) it is easy to present f_{LT}^2 as

$$f_{LT}^2 = 2J \sinh \beta \cosh \beta \frac{\partial}{\partial \sigma} \left(\frac{\sigma}{\mathcal{R}^3} \right). \quad (3.2.57)$$

The asymptotic displacement is given by (3.2.39). The integral over Z or, equivalently, the integral over σ of (3.2.57), which is a total derivative over σ , reduces to boundary terms σ/\mathcal{R}^3 at $\sigma = \pm\infty$, which vanish.

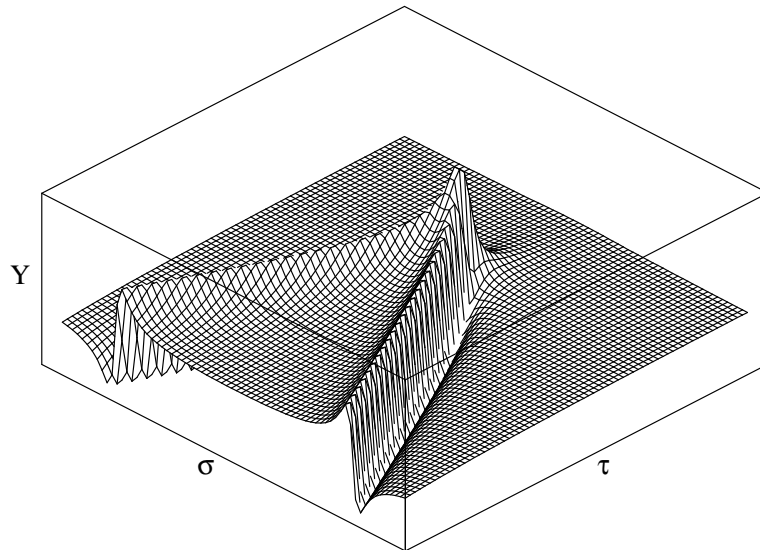
Figure 3.2: Y -profile for Lense-Thirring scattering

Figure 3.2 shows the Y -direction displacement as a function of τ and σ for the weak field scattering. It should be emphasized that the scale of structures for Lense-Thirring scattering is much smaller than that for Newtonian scattering. This can be easily seen if we compare the Newtonian force $f_N \sim M/\mathcal{R}^2$ with the Lense-Thirring force $f_{LT} \sim J/\mathcal{R}^3$

$$\frac{f_{LT}}{f_N} \sim \frac{J}{M\mathcal{R}} \leq \frac{J}{Mb}. \quad (3.2.58)$$

For the scattering by a rotating black hole $J = aM$, where $|a|/M \leq 1$ is the rotation parameter. Hence

$$\frac{f_{LT}}{f_N} \leq \frac{M}{b} \quad (3.2.59)$$

which is small for the weak field scattering. For this reason, in the weak field regime the string profiles for the prograde or retrograde scattering by rotating black hole do not greatly differ from the profiles for the scattering by a non-rotating black hole of the same mass. As we shall see in the next section the situation is different for strong-field scattering: the displacement parameter is

significantly different for prograde and retrograde scattering, and for critical scattering the profiles of the kinks contain visible structure produced by effects connected with the rotation of the black hole.

3.2.2 Scattering of particles by a Kerr black hole

Cosmic string scattering is similar in spirit to a test particle scattering. To study scattering of test particles, we send particles with various velocities and impact parameters towards a black hole, and then look at the outcome. In particular, we are interested whether the particle escapes to infinity or whether it is captured by the black hole. The impact parameter below which the particle is captured, and above which it escapes to infinity, is called the *critical impact parameter*. It is a function of the initial velocity, and in case of rotating black hole, of the angular momentum J as well.

If the test particle moves in the equatorial plane, it is possible to obtain explicit expressions for the critical impact parameter for non-relativistic and ultrarelativistic velocities [37].

For non-relativistic velocities

$$b_c/M = \frac{2}{v} \left(1 + \sqrt{1 - a/M} \right) , \quad (3.2.60)$$

and for ultrarelativistic velocities

$$b_c/M = \left(8 \cos^3 \left[\frac{1}{3} (\pi - \arccos(a/M)) \right] + a/M \right) . \quad (3.2.61)$$

The sign of the rotation parameter a is positive for *prograde* scattering (i.e., both the particle and the black hole have the same sign of their angular momentum) and negative for *retrograde* scattering (i.e., the particle and black hole have opposite angular momenta).

The graph of the critical impact parameter $b_c(v)$ vs. the initial velocity v far from the black hole (theoretically in infinity) is called the critical impact

parameter curve. For a rotating black hole the critical impact parameter is a function of its angular momentum $J = aM$.

For test particles the capture curve decreases monotonically with increasing v , but for strings it has more complicated structure, as it will be shown in chapter 5.

3.2.3 Initial and boundary conditions

In an ideal situation, we would study scattering by initially placing our infinitely straight long string at spatial infinity, where the spacetime is flat and the string can be described in simple terms. In a numerical scheme, however, the string cannot be infinitely long and we must start the simulation at a finite distance from the black hole. We discuss here the initial and boundary conditions used for the simulations.

In studying the scattering of a straight string, we consider the special case where the string is initially parallel to the axis of rotation of the black hole. We use Cartesian coordinates in the asymptotic region so that X -axis coincides with the direction of motion and the Z -axis is parallel to the string (see Fig. 3.3).

We consider a string segment of length L at a time τ_0 and an initial distance X_0 from the black hole. In order to keep accuracy high and yet prevent the calculation time from being inordinately large, we do not evolve the straight string numerically from this initial position. Instead, we use the weak field approximation to describe the string configuration at a later time τ_s where the distance X_s is closer to the black hole, $|X_s| \ll |X_0|$ ¹.

Given a sufficiently long string segment, the boundary points move at a great distance from the black hole, so that their evolution can be described by the weak

¹In our simulations we put $X_0 = -10^6 M$ and $X_s = -500 M$. The length L of the string segment depends on the velocity of the string, simulation time as well as the type of boundary conditions

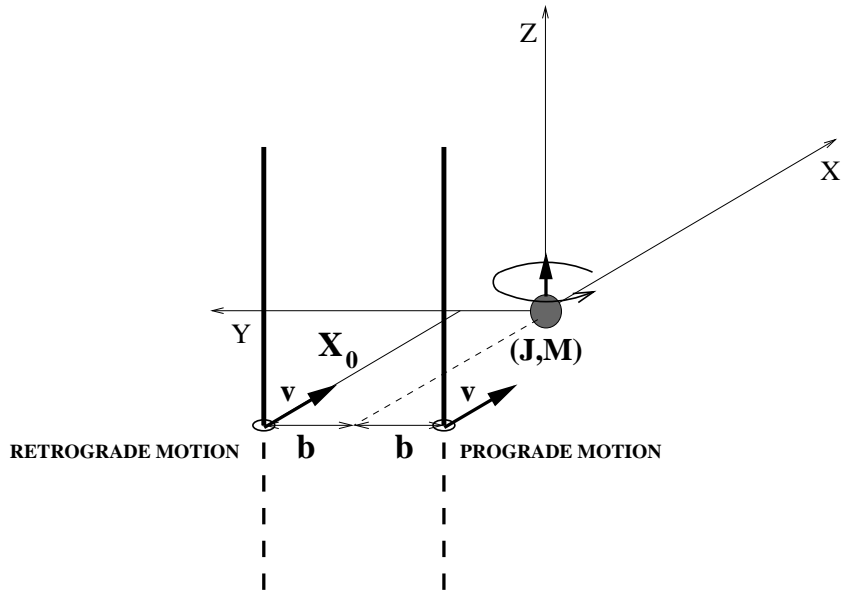


Figure 3.3: Initial setup for prograde and retrograde string motion. The part of the string depicted by the dashed line lies below the XY -plane.

field approximation until information about the interaction with the black hole reaches the boundary. We denote this time as τ_* . Starting from this moment we solve the dynamical equations in the region $|\sigma| < L - (\tau - \tau_*)$ (see figure 3.4). The larger is the initial string length L the longer one can go in τ in the simulation. We choose L to be large enough to provide the required accuracy in the determining the final scattering data.

Since the boundary conditions found from the weak field regime calculations are not exact there will be a disturbance created by this effect. In some cases, when it is important to exclude these disturbances, we used a modified scheme of calculations in which no boundary conditions are used from the very beginning of the simulation. The price for this is that one needs to take a longer initial size of L which in turn increases the computational time.

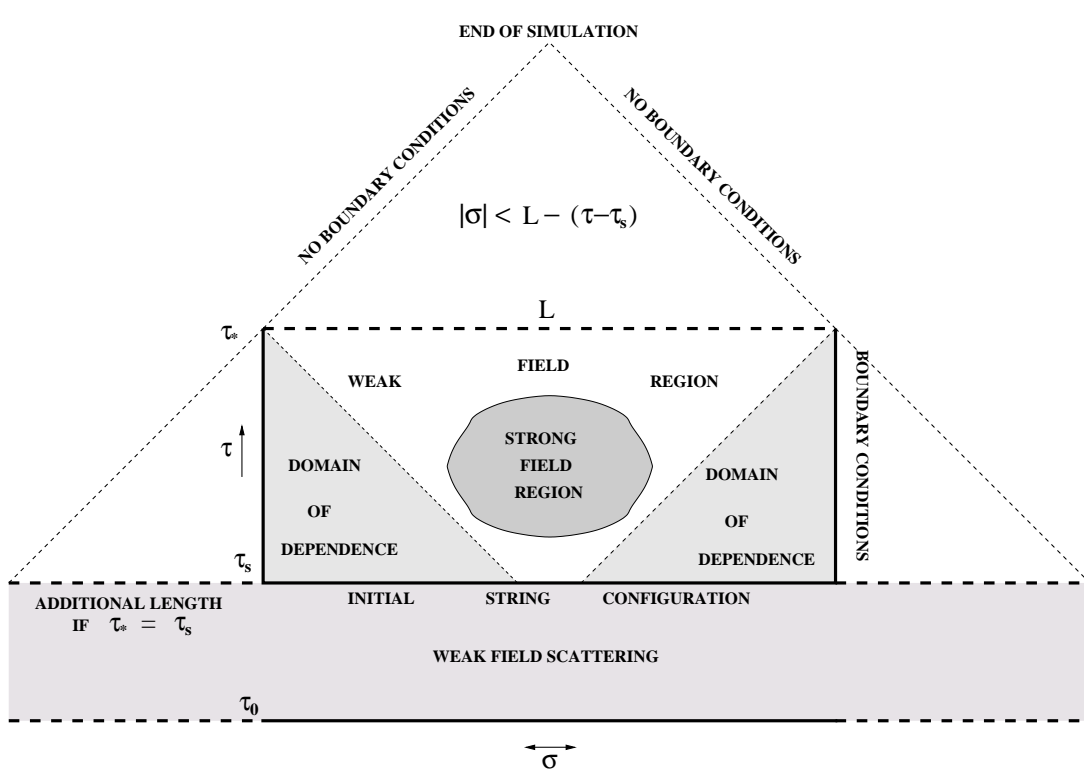


Figure 3.4: Scheme of time domains for scattering problem

3.2.4 Solving dynamical equations and constraints

Using the initial conditions at τ_s and boundary conditions we solve numerically the dynamical equations (2.5.44). Since the equations are of second order, we use the weak field approximation to get initial data at τ_s and $\tau_s + \Delta\tau$ in order to completely specify the initial value problem. The time step $\Delta\tau$ must be chosen to be smaller or equal to the smallest spatial grid distance $\delta\sigma$ (this is the so-called Courant-Friedrichs-Lewy condition). In practice we choose it to be

$$\Delta\tau = \frac{\Delta\sigma}{\cosh\beta} = \Delta\sigma\sqrt{1-v^2}, \quad (3.2.62)$$

where β is the rapidity parameter, i.e., $v = \tanh\beta$. The numerical scheme uses second-order finite differences and evolves the string configuration using an implicit scheme. Because of the symmetry $\sigma \rightarrow -\sigma$ it is sufficient to evolve only

half of the string worldsheet, $\sigma \leq 0$, and use a reflecting boundary condition at the string midpoint. We used the constraint equations (2.5.45) and (2.5.46) for an independent check of the accuracy of the calculations. The time step $\Delta\tau$ must be chosen to be smaller or equal to the smallest spatial grid distance $\delta\sigma$.

For the numerical simulations we use non-uniform adaptive grid. We use two different adaptive techniques — one type for scattering and another for critical scattering and capture. More details on the numerical scheme can be found in appendix A.

Chapter 4

Scattering of Cosmic String by a Rotating Black Hole: Strong Field Regime

In this chapter we discuss the cosmic string scattering in the strong field regime. In the first section we describe the general features of scattered string profiles, and discuss the properties of string profiles obtained from numerical simulations.

Next we discuss the late time scattering data. In particular, we investigate how the black hole rotation influences the string's displacement in the Y -direction κ . We show that these dependencies can be quantified by simple empiric formulas obtained by data fits. Finally, we study how the width of the kinks depend on the parameters of the string, i.e., the impact parameter b and initial velocity v . We show that formula obtained from weak field approximation fits the data well.

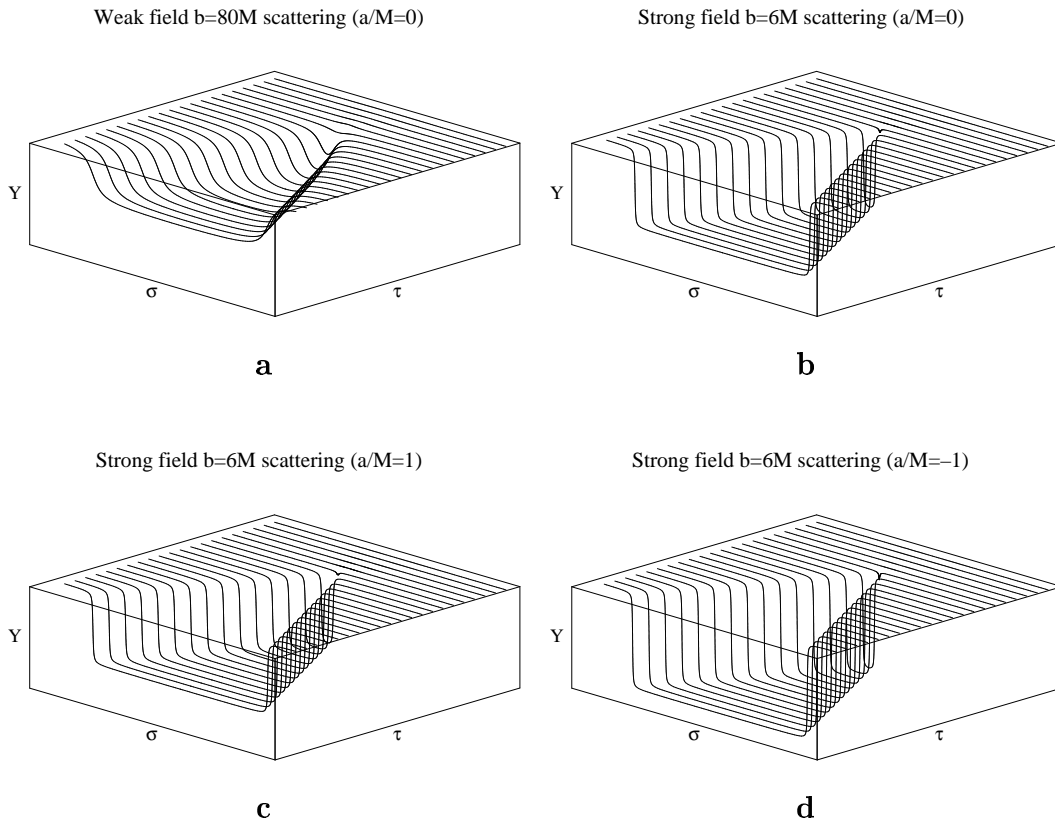


Figure 4.1: Displacement in Y -direction as a function of (τ, σ) for given velocity $v/c = 0.762$ in the weak (a) and strong (b–d) field regime.

4.1 String Profiles for Strong Field Scattering

4.1.1 General picture

Figure 4.1 demonstrates general features of straight string scattering, here for a string with velocity $v = 0.762$ ($\beta = 1$). The four panels show the displacement in the Y -direction as a function of internal coordinates (τ, σ) for weak and strong field scattering.

Figure 4.1 (a) shows the scattering for an impact parameter $b = 80 M$. The value of the displacement parameter at the largest τ shown is $\kappa = 7.23M$. This value as well as the form of the kinks are in a very good agreement with the weak

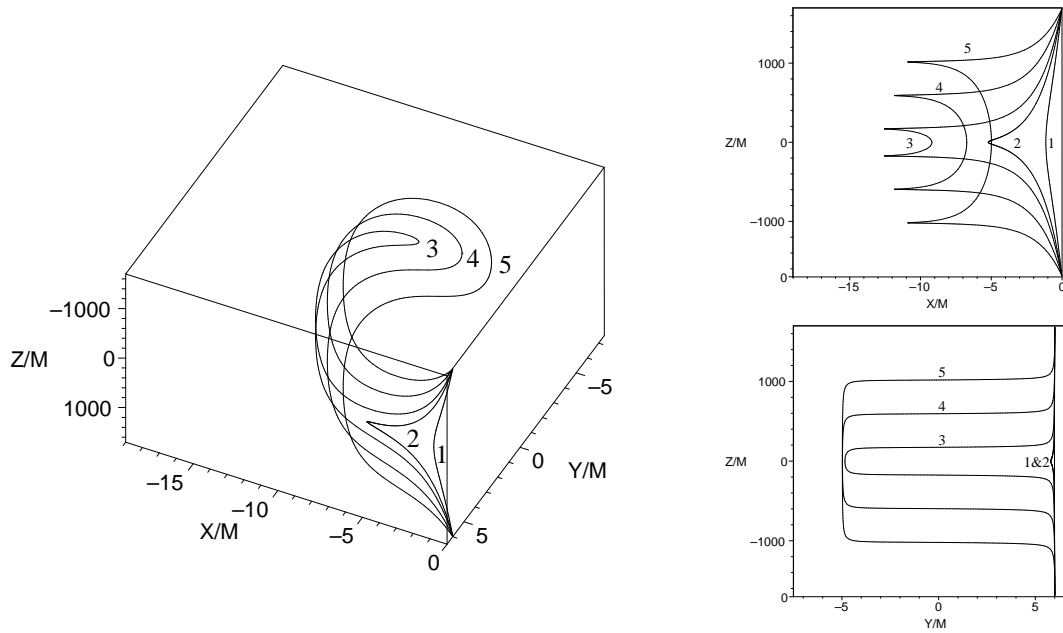


Figure 4.2: “Real-time profiles” of the string and their XZ - and YZ - projection for the strong field scattering by the Schwarzschild black hole.

field scattering results. Plots for prograde and retrograde scattering at $b = 80 M$ are virtually indistinguishable from Fig. 4.1 (a).

Figures 4.1 (b–d) show the scattering for $b = 6 M$. Qualitatively these plots are similar to weak field scattering. The main differences are the following: (1) The value of the displacement parameter $\kappa = 11.03M$ for the non-rotating black hole is significantly larger than $\kappa = 7.23$ for $b = 80 M$. (2) Effects of rotation are more pronounced. The displacement κ for retrograde scattering is essentially larger than κ for the prograde scattering. (3) The string profile after scattering is more sharp, the width of the kinks is visibly smaller than for weak field scattering.

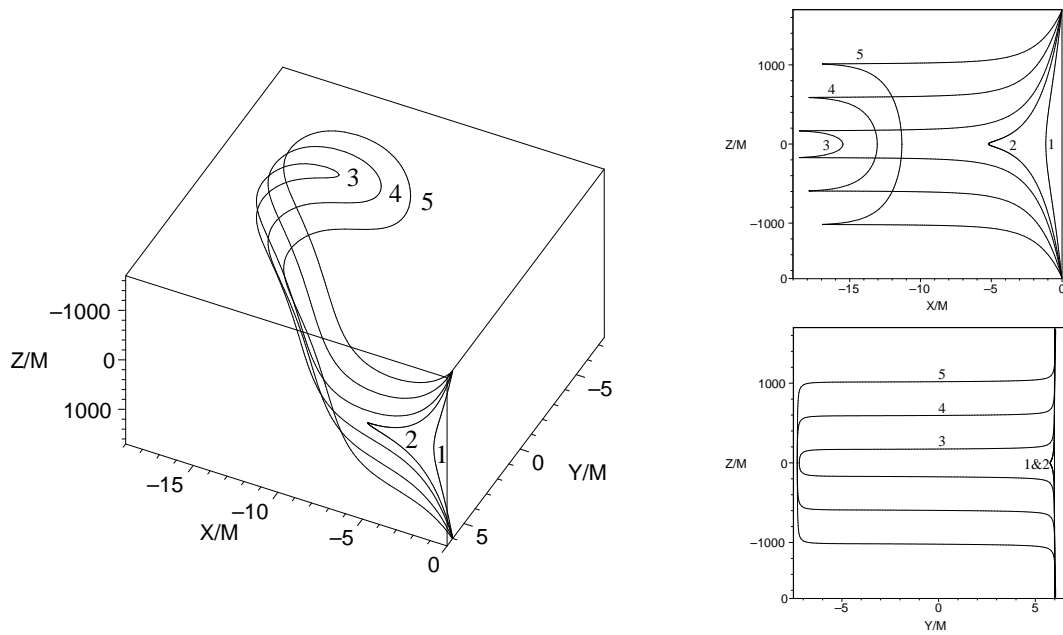


Figure 4.3: “Real-time profiles” of the string and their XZ - and YZ - projection for the strong field retrograde scattering by the extremal Kerr black hole.

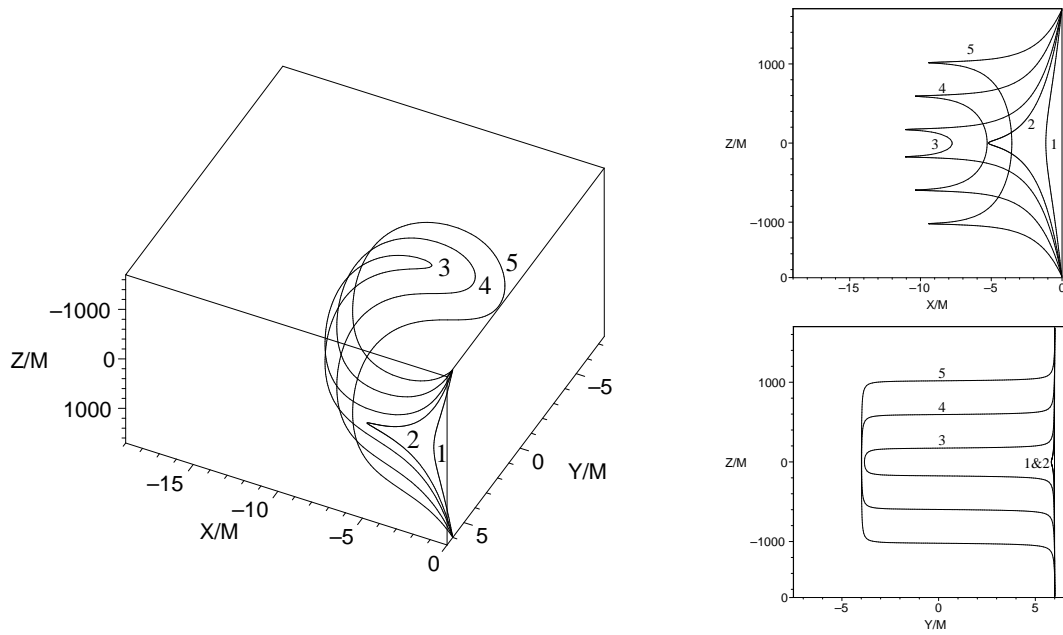


Figure 4.4: “Real-time profiles” of the string and their XZ - and YZ - projection for the strong field prograde scattering by the extremal Kerr black hole.

4.1.2 “Real-time profiles” of the string for strong field scattering

It should be emphasized that figure 4.1 gives an accurate impression of the displacement effect, but it gives a distorted view of the real form of the string. The reason is evident. The grid imposed on the worldsheet is determined by the choice of (τ, σ) coordinates which are fixed by the gauge conditions (2.5.45)–(2.5.46). But a $\tau = \text{const}$ section differs from a time $T = \text{const}$ section in the laboratory slice of spacetime. The position of the string at given time T can be found by using the solution $\{T(\tau, \sigma), X(\tau, \sigma), Y(\tau, \sigma), Z(\tau, \sigma)\}$ to obtain functions $X(T, \sigma)$, $Y(T, \sigma)$ and $Z(T, \sigma)$. For fixed T these functions determine a position of the string line in three-space¹.

Figures 4.2, 4.3 and 4.4 show a sequence of “real-time” profiles for strong-field string scattering at five different coordinate times T . We ordered them so that the larger number labeling the string corresponds to later time. In figure 4.2 the black hole is non-rotating. Figures 4.3 and 4.4 show the “real-time” profiles for retrograde and prograde scattering for a maximally rotating black hole, respectively. Again we can see that due to frame dragging, the distortion of the string is more pronounced for retrograde scattering.

4.2 Late Time Scattering Data

4.2.1 Displacement parameter

Figures 4.5–4.7 show the dependence of the displacement parameter κ on the impact parameter b for different velocities v . For a given value of b the curve for $a/M = -1$ always lies higher than the curves for more positive values of a/M .

¹The procedure of finding the real time string profiles is described in section A.5.

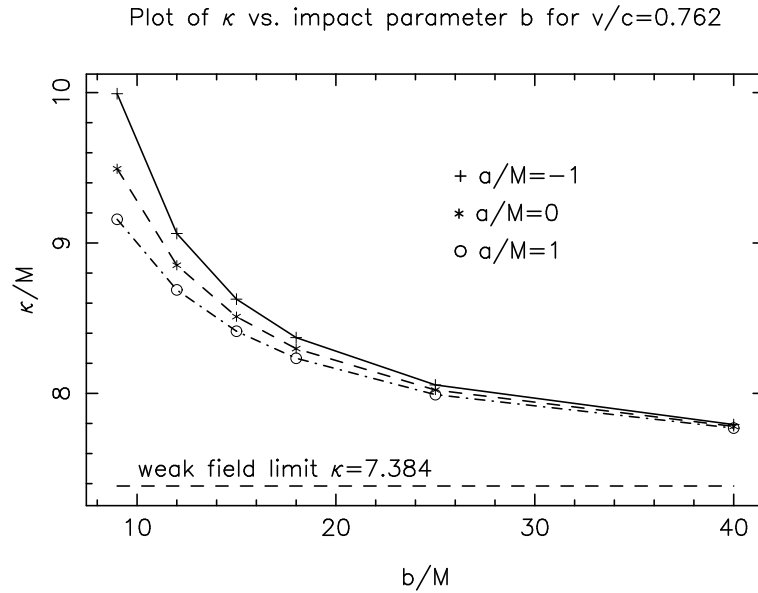


Figure 4.5: Displacement parameter κ as a function of the impact parameter b for different velocities $v/c = 0.762$.

This is true for all values of velocity v , but this difference is more pronounced at large velocities.

The relative location of the curves for given v and b and different a can be explained by frame dragging. Namely, a string in the retrograde motion is effectively slowed down when it passes near the black hole and hence it spends more time near it. As the result its displacement is greater than the displacement for the prograde motion with the same impact parameter. Let us make an order-of-magnitude estimation of this effect. For this purpose we use the metric (3.1.14). We focus our attention on the Lense-Thirring term and neglect for a moment the Newtonian part. Consider first a point particle moving in this metric with the velocity v and impact parameter b . In the absence of rotation it moves with constant velocity so that $(X = vT, Y = b, Z = 0)$ and the proper time τ is

$$\tau_0 = \sqrt{1 - v^2} T. \quad (4.2.1)$$

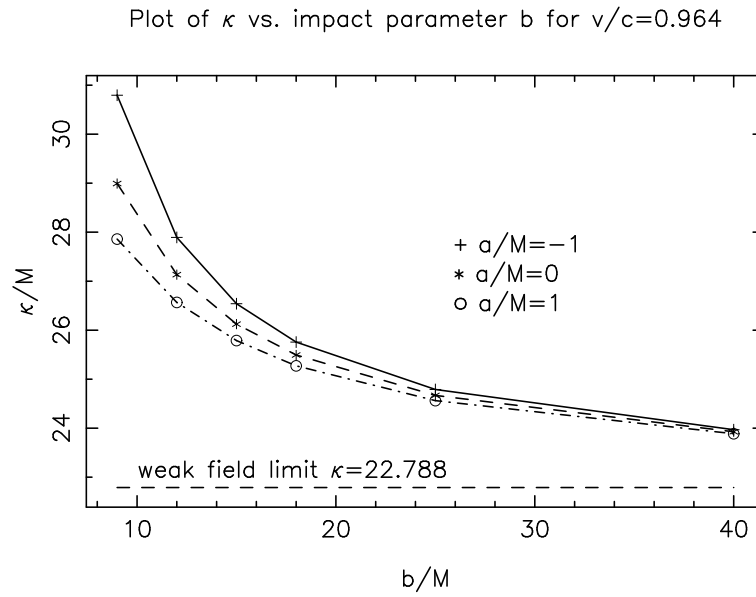


Figure 4.6: Displacement parameter κ as a function of the impact parameter b for $v/c = 0.964$.

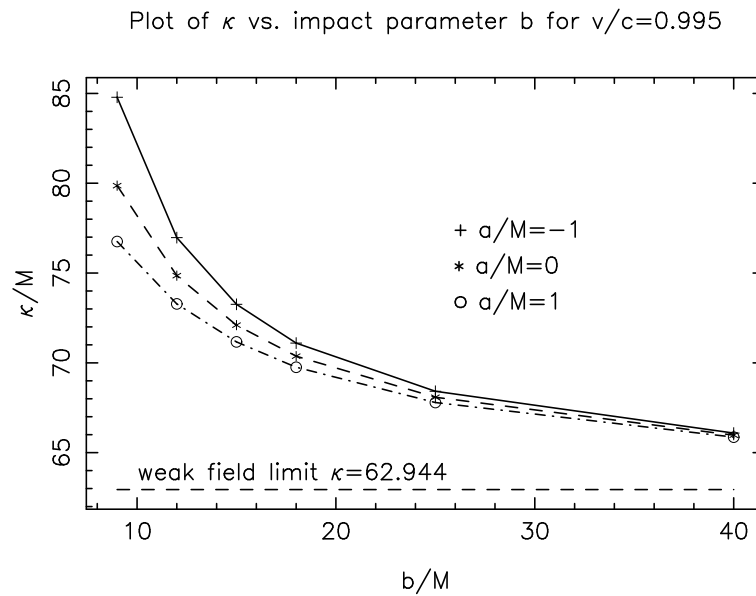


Figure 4.7: Displacement parameter κ as a function of the impact parameter b for $v/c = 0.995$.

In the presence of rotation one has

$$d\tau^2 = (1 - v^2) dT^2 - \frac{4Jbv}{R^3} dT^2, \quad (4.2.2)$$

where

$$R^2 = b^2 + v^2 T^2. \quad (4.2.3)$$

For large b and $\tau_0 \rightarrow \infty$ one can write

$$\tau = \tau_0 + \Delta\tau, \quad (4.2.4)$$

where

$$\Delta\tau = -\frac{2Jbv}{\sqrt{1-v^2}} \int_{-\infty}^{\infty} \frac{dT}{(b^2 + v^2 T^2)^{3/2}} = -\frac{4J}{b\sqrt{1-v^2}}. \quad (4.2.5)$$

This quantity $\Delta\tau$ characterizes the additional time delay for the motion in the Lense-Thirring field. The characteristic time of motion in the vicinity of a black hole is $\tau_{int} \sim b/v$. Thus we have

$$\frac{\Delta\tau}{\tau_{int}} \sim -\frac{4Jv}{b^2\sqrt{1-v^2}}. \quad (4.2.6)$$

One can expect that a similar delay takes place for a string motion. As a result of being longer close to the black hole the string has a larger displacement by the value $\Delta\kappa$ such that

$$\frac{\Delta\kappa}{\kappa} \sim \frac{\Delta\tau}{\tau_{int}} \sim -\frac{4Ma}{b^2} \sinh \beta. \quad (4.2.7)$$

Qualitatively this relation explains dependence of κ on a and β presented in figures 4.5–4.7.

More generally, if we look at $\alpha = a/M$ in the metric as a parameter, we can use perturbation theory to calculate the effect of rotation. The solution \mathcal{X}^A can be expanded in powers of α

$$\mathcal{X}^A = \mathcal{X}^A{}^0 + \alpha \mathcal{X}^A{}^1 + \alpha^2 \mathcal{X}^A{}^2 + \dots, \quad (4.2.8)$$

where $\mathcal{X}^0(\tau, \sigma)$ is the solution for the non-rotating case and $\mathcal{X}^i(\tau, \sigma)$ are the perturbation corrections.

Numerical calculations show that the first two terms in the perturbation series give very good approximation to the solution as long as we are not close to critical scattering. As a consequence

$$\kappa = b - \lim_{\tau \rightarrow \infty} \mathcal{X}^2(\tau, 0) = \kappa_0 - \kappa_1 \alpha - \kappa_2 \alpha^2, \quad (4.2.9)$$

where κ_0 is the Y -displacement for the non-rotating black hole, and κ_1, κ_2 are defined simply as

$$\kappa_{1,2} = \lim_{\tau \rightarrow \infty} \mathcal{X}^{1,2}(\tau, 0). \quad (4.2.10)$$

In the above $\mathcal{X}^{1,2}$ denote the Y -coordinate corrections. The equations of motion for $\mathcal{X}^{1,2}$ are linear and the solution for \mathcal{X}^A can be obtained in one run together with \mathcal{X}^0 (more details can be found in section A.4).

In order to determine the coefficients in equation (4.2.9) we need to extrapolate the relevant data obtained during the simulation to infinity. One possibility is to numerically advance the solution very far from the black hole and simply take the value at the end of the simulation as our estimate. The problem with this approach is that to advance very far by maintaining high accuracy of the solution is a very lengthy process, feasible only for larger impact parameters (since the grid can be sparser).

Our approach was to advance to a moderate distance ($X_{\max} \approx 8000M$) keeping high accuracy of the solution (judged by the constraint equations). Then we fit the calculated data by the function

$$\kappa(0, \tau) = \kappa + k(\tau - \tau_{\text{shift}})^\gamma, \quad (4.2.11)$$

where $\kappa, k, \tau_{sh}, \gamma$ are the parameters to be fitted. We take our first data point at $X = 1000M$. To see how consistent this procedure is and to estimate the errors

we perform three fits with different set of data points. The first set uses all the data points, the second one uses only the first half, and the third one uses only the last half of the data points. For this particular problem the disturbances from the boundary have an adverse effect to the fit, therefore we use the null boundary approach.

Our experience shows that the fitting procedure for κ works much better for larger velocities and larger impact parameters. For the velocities $v/c = 0.762, 0.964, 0.995$ the estimated values of κ from all three fits are consistent and differ by no more than 3%². This fact gives us reasonable confidence that the plotted values of κ indeed represent the true values.

Unfortunately, the situation is not so good for slower velocities. For example for the case $v/c = 0.462$ the slope of the fitted function $\kappa(0, \tau)$ is almost constant during the later phases of the simulation, and fits using different sets of data points yield inconsistent (and improbable) values of κ . We expect the behavior of $\kappa(0, \tau)$ to change but we did not see it in our data even after driving the simulation four times further then for the other velocities ($X_{\max} \approx 32,000M$). Again, this behavior is more pronounced for smaller impact parameters b .

To obtain the values for κ_1 and κ_2 we use the same method as for κ . We did not encounter any difficulties in estimating the values of κ_1 and κ_2 for any of the four velocities. The trend here is the opposite of the one for κ – the fits work best for smaller velocities and smaller impact parameters. The fits with different set of data points are typically less than 1% apart.

Figures 4.8 and 4.9 show the results in a log-log plot. Figure 4.10 shows the plot of κ_1/κ , which is proportional to $\Delta\kappa/\kappa$. The straight lines shown are obtained from least square fit. Note that the plots for the velocities $v/c = 0.964$ and $v/c = 0.995$ lie on top of each other.

²For $b \geq 12M$ the results from the three fits differ by less than 1%.

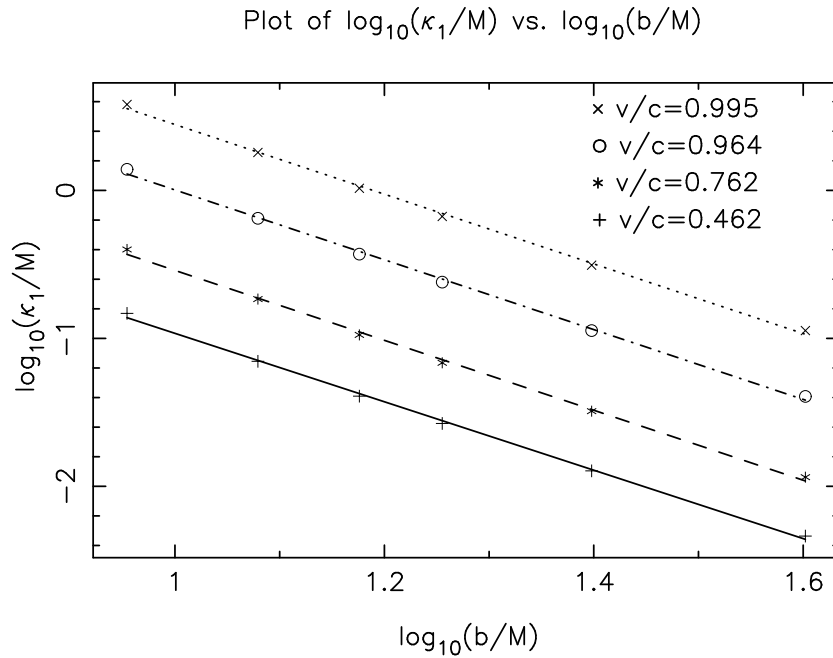


Figure 4.8: Plot of κ_1 for different velocities v and impact parameters b . The straight lines represent a linear fit.

In the interval shown κ_1 and κ_2 can be reasonably approximated by a functions of the form

$$\kappa_{1,2} \approx A_{1,2}(v) \left(\frac{1}{b}\right)^{\lambda_{1,2}}. \quad (4.2.12)$$

Similarly for κ_1/κ ,

$$\frac{\kappa_1}{\kappa} \approx A_3(v) \left(\frac{1}{b}\right)^{\lambda_3}. \quad (4.2.13)$$

The values for $A_{1,2,3}$ and $\lambda_{1,2,3}$ obtained from a linear fit are shown in table 4.1. By comparing (4.2.13) with (4.2.7) one can conclude that the numerical value $\lambda_3 = 2.23$ is close to the value 2, which is what is given by the relation (4.2.7).

Note that the last data point on the plot for κ_2 is a bit out of a straight line. We are not sure if this is a genuine feature or simply inaccurate data points (e.g., due to round-off errors)³. We did not include this data point into calculation of

³The discrepancies are larger than those which could result from the extrapolation proce-

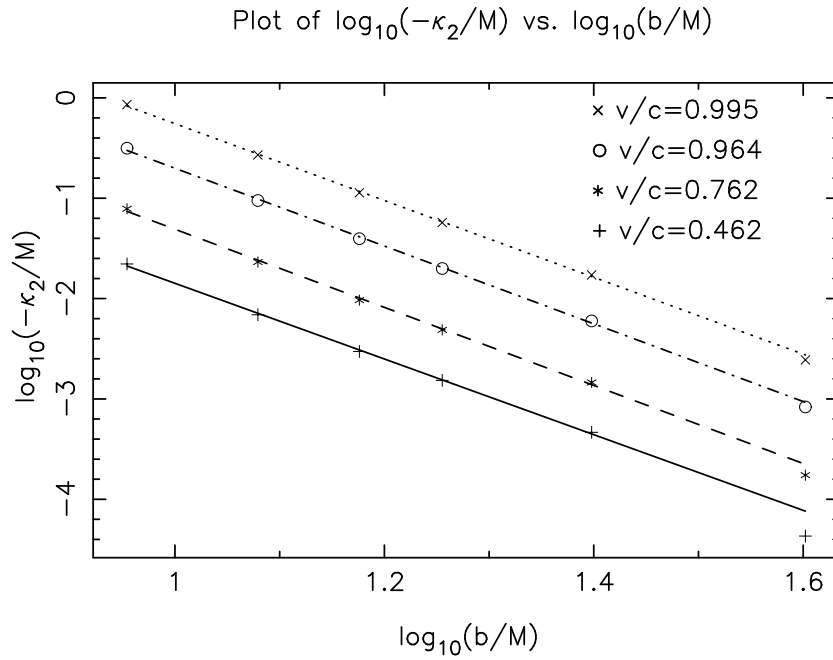


Figure 4.9: Plot of κ_2 for different velocities v and impact parameters b . The straight lines represent a linear fit.

the values in table 4.1.

v/c	0.462	0.762	0.964	0.995
A_1	22.3	66.6	231.0	631.6
λ_1	2.31	2.36	2.36	2.35
A_2	-83.9	-381.4	-1487.9	-3717.0
λ_2	3.77	3.89	3.87	3.83
A_3	-	5.42	6.21	6.17
λ_3	-	2.23	2.23	2.23

Table 4.1: Values of fitted parameters from equation (4.2.12) and (4.2.13)

dure.

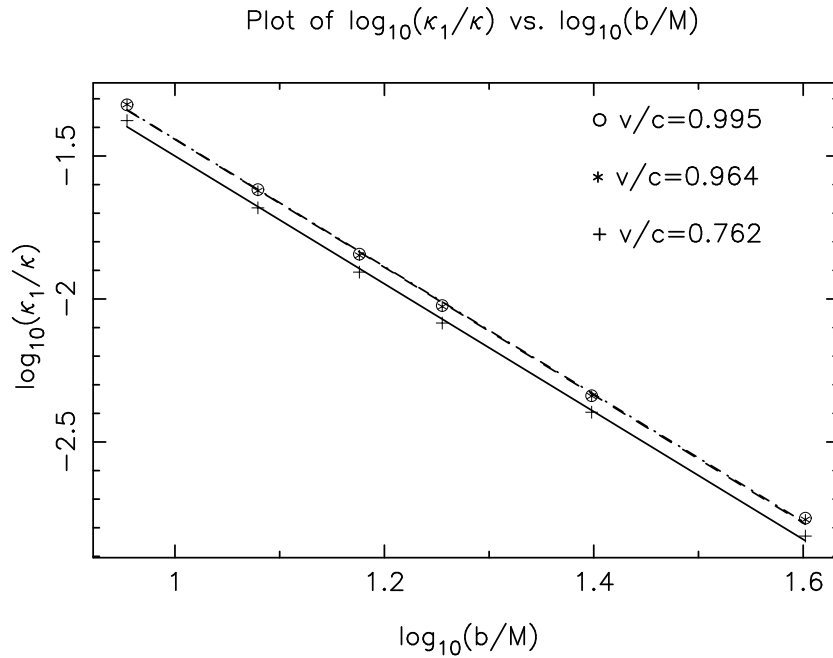


Figure 4.10: Plot of κ_1/κ for different velocities v and impact parameters b . The straight lines represent a linear fit.

4.2.2 Form of the kinks

Figure 4.11 shows details of the transition from the “old phase” to the “new phase” for two different impact parameters. We see that the width of the kinks differs significantly. In general the width also depends on the velocity v/c . The dependence of the kink width on velocity and the impact parameter can be estimated by using the weak field approximation as

$$w \sim \frac{bc}{v} . \quad (4.2.14)$$

We operationally define the width of the kink to be the width of the peak of $dY/d\sigma$ at 1/20-th of its height. Figure 4.12 shows comparison of the kink widths obtained from simulation with a function

$$w_{\text{analyt}} = 7.14 \frac{bc}{v} . \quad (4.2.15)$$

The numerical constant was obtained by a fit. The match with the data is surprisingly good.

We also noticed that the dependency of the width of the kink on the rotation parameter a is rather small. In general

$$w_{a/M=1} < w_{a/M=0} < w_{a/M=-1} . \quad (4.2.16)$$

For the parameters shown on figure 4.12 the rotation made a difference in kink width from $3M$ to $7M$ for the extremal black holes.

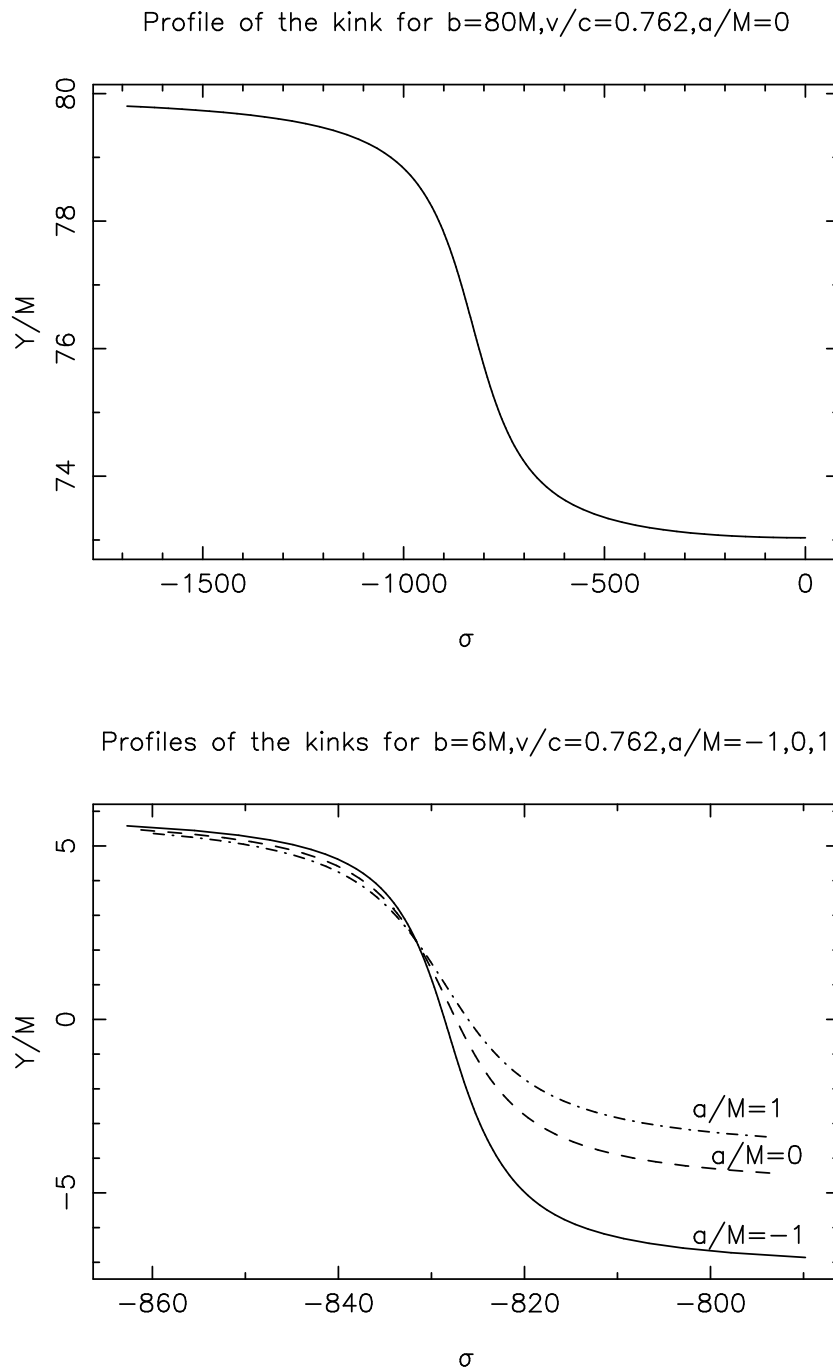


Figure 4.11: Profiles of the kinks for different impact parameters

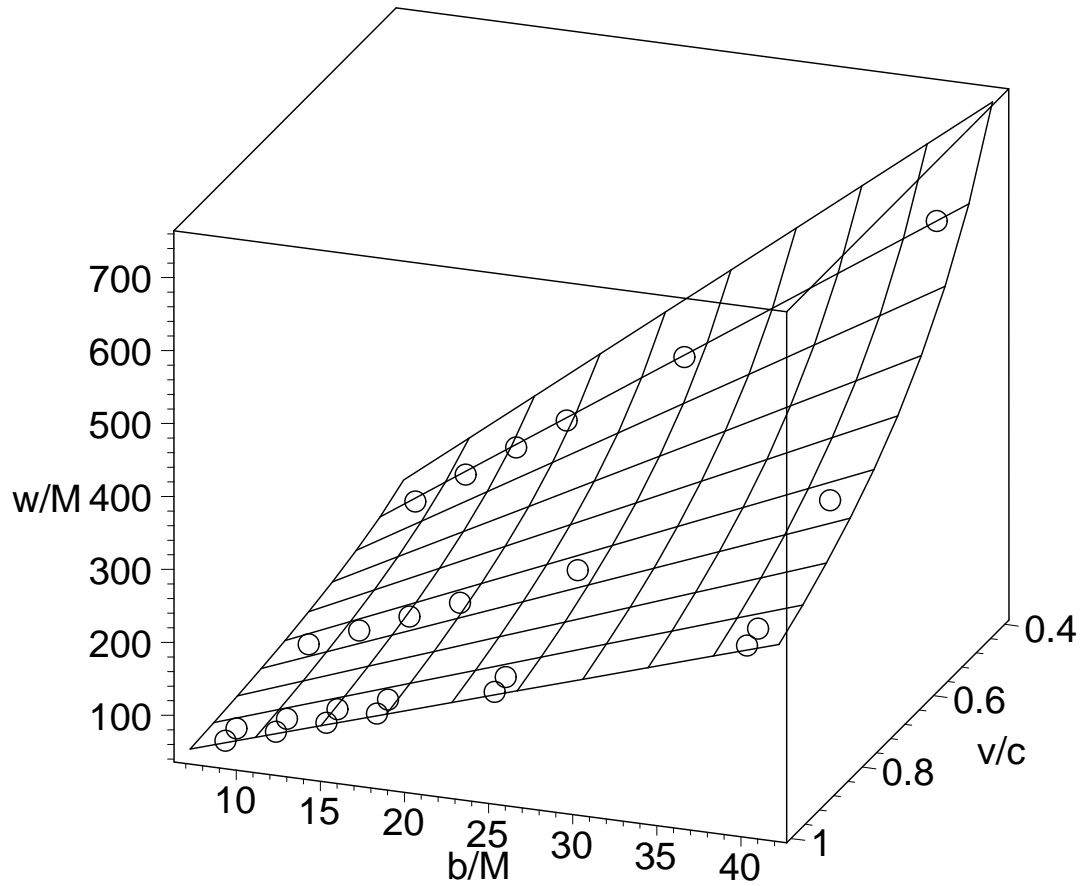


Figure 4.12: Comparison of kink widths for $v/c = 0.462, 0.762, 0.964, 0.995$ and impact parameters $b/M = 9, 12, 15, 18, 25, 40$ obtained from simulation (circles) and the analytic approximation (4.2.15). The data shown are taken for $a/M = 0$.

Chapter 5

Critical Scattering and Capture

In this chapter we discuss critical scattering and capture of cosmic strings by a rotating black hole.

In the first section we discuss the critical impact parameter curves obtained from numerical simulations. We present an analytical formula obtained from linear fits approximating the critical impact parameter curves for different values of black hole angular momentum and initial velocity v . We also discuss the peculiar shape of critical impact parameter curves for relativistic strings moving in nearly extremal Kerr spacetime.

In the next section we focus on the critical scattering of cosmic strings. Critical scattering is characterized by impact parameters close to the critical value b_c . Real-time profiles and late time scattering data of such strings exhibit distinctive features not present for non-critically scattered strings.

In the last section we analyze the conditions for coil formation. Formation of coils is a relativistic effect and as will be seen from the data it is also influenced by the black hole rotation.

5.1 String Capture and Critical Impact Parameter

Two outcomes are possible for the string evolution—scattering and capture. Capture occurs when a part of the string enters the event horizon of the black hole located at

$$r = M + \sqrt{M^2 - a^2}. \quad (5.1.1)$$

Since the Kerr in-going coordinates are regular at the event horizon we can trace the string evolution both in the black hole exterior and interior. For our study of the string capture we stop our calculations as soon as part of the string crosses the horizon. The value of $b_c(v)$ is determined as follows. For each fixed velocity v and angular momentum a we start the search with two values of b —one for which the string is captured and one for which it escapes. Then we use bisection method to bracket the critical impact parameter¹. The results of these calculations are shown in figure 5.1. The error bars are smaller than the data markers so they are not shown.

This plot contains the critical impact parameter curves for 9 different values of the rotation parameter a from $a = -M$ to $a = M$. The signs are chosen so that a negative value of a corresponds to a retrograde motion of the string and positive value to a prograde one. The lower the value of a the higher is the position of the critical impact parameter curves in the (v, b_c) -plane. This feature is easily explained by the *dragging into rotation* effect. Indeed, for the retrograde motion the dragging effect slows down the string's motion. The string spends more time in the strong attractive field of the black hole and hence it can be captured easier. In order to escape the capture the string must be moving with

¹This algorithm must be used with caution when the critical impact parameter curve contains multiple branches.

Critical impact parameter curves for various angular momenta

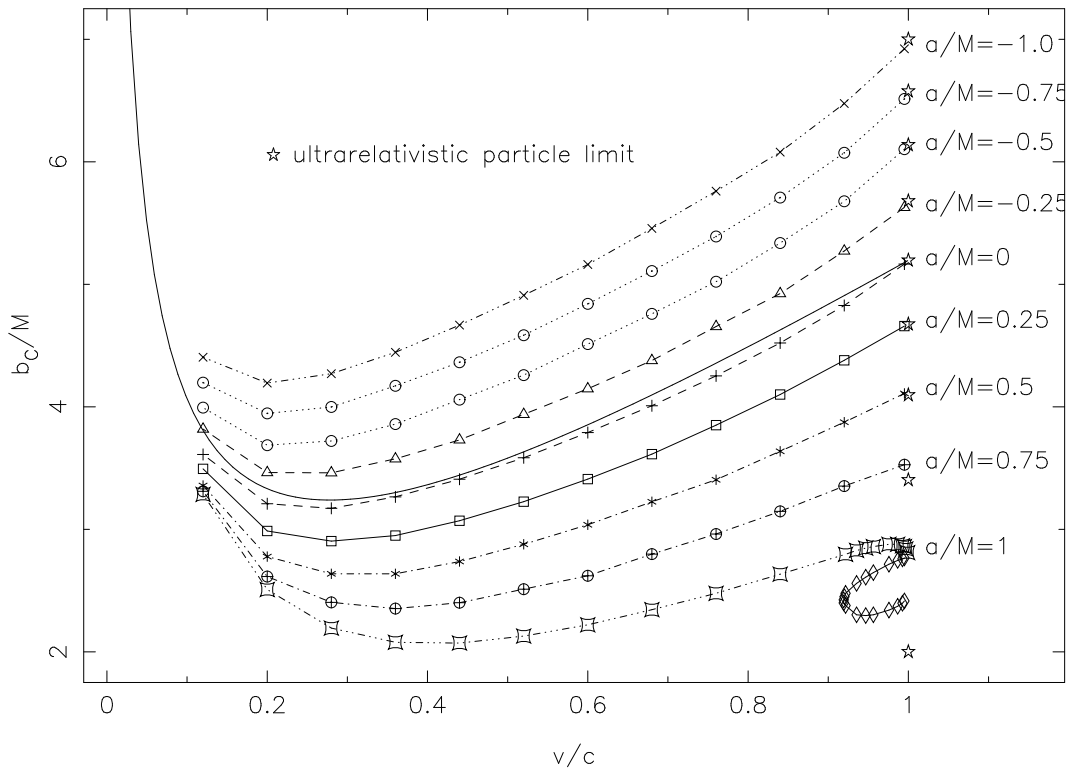


Figure 5.1: Critical impact parameter b_c as a function of the string's initial velocity v . The solid line represents Page's approximation for Schwarzschild black hole (formula (5.1.2)).

larger impact parameter. Thus the critical impact parameter is larger than that for a non-rotating black hole. For the prograde motion the effect is opposite.

Numerical calculations were done for $v/c > 0.12$. For smaller velocity the impact parameter becomes large and computational time grows. On the other hand, for large impact parameters the main part of the time evolution of the string occurs in the weak field region. One can use this to estimate the critical impact parameter for low velocity motion [19, 20]. Combining low velocity dependence with the result for the ultrarelativistic scattering of particles Page

proposed the following approximation for the critical impact parameter [20]

$$b_c/M = \left(\sqrt{\frac{\pi}{2v}} - \sqrt{\frac{\pi}{2}} \right) - \frac{64}{15} (1 - v) + 3\sqrt{3}. \quad (5.1.2)$$

This function is shown in figure 5.1 as a solid line. One can see that it gives quite good approximation for a non-rotating black hole. For rotating black holes this line gives good approximation for small v since for large impact parameters the rotation plays less important role.

We obtain the generalization of the Page approximation (5.1.2) to the case of a rotating black hole. Notice that in the ultrarelativistic limit $v/c \rightarrow \infty$ the critical impact parameter for the string coincides with the critical impact parameter for photons². The critical impact parameter for particles in the ultrarelativistic limit is given by (3.2.61). The value of b_c^{part} for $a/M = 0, \pm 0.25, \pm 0.5, \pm 0.75, \pm 1$ is shown by stars on figure 5.1 on the vertical line at $v/c = 1$. These points are very close to those belonging to an ultrarelativistic string. The only exception is a region of a/M close to 1.

Page's approximation for critical impact parameter curves can be generalized to the case of a rotating black hole. We can write the corresponding ansatz in the form

$$b_c^{fit}/M = \left(\sqrt{\frac{\pi}{2v}} - \sqrt{\frac{\pi}{2}} \right) - (b_0 + b_1 a + b_2 a^2) (1 - v) + b_c^{part}/M. \quad (5.1.3)$$

The best fit for numerically calculated critical impact parameter curves gives the following values of the fitting parameters b_i

$$b_0 = 4.40, \quad b_1 = -1.55, \quad b_2 = -0.53. \quad (5.1.4)$$

We see that the fitted value of b_0 agrees well with the Page's value $64/15 \approx 4.27$. Figure 5.2 shows the result of the fitting for values of $a/M = 0, \pm 0.25, \pm 0.5,$

²The only exception is a case of prograde scattering by a nearly extreme black hole. The complicated structure of the critical impact parameter curve for this case is connected with the features of the critical scattering which we discuss later.

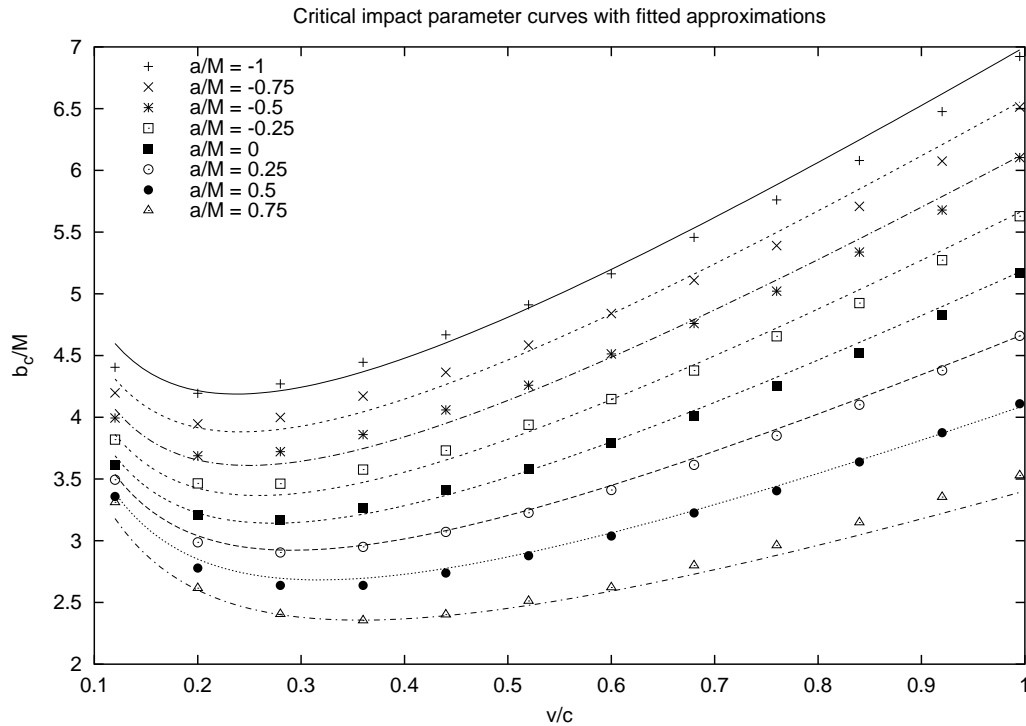


Figure 5.2: Critical impact parameter b_c and its fitted approximation b_c^{fit} as functions of the string's initial velocity v for different values of the rotation parameter a/M .

± 0.75 , -1 . (We exclude $a/M = 1$ because of the peculiar behavior of the critical impact parameter curve for this case.) It is easy to see that continuous curves representing b_c^{fit} given by (5.1.3)–(5.1.4) are in a good agreement with the numerical data shown by shaped points.

Let us discuss an additional new feature in the critical impact curves which occurs for highly relativistic prograde scattering by rapidly rotating black holes. The plot for $a/M = 1.0$ presented in figure 5.1 shows that in this regime $b_c(v)$ becomes a multiply valued function of v . We studied numerically this regime. Figure 5.3 shows the corresponding region in more details. It contains plots of

Details of the critical impact parameter curves for $a/M=0.9$ and $a/M=1.0$

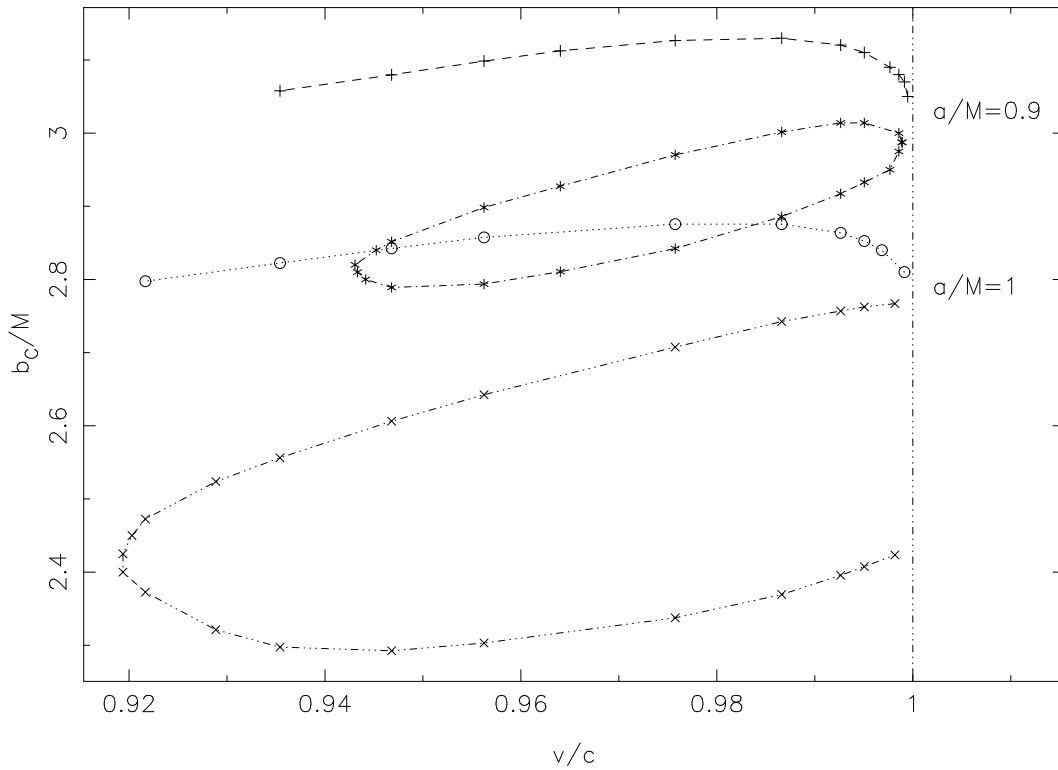


Figure 5.3: Critical impact parameter curve for a prograde scattering of a relativistic cosmic string by a rapidly rotating black hole.

$b_c(v)$ near $v/c = 1$ for two values of the rotation parameter— $a/M = 0.9$ and $a/M = 1.0$. Besides the main branch curve (marked by ‘+’ for $a/M = 0.9$ and by ‘o’ for $a/M = 1.0$) there also exists an additional branch (marked by ‘*’ for $a/M = 0.9$ and by ‘x’ for $a/M = 1.0$). We performed calculations up to $v/c = 0.9995$ which corresponds to the gamma-factor $\gamma \approx 30$. For greater values of γ our program does not allow us to obtain the solution with the required accuracy.

For given velocity v and the impact parameter lying just below the main branch the string is captured. But if the value of impact parameter lies inside

the closed loop, the string is again able to escape to infinity. We call this peculiar behavior of critical strings the *escape phenomenon*. At first glance this behavior looks quite strange. We discuss the mechanism which makes these types of motion possible in the next section.

5.2 Critical Scattering

5.2.1 Real-time string profiles

As we saw in the previous section the critical impact parameter curve is more complicated in the ultrarelativistic regime for a rapidly rotating black hole. This can be better understood from the way the string is scattered in the critical regime. Figures 5.4–5.6 illustrate this. Each of the figures contains a set of snapshots made at some moment of coordinate time T . We call such a snapshot a *real-time profile*. The time is given in units of GM/c^3 . $T = 0$ corresponds to the moment when the parts of the string located far from the black hole (where the spacetime is practically flat) pass the $X = 0$ plane. The black hole event horizon is depicted as a black spot. It should be noted that the scales along different axes are different. That is the reason why instead of a sphere the spot representing the black hole event horizon looks like an ellipsoid.

There are two basic modes how a string can escape. In the "standard" mode the string passes the black hole with its center partially wrapped around it (figure 5.4, (a)–(b)). As the rest of the string escapes the central part unwraps and the string escapes to infinity (figure 5.4, (c)–(d)). As we lower the impact parameter the central part wraps more around the black hole and ultimately it does not have enough time to unwrap and it gets captured. However, if we lower the impact parameter under a certain value the string can escape again. Now the mechanism is different. In this "alternative" mode the string wraps around the

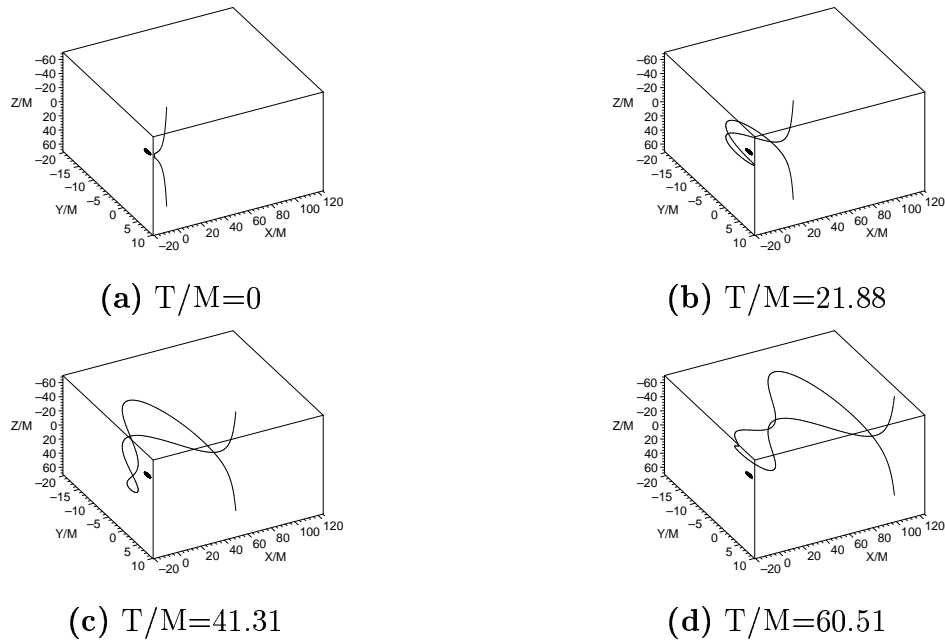


Figure 5.4: Real-time profiles of the cosmic string: $v/c = 0.995$, $a/M = 1$ and $b/M = 2.9$.

black hole as in the "standard" mode (figure 5.5, (a)–(b)) but this time, instead of unwrapping, the black hole slips through the open coil (figure 5.5, (c)–(d)). For even smaller values of the impact parameter this mechanism breaks down eventually and the string is captured again. Although it is possible that there exist other "islands of escape" below the lowest branch of the critical impact parameter curve we did not observe it in our simulations.

To have a better picture of the two different escape modes we created three MAPLE animations, each corresponding to one of the figures 5.4–5.6. These can be found at the URL <http://www.phys.ualberta.ca/~frolov/CSBH>. Note that the animations show only the central part of the string. In the animations the rate of time is "slowed down" when the string is close to the black hole in order to make the details of the string behavior more clear. For this reason it seems that the string starts moving more rapidly when all its parts leave the proximity of

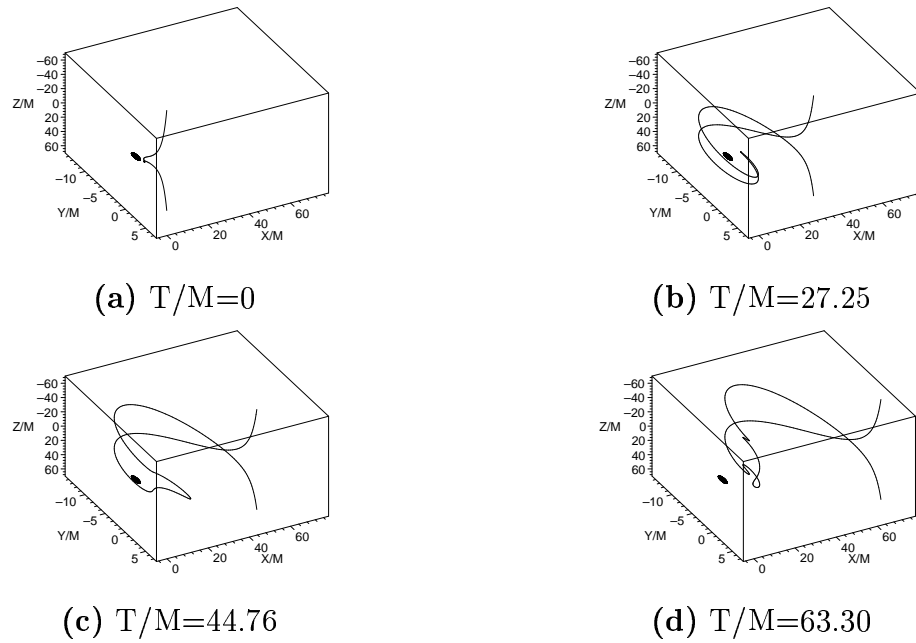


Figure 5.5: Real-time profiles of the cosmic string: $v/c = 0.995$, $a/M = 1$ and $b/M = 2.55$.

the black hole.

Interesting features of the string structure are connected with *wrapping effect*, that is, when the central part of the string rotates around the black hole at the angle greater than 2π . Such wrapping type of motion is characteristic for the motion of the ultrarelativistic particles in the regime close to capture. The tension of the string makes this effect less profound. One can expect that for highly ultrarelativistic motion it occurs even for a non-rotating black hole. We do not see this effect in our simulations since we can not perform sufficiently accurate calculations for ultrarelativistic velocities with the rapidity factor beyond $\beta \approx 4.0$. The dragging effect connected with the rotation of the black hole makes this effect more profound. Figure 5.6 shows real time profiles for the string which "wraps" around the black hole. It is interesting that during this process sharp

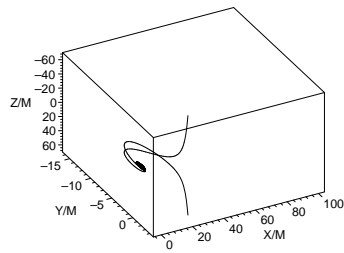
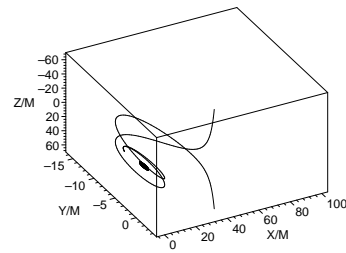
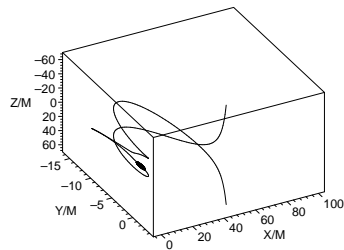
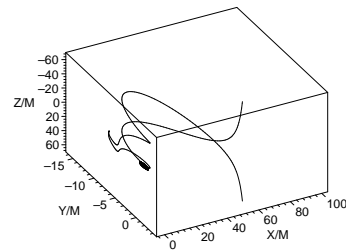
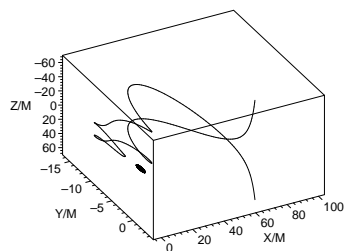
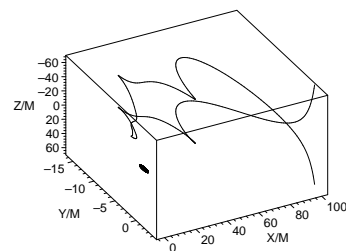
(a) $T/M=15.13$ (b) $T/M=30.19$ (c) $T/M=40.10$ (d) $T/M=48.57$ (e) $T/M=58.87$ (f) $T/M=95.65$

Figure 5.6: Real-time profiles of the cosmic string: $v/c = 0.995$, $a/M = 1$ and $b/M = 2.4125$.

spikes are formed in the string profiles³.

³These spikes are not infinitely sharp however, so the appropriate derivatives are well defined.

5.2.2 Late time scattering data

For critical scattering the central part of the string spends some time in the vicinity of the black hole while the further located parts of the string keep moving forward. After the central part of the string leaves the black hole vicinity the string as a whole is moving away from the black hole with the central part excitations propagating along the string. The combination of these effects results in quite a rich structure of the late time string profiles. Figures 5.7–5.10 illustrate this.

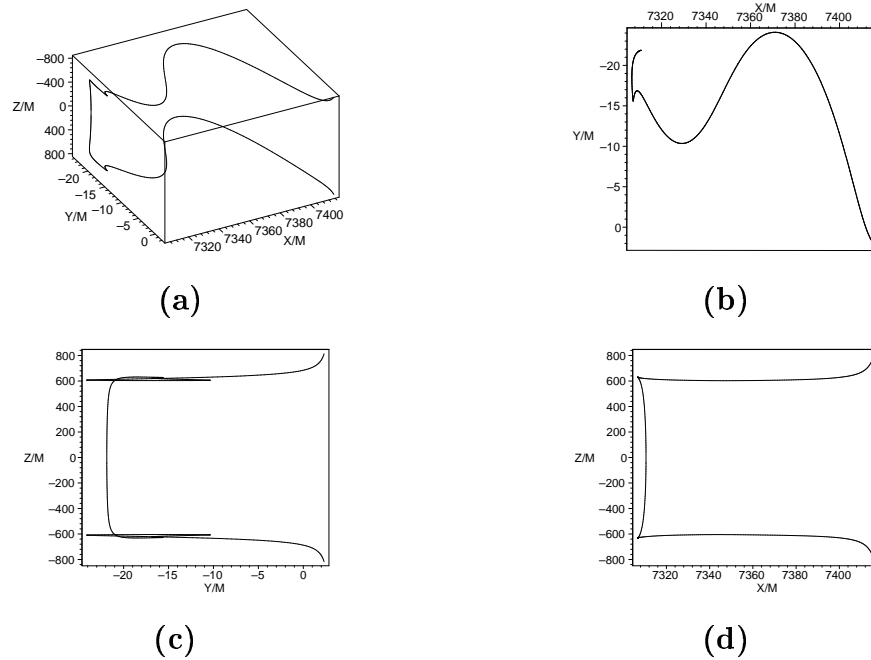


Figure 5.7: Late time profiles of the cosmic string: $v/c = 0.995$, $a/M = 1$ and $b/M = 2.9$, $T/M = 7446.47$.

Each of these figures consists of four plots. They demonstrate the form of the string some time after it passes close to the black hole. The black hole left behind the string is not shown. We show only that part of the string near the center which contains interesting details. The strings depicted on the figures 5.7–5.9 differ only by their initial impact parameter b . They are scattered by an extremal

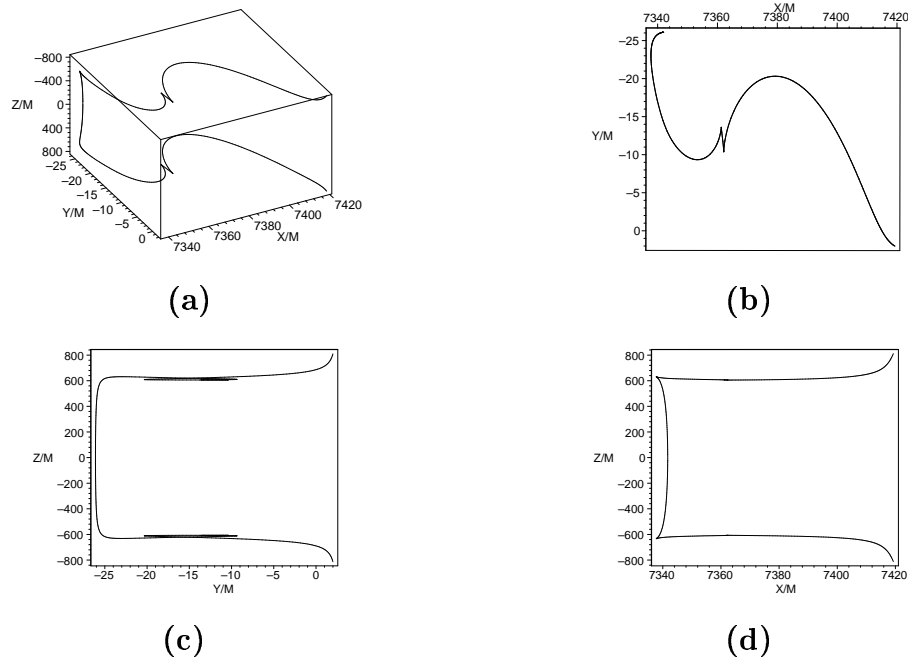


Figure 5.8: Late time profiles of the cosmic string: $v/c = 0.995$, $a/M = 1$ and $b/M = 2.55$, $T/M = 7448.56$.

black hole in the prograde direction. For comparison figure 5.10 shows the late time profiles of a critically scattered string by a Schwarzschild black hole. Plots (a) show the real-time three-dimensional space profile of the string, while plots (b), (c), and (d) show two-dimensional projections onto the planes XY , YZ , and XZ , respectively. One can easily observe that at this relatively late time when the interaction with the black hole becomes weak the part of the string close to the center looks practically as a segment of a straight line. This property is also characteristic for a generic (non-critical) string scattering. In section 4.2 we demonstrated that for this case, as a result of scattering, the central part of the string ‘shifts’ into the Y -direction and a new ‘phase’ is formed. This new phase is that region of the string which is moving in the plane parallel to the initial one, but is displaced by some value ΔY in the Y -direction. The length of the string segment in the new phase grows with the velocity of light, the transition

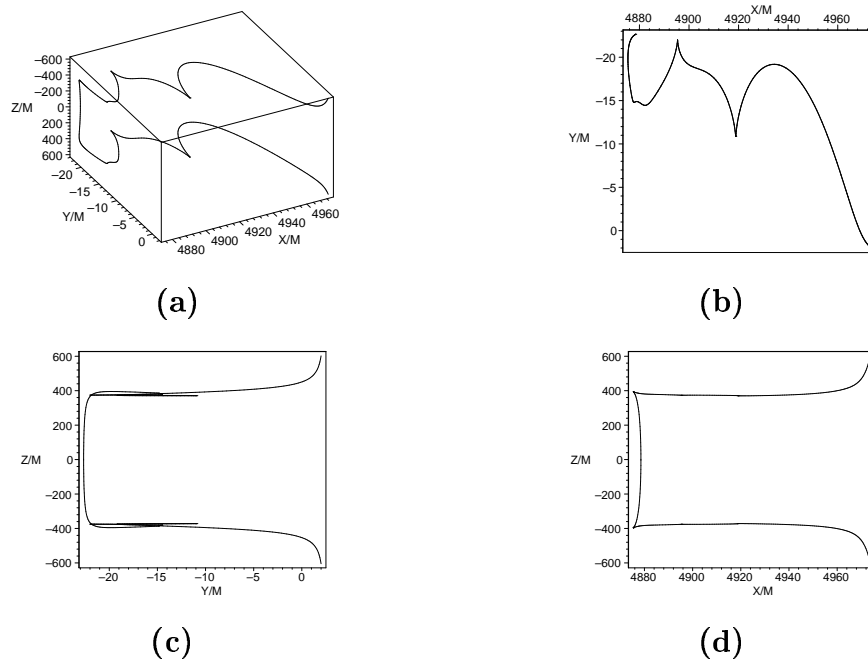


Figure 5.9: Late time profiles of the cosmic string: $v/c = 0.995$, $a/M = 1$ and $b/M = 2.4125$, $T/M = 4991.53$.

layers being kink-like profiles. Similar picture is valid also in the critical regime, as one can see by comparing plots (c) at figures 5.7–5.10. An important new feature is the possibility that the points with maximum shift in Y -direction may be located not at the center of the string, but slightly aside. Figure 5.7 (c) shows that there are two such points located symmetrically with respect to the center.

The XZ -profiles (plots (d) at figures 5.7–5.10) are also quite regular and resemble similar profiles for a non-critical scattering. On the contrary, the XY -profiles (plots (b) at figures 5.7–5.10) are rich of details. The spikes in the string shape are most profound in this projection. All these details are connected with a simple fact that the central part of the string spends considerable time moving near the black hole, while the other parts of the string are moving away practically with the velocity of light. The profiles are sharper for the strings scattered by a rotating black holes. One can expect that by fine tuning the impact parameter

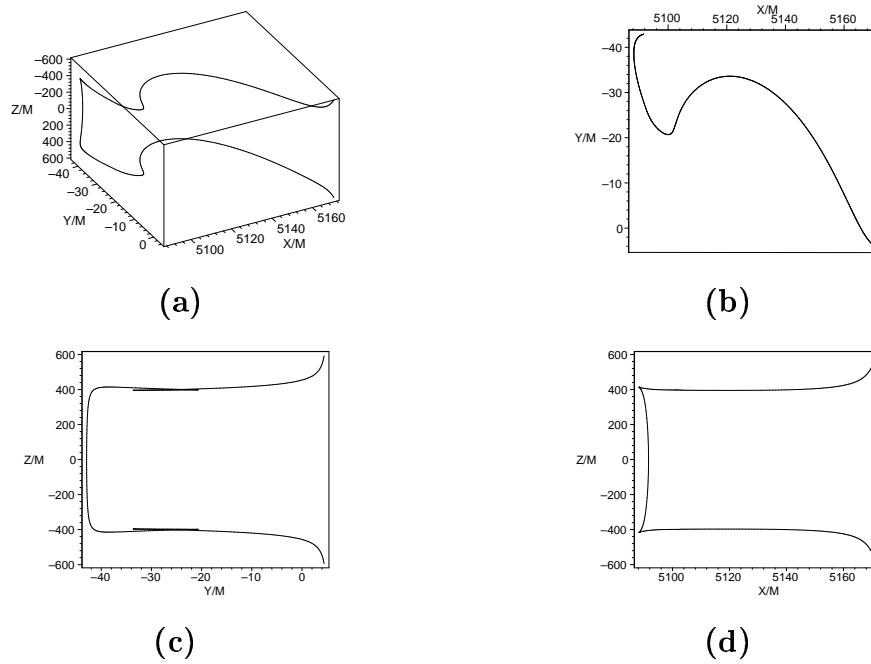


Figure 5.10: Late time profiles of the cosmic string: $v/c = 0.995$, $a/M = 0$ and $b/M = 5.17$, $T/M = 5209.56$.

one might be able to obtain string configurations which remain ‘glued’ to the vicinity of the black hole for arbitrary long time. But one can also expect that such solutions are very unstable, so that a tiny change of the impact parameter either results in the capture of the string or in its earlier escape. This situation is similar to the one discussed in [38], where it was demonstrated that axially symmetric motion of a circular string in the gravitational field of Schwarzschild black hole is chaotic. One can make a conjecture that the critical scattering of the cosmic string is also chaotic.

5.3 Coil Formation

There exists a special regime of the string scattering when after passing nearby a black hole the string forms a *coil*. A coil arises when the function $Z(\tau, \sigma)$

loses its property to be a monotonous function of σ at fixed τ_0 . In this case there exist two different values σ_0 and $-\sigma_0$ for which the value of Z is zero, $Z(\tau_0, \sigma_0) = Z(\tau_0, -\sigma_0) = 0$. Since all other coordinates are symmetric functions of σ , the point $(\tau_0, \pm\sigma_0)$ is in fact a point of the string self intersection. A coil exists for some finite time interval from τ_i till τ_f . At the end points of this interval $\partial_\sigma Z|_{\sigma=0} = 0$.

It should be emphasized that, because of the interconnection effect, for most of the string models any self-crossing of the string results in the formation of a loop. After this, the loop moves independently from the remaining part of the string. In our simulations we did not include this effect. For this reason, such details as a coil size and structure may not represent the real properties of the string after its self-intersection. On the other hand, before the intersection occurs the numerical simulation describes the correct picture. That is why we focus our attention on the form of the *coil formation curve*. This is a curve (or surface) in the space of parameters which separates the region without coils from the region with coils. The structure of the coil formation curve does not depend on the details of the loop formation process.

Figure 5.11 shows the regions of coil formation for different values of the rotation parameter a . This region lies below the coil formation curves shown in the pictures. From below this region is restricted by the critical impact parameter curve. For a point lying exactly on the coil formation curve one has $\tau_i = \tau_f = \tau_*$. It means that $\partial_\sigma Z|_{\sigma=0}$ has a local minimum at this point as a function of τ and hence

$$\partial_\sigma Z|_{(\sigma=0, \tau=\tau_*)} = \partial_\tau \partial_\sigma Z|_{(\sigma=0, \tau=\tau_*)} = 0. \quad (5.3.5)$$

The plots presented in figure 5.11 demonstrate that the formation of coils occurs when a string moves with relativistic velocity. For the prograde motion the coil formation starts at $v/c \approx 0.6$ (see figure 5.11, (c) and (d)). For the

retrograde motion the corresponding velocity is higher and reaches $v/c \approx 0.8$ for the extremally rotating black hole (see figure 5.11 (e) and (f)).

It is instructive to compare these results with the condition of the coil formation in the weak field approximation. To simplify the analysis we work with the weak field solution (3.2.31)–(3.2.38) in the limit $X_0 \rightarrow -\infty$. To calculate the limit it is convenient to choose $X_0 = (\tilde{\tau} - \tau) \sinh \beta$ and, while keeping $\tilde{\tau}$ finite, to send $\tau \rightarrow \infty$. The physical interpretation of the new time-like parameter $\tilde{\tau}$ is quite simple—at $\tilde{\tau} = 0$ the string crosses the $X = 0$ plane⁴.

Omitting the terms vanishing in this limit we obtain

$$Z = \sigma + M \cosh \beta \ln \left(\frac{A_- B_-}{A_+ B_+} \right), \quad (5.3.6)$$

$$\begin{aligned} Y = b - M \sinh \beta \left[\arctan \left(\frac{b^2 + \tilde{\tau}(\tilde{\tau} + \sigma) \sinh^2 \beta}{b \sinh \beta \sqrt{\tilde{\tau}^2 \sinh^2 \beta + b^2 + \sigma^2}} \right) \right. \\ \left. + \arctan \left(\frac{b^2 + \tilde{\tau}(\tilde{\tau} - \sigma) \sinh^2 \beta}{b \sinh \beta \sqrt{\tilde{\tau}^2 \sinh^2 \beta + b^2 + \sigma^2}} \right) \right. \\ \left. + \arctan \left(\frac{(\tilde{\tau} + \sigma) \sinh \beta}{b \cosh \beta} \right) \right. \\ \left. + \arctan \left(\frac{(\tilde{\tau} - \sigma) \sinh \beta}{b \cosh \beta} \right) \right], \quad (5.3.7) \end{aligned}$$

$$X = \tilde{\tau} \sinh \beta, \quad (5.3.8)$$

$$T = \tilde{\tau} \cosh \beta + M \ln \left(4 \frac{B_- B_+}{A_- A_+} \right) + 2M \ln(\tau \cosh^2 \beta), \quad (5.3.9)$$

with

$$A_{\pm} = b^2 \cosh^2 \beta + (\tilde{\tau} \pm \sigma)^2 \sinh^2 \beta, \quad (5.3.10)$$

⁴In the weak field approximation the motion of the string in the X -direction is not altered, i.e., $X = X_0 + \tau \sinh \beta$. Thus $\tau|_{X=0} = -X_0 / \sinh \beta$.

$$B_{\pm} = \cosh \beta \sqrt{\tilde{\tau}^2 \sinh^2 \beta + b^2 + \sigma^2} + \tilde{\tau} \sinh^2 \beta \pm \sigma. \quad (5.3.11)$$

The divergent term $2M \ln(\tau \cosh^2 \beta)$ in the expression for T arises because the gravitational field at infinity does not go to zero rapidly enough.

It is easy to check that Z is an antisymmetric function of σ , so that for example $Z_{,\sigma\sigma}|_{\sigma=0} = 0$. To obtain the condition of the coil formation one needs first to calculate the derivatives $Z_{,\sigma}$ and $Z_{,\sigma\tilde{\tau}}$, and then solve the equations

$$Z_{,\sigma}|_{\sigma=0} = 0, \quad (5.3.12)$$

$$Z_{,\sigma\tilde{\tau}}|_{\sigma=0} = 0, \quad (5.3.13)$$

in order to determine τ_* and b as functions of rapidity β . By calculating the derivatives we obtain

$$Z_{,\sigma}|_{\sigma=0} = 1 - 2M \cosh \beta \left(\frac{1}{\rho \cosh \beta + \tilde{\tau} \sinh^2 \beta} + \frac{2\tilde{\tau} \sinh^2 \beta}{\tilde{\tau}^2 \sinh^2 \beta + b^2 \cosh^2 \beta} \right), \quad (5.3.14)$$

$$Z_{,\sigma\tilde{\tau}}|_{\sigma=0} = 2M \cosh \beta \sinh^2 \beta \left(\frac{\tilde{\tau} \cosh \beta + \rho}{(\rho \cosh \beta + \tilde{\tau} \sinh^2 \beta)^2 \rho} - \frac{2(b^2 \cosh^2 \beta - \tilde{\tau}^2 \sinh^2 \beta)}{(\tilde{\tau}^2 \sinh^2 \beta + b^2 \cosh^2 \beta)^2} \right), \quad (5.3.15)$$

where

$$\rho = \sqrt{\tilde{\tau}^2 \sinh^2 \beta + b^2}. \quad (5.3.16)$$

We use MAPLE to make all the above computations and to solve equations (5.3.12)–(5.3.13). The solution is

$$b = 2M \cosh \beta, \quad \tau_* = 2M \cosh \beta. \quad (5.3.17)$$

The relation $b = 2M \cosh \beta$ determines a coil formation curve. This result coincides with the one obtained earlier in [21] as a condition for coil formation for the ultrarelativistic ($\beta \rightarrow \infty$) motion of the string.

For comparison, we show the coil formation curves for a non-rotating black hole in figure 5.11 (a) as calculated by using the weak field approximation. The corresponding curve lies below the exact one. One can conclude that the strong field effects help the coil formation process.

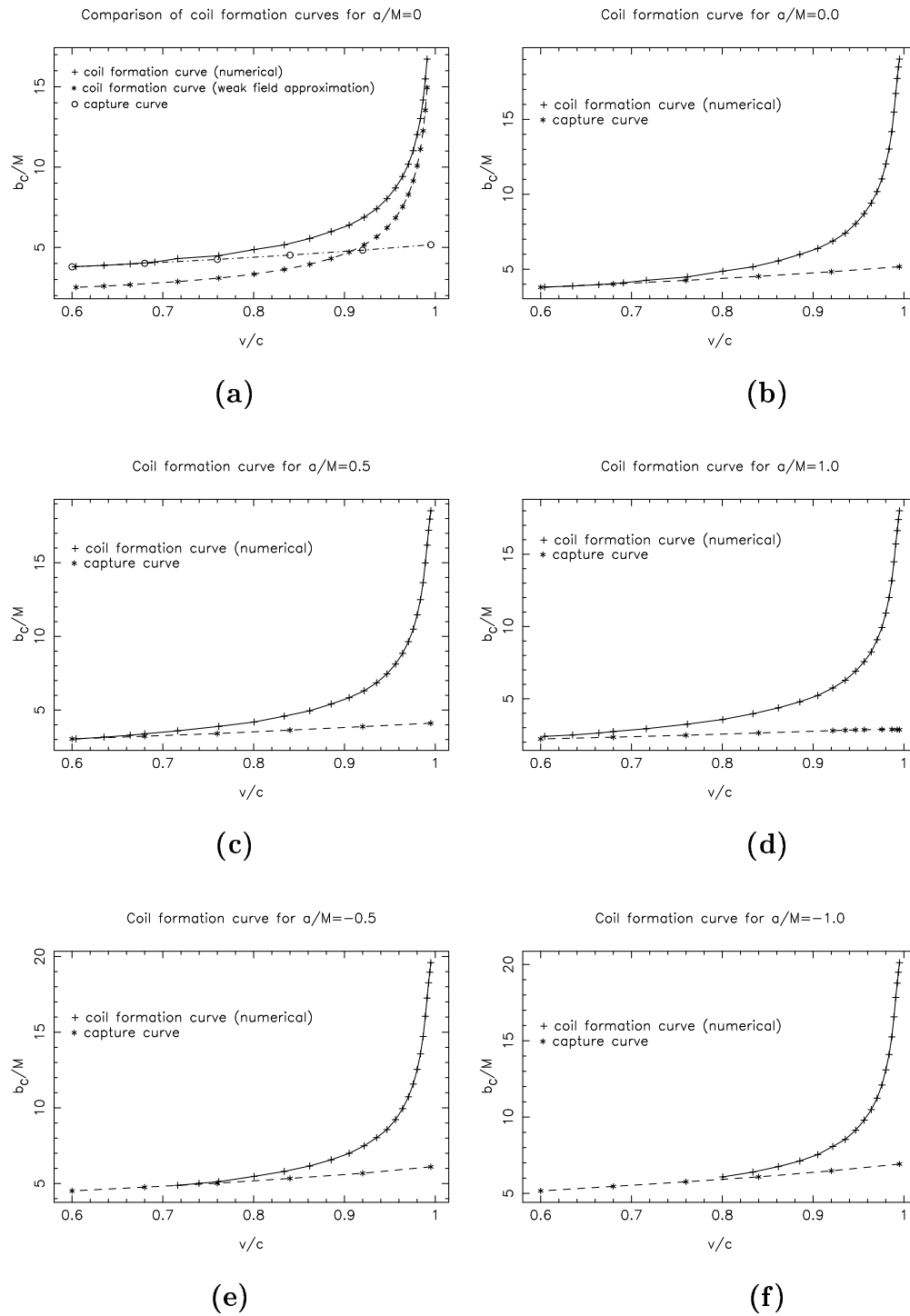


Figure 5.11: Coil formation regions for prograde and retrograde scattering of the string.

Chapter 6

Interaction of a Brane with a Moving Bulk Black Hole

String scattering and capture by black holes is a special case of a general problem of motion of different topological defects and branes in the gravitational field of a black hole. Recently, there was a great deal of discussion about brane world models with large extra spatial dimensions.

Mini black holes propagating in the bulk space and interacting with the brane representing our universe can play the role of probes testing extra dimensions. For this reason it is interesting to discuss various aspects of the black-hole-brane system. The methods developed in previous chapters can be adopted to this problem.

Black holes in the bulk space may exist as a result of the early stage evolution of the universe, e.g., as a result of the recoil during the quantum evaporation of primordial black holes created on the brane [39, 40]. The final state of such evaporating mini black holes is not known. Similarly to the early studied case of evaporation of the mini black holes in the four-dimensional theory with the Planck scale quantum gravity, two different final states are possible. Either a

stable remnant of mass of the order of M_* (see below) is formed or the evaporation is complete. We assume that bulk black holes are either those stable remnants or black hole with mass $M \gg M_*$, so that they are relatively long living.

The first section of chapter 6 explains the motivation for introducing extra dimensions into the physical picture of our world. To make the consideration more concrete we use the so called ADD model [41] (see next section for explanation) in which the gravitational field of the brane is neglected and extra dimensions are flat. An important generic feature of this model is that the fundamental quantum gravity mass scale M_* may be very low (of order TeV) and the size of the extra spatial dimensions may be much larger than the Planck length ($\sim 10^{-33}\text{cm}$).

In the most interesting version of the ADD model there exist two extra spatial dimensions with the size L of the order of 0.1 mm, which is still allowed by the experiments testing the Newton law at small distances. The gravitational radius R_0 of a black hole of mass M in the spacetime with k extra dimensions is defined by the relation $G^{(4+k)} M \sim R_0^{k+1}$, where $G^{(4+k)} = 1/M_*^{(k+2)}$ is the $(4+k)$ -dimensional Newton coupling constant. The minimal mass of the black hole is determined by the condition that its gravitational radius coincides with its Compton length $\sim 1/M$. The mass of such an elementary black hole is M_* . For $M_* \sim \text{TeV}$ one has $R_* \sim 10^{-17}\text{cm}$. When $M \gg M_*$ the higher-dimensional mini black holes can be described by the classical solutions of vacuum Einstein's equations. We assume that the size of a black hole R_0 is much smaller than the characteristic size of extra dimensions, L , and neglect the effects of the black hole deformation connected with this size.

In sections 6.2–6.5 we develop an unified approach to the weak field approximation for a generic n -brane moving in a background of an $(n+k+1)$ -dimensional Schwarzschild black hole. We investigate in more detail the case of $n = 3$ and

$k = 2$ which corresponds to the most interesting ADD model. Note that the case $n = 1$ and $k = 2$ corresponds to a string moving in the background of a standard Schwarzschild black hole. In the remainder of the chapter we discuss the effects of the presence of the bulk black hole on the physics of the three-brane.

In what follows we will interchangeably use the picture of a brane moving in a fixed background spacetime as well as the notion of a moving black hole passing an initially stationary brane.

6.1 Brane Worlds and Large Extra Dimensions

In the present particle physics paradigm there exist two different fundamental energy scales — the electroweak energy scale $m_{\text{EW}} \sim 10^3$ GeV and the Planck energy scale $M_{\text{Pl}} = 1/\sqrt{G_{\text{N}}} \sim 10^{18}$ GeV. It is generally believed that at the Planck energy all the interactions will be unified. One of the challenges is to explain the huge gap between these two energy scales. This is known as the *hierarchy problem*.

The existence of the electroweak energy scale is well established and experimentally verified up to the distances $\sim m_{\text{EW}}^{-1}$. The existence of the Planck scale, on the other hand, is taken much more on faith. The validity of the Newton's law has been to date verified only up to distances ~ 0.1 mm.

In 1998 Arkani-Hamed, Dimopoulos and Dvali [41] proposed a scenario in which the fundamental energy scale M_* is much smaller than the Planckian one and it is of order of TeV. This scenario requires the existence of large extra spatial dimensions of size R such that

$$R \leq 0.1 \text{ mm} . \tag{6.1.1}$$

Another assumption of the ADD approach is that all the Standard Model (SM) particles and fields are confined to a three-dimensional *brane* representing our

universe. Only gravity can freely propagate into the extra dimensions. The characteristic thickness of the brane d in the extra dimensions must not exceed m_{EW}^{-1} .

For $r \ll R$ the gravitational potential has the $(n + 4)$ -dimensional form

$$V(r) \sim \frac{1}{M_*^{n+2}} \frac{m_1 m_2}{r^{n+1}}, \quad (r \ll R). \quad (6.1.2)$$

When the masses are far apart ($r \gg R$) the gravitational flux lines do not have the space to spread into the extra dimensions and the potential has the standard $1/r$ dependence

$$V(r) \sim \frac{1}{M_*^{n+2} R^n} \frac{m_1 m_2}{r}, \quad (r \gg R) \quad (6.1.3)$$

and thus

$$M_{\text{Pl}}^2 = M_*^{n+2} R^n. \quad (6.1.4)$$

From the requirement $M_* \sim \text{TeV}$ we obtain the condition for the size of the extra dimension

$$R \sim 10^{\frac{30}{n}-17} \text{ cm}. \quad (6.1.5)$$

For $n = 1$ R is comparable to the size of our solar system, so it is excluded by testing the Newton's law. For $n = 2$ the size is just at the 1 mm scale so it is not excluded by experiments. For greater n the size is smaller than the present experimental bound.

One of the appeals of the ADD proposal is that it can, in principle, be tested in the near future. This is because the fundamental quantum gravity scale is about 1 TeV and that will be accessible by the Large Hadron Collider (LHC).

If the energy of the collision $E_{\text{esc}} \gtrsim m_{\text{EW}}$, created gravitons can escape into the extra dimensions which would violate the energy and momentum conservation on the brane. Note, however, that charge will still be conserved. The reason why charged particles can not escape to the bulk is that photons are localized on the brane and therefore the notion of charge has no meaning in the bulk.

Another type of experiment that could support the existence of extra dimensions is a direct measurement of deviations from Newton's law (see, e.g., [42] for a review). More dramatic effects are connected with the possibility of mini black hole creation in the colliders and cosmic rays (see, e.g., [43] for a review). Indeed, some estimates predict a production of one black hole per second in the LHC [44, 45]. Black holes, being gravitational solitons, can leave the brane (e.g., as a result of a recoil effect due to their Hawking evaporation [39, 40]) and propagate in the bulk space. Their motion is modified by the interaction with the brane. Black holes can also induce gravitational effects on the brane. In this chapter we study some of these effects.

6.2 Higher-dimensional Non-rotating Black Holes

The metric of a static multi-dimensional black hole in $(K+1)$ -dimensional space-time is

$$dS^2 = -F dT^2 + \frac{dR^2}{F} + R^2 d\Omega_{K-1}^2, \quad F = 1 - \left(\frac{R_0}{R}\right)^{K-2}, \quad (6.2.6)$$

where K is the number of spatial dimensions, R_0 is the gravitational radius and $d\Omega_{K-1}^2$ is the line element on a unit $(K-1)$ -dimensional sphere. For $K=3$ this is the usual four-dimensional Schwarzschild metric. We shall use the metric (6.2.6) in the *isotropic coordinates*

$$dS^2 = -F dT^2 + A^2 [d\sigma^2 + \sigma^2 d\Omega_{K-1}^2], \quad (6.2.7)$$

where

$$\ln \sigma = \int \frac{dR}{R\sqrt{F(R)}}, \quad A = \frac{R}{\sigma}. \quad (6.2.8)$$

In the weak field approximation when $R_0/R \ll 1$ one gets

$$R \sim \sigma + \frac{R_0^{K-2}}{2(K-2)\sigma^{K-3}}, \quad A \sim 1 + \frac{R_0^{K-2}}{2(K-2)\sigma^{K-2}}, \quad (6.2.9)$$

and the metric takes the following asymptotic form

$$dS^2 = g_{AB} dX^A dX^B, \quad (6.2.10)$$

$$g_{AB} = (1 + \Psi)\eta_{AB} + (K-1)\Psi \delta_A^0 \delta_B^0 = \eta_{AB} + \Psi h_{AB}, \quad (6.2.11)$$

where

$$h_{AB} = \eta_{AB} + (K-1) \delta_A^0 \delta_B^0, \quad \Psi = \frac{R_0^{K-2}}{(K-2)\sigma^{K-2}}. \quad (6.2.12)$$

It should be emphasized that the metric (6.2.10)–(6.2.12) describes gravitational field of any compact static distribution of matter ¹ since we are considering only the leading terms. It is a perturbation over the background flat metric

$$dS_0^2 = -dT^2 + dL_K^2, \quad (6.2.13)$$

where

$$dL_K^2 = (dX^i)^2 + (dY^m)^2 = d\sigma^2 + \sigma^2 d\Omega_{K-1}^2, \quad (6.2.14)$$

$$\sigma^2 = (X^i)^2 + (Y^m)^2. \quad (6.2.15)$$

We denote by X^i , $i = 1, \dots, n$ the ‘standard’ n Cartesian coordinates, and by Y^m , $m = n+1, \dots, n+k = K$ the Cartesian coordinates in ‘extra-dimensions’. This splitting will be meaningful and convenient later when we consider an n -dimensional brane in the spacetime of the $(K+1)$ -dimensional black hole.

¹See for example non-topological solitons in brane world models in [46].

6.3 A Moving Flat Brane in a Spacetime with a Fixed Point

Our goal is to study the equations of motion of a brane in the gravitational field of a black hole. We keep the number of brane spatial dimensions, n , and the number of extra dimensions, k , arbitrary.

In the lowest order, when the gravitational field of the black hole is neglected, $g_{AB} = \eta_{AB}$, where η_{AB} is the $(n + k + 1)$ -dimensional Minkowski metric. We also assume that the brane is flat. It is convenient to introduce an orthonormal ennuple, $N_{\hat{B}}^A$,

$$g_{AB} N_{\hat{C}}^A N_{\hat{D}}^B = \eta_{\hat{C}\hat{D}} \tag{6.3.16}$$

so that its first $n + 1$ vectors, $N_{\hat{\mu}}^A$ ($\mu = 0, \dots, n$), are tangent to the brane, while the other k vectors, $N_{\hat{m}}^A$ ($m = n + 1, \dots, n + k$), are orthogonal to the brane. worldline Γ representing a position of uniformly moving black hole is described by the equation

$$X_{\Gamma}^A = (x_0^{\hat{B}} + U^{\hat{B}} T) N_{\hat{B}}^A. \tag{6.3.17}$$

Here T is the proper time parameter along the world line, U^A is the $(n + k + 1)$ -velocity, $\eta_{\hat{A}\hat{B}} U^{\hat{A}} U^{\hat{B}} = -1$, and $X_0^A \equiv x_0^{\hat{B}} N_{\hat{B}}^A$ are the coordinates of the black hole position at $T = 0$.

Consider first the case of one extra dimension. There are two possibilities.

(1) The black hole crosses the brane. In this case we use the ambiguity $T \rightarrow T + \text{const}$ to put $T = 0$ at the moment when the black hole meets the brane. Using the Poincare group $P(n + 1)$ of coordinate transformations preserving the position of the brane in the bulk space one can always put

$$x_0^{\hat{B}} = 0, \quad U^{\hat{B}} = \cosh \beta \delta_0^{\hat{B}} + \sinh \beta \delta_{n+1}^{\hat{B}}. \tag{6.3.18}$$

That is a projection of the point representing the black hole onto the brane surface is located at the origin of the brane coordinates, at $x^{\hat{1}} = \dots = x^{\hat{n}} = 0$.

The black hole crosses the brane at the moment $x^{\hat{0}} = 0$ of the brane time, and is moving orthogonally to the brane surface. β is a rapidity parameter related to the velocity v as $v = \tanh \beta$.

(2) The black hole never crosses the brane. This is a special case when the velocity of the black hole relative to the brane vanishes. In this case by using transformations from $P(n+1)$ one can put

$$x_0^{\hat{\mu}} = 0, \quad x_0^{n+1} = b, \quad U^{\hat{B}} = \delta_0^{\hat{B}}, \quad (6.3.19)$$

where b is the distance between the black hole and the brane.

Similarly, in the case with two or more extra dimensions two cases are possible.

(1) The black hole crosses the brane. We choose T so this happens at the moment $T = 0$. It means that $x_0^{\hat{m}} = 0$. Using the Poincare group $P(n+1)$ of coordinate transformations preserving the position of the brane in the bulk space we put $x^{\hat{\mu}} = 0$ and $U^{\hat{\mu}} = \cosh \beta \delta_0^{\hat{B}}$. We use the group of rotations $O(k)$ which preserve the position of the brane to put $U^{\hat{B}} = \sinh \beta \delta_{n+1}^{\hat{B}}$. Thus we have

$$x_0^{\hat{B}} = 0, \quad U^{\hat{B}} = \cosh \beta \delta_0^{\hat{B}} + \sinh \beta \delta_{n+1}^{\hat{B}}. \quad (6.3.20)$$

(2) The black hole never crosses the brane. There exists a minimal distance, b , between the black hole and the brane, which we call the *impact parameter*. As earlier we can put $x_0^{\hat{\mu}} = 0$. We also can choose the N_{n+2}^A to be directed from the brane to the position of the black hole when it is at the minimal distance from the brane. There still exists a group $O(k-1)$ of rotations which preserves the position of the brane and the direction of N_{n+2}^A . We use this freedom to choose the vector N_{n+1}^A to coincide with the direction of the black hole velocity. For this choice we have

$$x_0^{\hat{B}} = b \delta_{n+2}^{\hat{B}}, \quad U^{\hat{B}} = \cosh \beta \delta_0^{\hat{B}} + \sinh \beta \delta_{n+1}^{\hat{B}}. \quad (6.3.21)$$

It is easy to see that the expression (6.3.21) is in fact the most general one. The relations (6.3.18)–(6.3.20) for the other cases can be obtained from (6.3.21) by either taking the limit $\beta = 0$ or putting $b = 0$.

The gravitational potential Ψ entering the expression (6.2.11) for the gravitational field of the black hole depends on the interval σ between the position of the black hole and a point in a spacetime, calculated along the surface of constant coordinate time T_c . Let us calculate σ for a point on the brane. Denote by $V^{\hat{B}}$ a vector

$$V^{\hat{B}} = \sinh \beta \delta_0^{\hat{B}} + \cosh \beta \delta_{n+1}^{\hat{B}}. \quad (6.3.22)$$

This vector is orthogonal to $U^{\hat{B}}$ and hence it is tangent to $T_c = \text{const}$ plane. The brane time $x^{\hat{0}}$ corresponding to a given T can be found from the equations

$$T U^{\hat{B}} + \lambda V^{\hat{B}} = x^{\hat{0}} \delta_0^{\hat{B}}. \quad (6.3.23)$$

This equation for $\hat{B} = n + 1$ gives

$$\lambda = -\tanh \beta T, \quad (6.3.24)$$

while for $\hat{B} = \hat{0}$ it gives

$$T = \cosh \beta x^{\hat{0}}, \quad \lambda = -\sinh \beta x^{\hat{0}}. \quad (6.3.25)$$

Using this results we easily find that

$$\sigma^2 = \rho^2 + b^2 + \sinh^2 \beta (x^{\hat{0}})^2, \quad (6.3.26)$$

where $\rho^2 = x^{\hat{i}} x_{\hat{i}}$. From this expression for σ it follows that the induced metric on the brane will be ‘spherically symmetric’, that is, it possesses the group $O(n)$ of symmetry.

Let X^A be Cartesian coordinates in the reference frame where the black hole is at rest. Then the components of the ennuple N_B^A in this frame are

$$N_0^A = \cosh \beta \delta_0^A + \sinh \beta \delta_{n+1}^A, \quad N_i^A = \delta_i^A, \quad (6.3.27)$$

$$N_{n+1}^A = \sinh \beta \delta_0^A + \cosh \beta \delta_{n+1}^A, \quad N_{\hat{m}}^A = \delta_m^A, \quad m > n + 1. \quad (6.3.28)$$

In the reference frame of the black hole the brane equation is

$$\mathcal{X}_0^A = x^{\hat{\mu}} N_{\hat{\mu}}^A + b N_{n+2}^A. \quad (6.3.29)$$

6.4 Brane Perturbation Equations of Motion. Gauge Fixing

Consider a brane $\mathcal{X}^A(x^{\hat{\mu}})$ moving in the spacetime with a metric $g_{AB}(X^C)$. The induced metric on the brane (which we assume can be described by the Nambu-Goto action) is

$$\gamma_{\hat{\mu}\hat{\nu}} = g_{AB}(\mathcal{X}^C) \mathcal{X}_{,\hat{\mu}}^A \mathcal{X}_{,\hat{\nu}}^B. \quad (6.4.30)$$

The brane equation of motion is

$$\left(\sqrt{-\gamma} \gamma^{\hat{\mu}\hat{\nu}} \mathcal{X}_{,\hat{\nu}}^A \right)_{,\hat{\mu}} + \sqrt{-\gamma} \gamma^{\hat{\mu}\hat{\nu}} \Gamma^A_{BC} \mathcal{X}_{,\hat{\mu}}^B \mathcal{X}_{,\hat{\nu}}^C = 0. \quad (6.4.31)$$

When the brane is far from the black hole g_{AB} has the form (6.2.10)–(6.2.12).

In the absence of gravity the unperturbed brane is described by the equation (6.3.29). We write the solution for a perturbed brane in the form

$$\mathcal{X}^A = \mathcal{X}_0^A + \chi^{\hat{m}}(x) N_{\hat{m}}^A + \zeta^{\hat{\mu}}(x) N_{\hat{\mu}}^A. \quad (6.4.32)$$

Let us show first that by changing the coordinates on the brane one can put $\zeta^{\hat{\mu}} = 0$. Indeed, a change of Cartesian coordinates on the brane $x^{\hat{\mu}} \rightarrow x^{\hat{\mu}} + \xi^{\hat{\mu}}(x)$ generates in (6.4.32) an extra term $\xi^{\hat{\mu}}(x) N_{\hat{\mu}}^A$. That is why, by using the diffeoinvariance of the brane equations and choosing $\xi^{\hat{\mu}} = -\zeta^{\hat{\mu}}$ one can always take²

$$\mathcal{X}^A = \mathcal{X}_0^A + \chi^{\hat{m}}(x) N_{\hat{m}}^A. \quad (6.4.33)$$

²This gauge is different from the conformal gauge we used for studying cosmic strings. As it was already mentioned the conformal gauge, which considerably simplifies many calculations, can not be adopted to higher dimensions, $n > 1$.

In this gauge $\chi^{\hat{m}}(x^{\hat{\nu}})$ are the ‘physical’ degrees of freedom of the brane. In a general case they describe both types of the brane perturbations, free waves and brane deformations induced by an external force. We focus our attention on the perturbations induced by the brane motion in the weak gravitational field. We restrict ourselves by considering only first order effects.

Using the relation

$$\mathcal{X}_{,\hat{\mu}}^A = N_{\hat{\mu}}^A + \chi_{,\hat{\mu}}^{\hat{m}} N_{\hat{m}}^A, \quad (6.4.34)$$

and keeping only the first order terms we obtain

$$\gamma_{\hat{\mu}\hat{\nu}} = \eta_{\hat{\mu}\hat{\nu}} + \Psi h_{\hat{\mu}\hat{\nu}}, \quad h_{\hat{\mu}\hat{\nu}} = h_{AB} N_{\hat{\mu}}^A N_{\hat{\nu}}^B = \eta_{\hat{\mu}\hat{\nu}} + (K-1) \cosh^2 \beta \delta_{\hat{\mu}}^0 \delta_{\hat{\nu}}^0. \quad (6.4.35)$$

We also have

$$\sqrt{-\gamma} = 1 + \frac{1}{2} [n+1 - (K-1) \cosh^2 \beta] \Psi, \quad (6.4.36)$$

$$\gamma^{\hat{\mu}\hat{\nu}} = \eta^{\hat{\mu}\hat{\nu}} - \Psi h^{\hat{\mu}\hat{\nu}}, \quad h^{\hat{\mu}\hat{\nu}} = \eta^{\hat{\mu}\hat{\alpha}} \eta^{\hat{\nu}\hat{\beta}} h_{\hat{\alpha}\hat{\beta}}. \quad (6.4.37)$$

In the chosen coordinate system, the Christoffel symbols Γ^A_{BC} are first order quantities

$$\Gamma^A_{BC} = \eta^{AD} \Gamma_{DBC}, \quad \Gamma_{DBC} = \frac{1}{2} (\Psi_{,B} h_{CD} + \Psi_{,C} h_{BD} - \Psi_{,D} h_{BC}). \quad (6.4.38)$$

By multiplying (6.4.31) by $N_{\hat{m}A}$ we obtain the following equations

$$\square^{(n+1)} \chi_{\hat{m}} = f_{\hat{m}}, \quad (6.4.39)$$

$$f_{\hat{m}} = \frac{1}{2} \Psi_{,\hat{m}} h + \frac{1}{2} (K-1) \sinh(2\beta) \Psi_{,\hat{0}} \delta_{\hat{m}}^{n+1}, \quad h = \eta^{\hat{\mu}\hat{\nu}} h_{\hat{\mu}\hat{\nu}} = n+1 - (K-1) \cosh^2 \beta. \quad (6.4.40)$$

Here $\Psi_{,\hat{\mu}} = N_{\hat{\mu}}^A \Psi_{,A}$, $\Psi_{,\hat{m}} = N_{\hat{m}}^A \Psi_{,A}$, and the $(n+1)$ -dimensional flat ‘box’-operator is defined as

$$\square^{(n+1)} = \eta^{\hat{\mu}\hat{\nu}} \partial_{\hat{\mu}} \partial_{\hat{\nu}}. \quad (6.4.41)$$

It is easy to check that the other equations obtained by multiplication of (6.4.31) by $N_{\hat{\mu}A}$ are trivially satisfied.

To calculate $f_{\hat{m}}$ we note that the function Ψ which enters this expression depends on σ^2 , i.e. $\Psi(\sigma^2)$, so that

$$\Psi_{,\hat{0}} = \Psi' \sigma_{,\hat{0}}^2, \quad \Psi_{,\hat{m}} = \Psi' \sigma_{,\hat{m}}^2, \quad (6.4.42)$$

where

$$\Psi' = \frac{\partial \Psi}{\partial \sigma^2} = -\frac{R_0^{K-2}}{2\sigma^K}, \quad (6.4.43)$$

$$\sigma^2 = \rho^2 + \sinh^2 \beta t^2 + b^2. \quad (6.4.44)$$

We denoted $t = x^{\hat{0}}$, $\rho^2 = x^{\hat{i}}x_{\hat{i}}$. We also have

$$\sigma_{,\hat{0}}^2 = 2t \sinh^2 \beta, \quad \sigma_{,\hat{n}+1}^2 = 2t \sinh \beta \cosh \beta, \quad \sigma_{,\hat{n}+2}^2 = 2b. \quad (6.4.45)$$

The other terms $\sigma_{,\hat{n}+p}^2$ with $p > 2$ vanish.

The induced metric on the unperturbed brane in the spherical coordinates is

$$ds_0^2 = \eta_{\hat{\mu}\hat{\nu}} dx^{\hat{\mu}} dx^{\hat{\nu}} = -dt^2 + d\rho^2 + \rho^2 d\Omega_{n-2}^2. \quad (6.4.46)$$

Because of the symmetry of the problem, the ‘force’ terms $f_{\hat{m}}$ on the right hand side of (6.4.39) are functions of t and ρ . Thus the induced perturbations of the brane are ‘spherically symmetric’ and can be written in the form

$$\chi_{\hat{m}} = \frac{P_m(t, \rho)}{\rho^{(n-1)/2}}. \quad (6.4.47)$$

By substituting this expression into (6.4.39) one obtains

$$\left[-\partial_t^2 + \partial_\rho^2 - \frac{(n-1)(n-3)}{4\rho^2} \right] P_m(t, \rho) = F_m(t, \rho), \quad (6.4.48)$$

where

$$f_{\hat{m}} = \frac{F_m(t, \rho)}{\rho^{(n-1)/2}}. \quad (6.4.49)$$

From this equation we see that that the cases of a string ($n = 1$) and a three-brane ($n = 3$) are particularly easy to study. Solutions for the general case are discussed in the appendix B.

6.5 Solutions of the Brane Perturbation Equations

6.5.1 Generators of solutions

In the chosen coordinate system and imposed gauge, the ‘force’ $f_{\hat{m}}$ which enters the right hand side of (6.4.39) has only two non-vanishing components, $f_- = f_{n\hat{+}1}$ and $f_+ = f_{n\hat{+}2}$. Since we consider only solutions which are induced by the ‘force’ acting on the brane, we shall also have only two non-trivial functions, $\chi_- = \chi_{n\hat{+}1}$ and $\chi_+ = \chi_{n\hat{+}2}$ which describe the brane excitations. We write the equations (6.4.39) as

$$\square^{(n+1)} \chi_{\pm}^{(n,k)} = f_{\pm}^{(n,k)} . \quad (6.5.50)$$

We included an upper index (n, k) to make clear the dependence of the functions on the number of spatial dimensions, n , of the brane, and on the number of extra dimensions, k . Simple calculations give

$$f_{\pm}^{(n,k)} = A_{\pm}^{(n,k)} \tilde{f}_{\pm}^{(n,k)} , \quad (6.5.51)$$

where

$$\tilde{f}_{-}^{(n,k)} = \frac{t}{\sigma^{n+k}} , \quad \tilde{f}_{+}^{(n,k)} = \frac{1}{\sigma^{n+k}} , \quad (6.5.52)$$

$$A_{-}^{(n,k)} = -\frac{1}{4} R_0^{n+k-2} [2 - k + (n + k - 1) \sinh^2 \beta] \sinh(2\beta) , \quad (6.5.53)$$

$$A_{+}^{(n,k)} = -\frac{1}{2} R_0^{n+k-2} [n + 1 - (n + k - 1) \cosh^2 \beta] b . \quad (6.5.54)$$

If we write

$$\chi_{\pm}^{(n,k)} = A_{\pm}^{(n,k)} \tilde{\chi}_{\pm}^{(n,k)} , \quad (6.5.55)$$

then

$$\square^{(n+1)} \tilde{\chi}_{\pm}^{(n,k)} = \tilde{f}_{\pm}^{(n,k)} . \quad (6.5.56)$$

Let us note now that

$$\tilde{f}_{\pm}^{(n,k+2)} = -\frac{2}{n+k} \frac{\partial}{\partial(b^2)} \tilde{f}_{\pm}^{(n,k)}, \quad (6.5.57)$$

and therefore

$$\tilde{\chi}_{\pm}^{(n,k+2)} = -\frac{2}{n+k} \frac{\partial}{\partial(b^2)} \tilde{\chi}_{\pm}^{(n,k)}. \quad (6.5.58)$$

This relation shows that one can generate solutions for an arbitrary $k > 2$ if the solutions for $k = 1, 2$ are known. It should be noted that for $k = 1$ there is only one transverse excitation of the brane, so that a solution $\chi_+^{(n,1)}$ does not have a direct physical meaning. Only its derivatives corresponding to higher values of k are physical. We call the functions $\chi_{\pm}^{(n,1)}$ and $\chi_{\pm}^{(n,2)}$ *generating solutions*.

6.5.2 Generating solutions for $n = 3$ brane

As an important example we consider now a special case when the brane has three spatial dimensions. This case is interesting for brane world models. The generating solutions for this case can be written as follows (see appendix B)

$$\tilde{\chi}_{\pm}^{(k)} = \frac{-1}{2\rho} \int_{-\infty}^t dt' \int_0^{\infty} d\rho' \rho' \tilde{f}_{\pm}^{(k)} (\vartheta(\lambda_+) - \vartheta(\lambda_-)), \quad (6.5.59)$$

where

$$\lambda_{\pm} = (t - t')^2 - (\rho \mp \rho')^2. \quad (6.5.60)$$

In order to make notations more compact we omitted index $n = 3$ in the superscript.

Since the $\tilde{f}_{\pm}^{(k)}$ are even functions of ρ the integral over the two ‘mirror’ regions can be rewritten as an integral over one region characterized only by the $\vartheta(\lambda_+)$ without the restriction of ρ being greater than zero (see figure 6.1).

After calculating the integrals we obtain

$$\tilde{\chi}_{-}^{(1)} = \frac{1}{\cosh^2 \beta} \left[(t + \rho) S_+^{(1)} - (t - \rho) S_-^{(1)} \right], \quad (6.5.61)$$

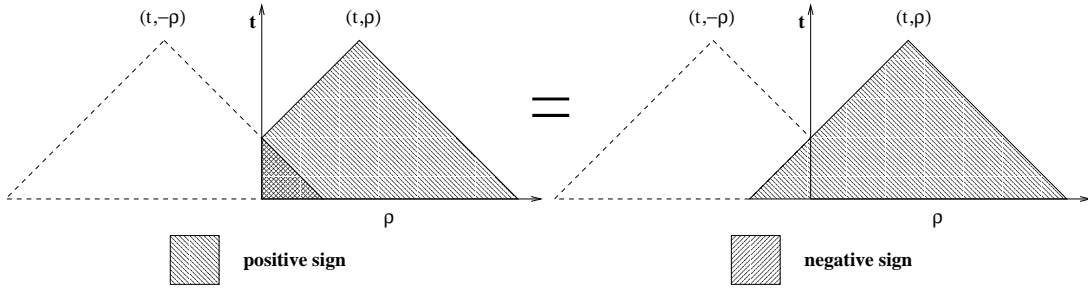


Figure 6.1: It is equivalent to integrate over the two regions on the left as it is to integrate over the one region on the right.

$$\tilde{\chi}_+^{(1)} = S_+^{(1)} - S_-^{(1)}, \quad (6.5.62)$$

where

$$S_{\pm}^{(1)} = \frac{1}{4\rho R_{\pm}} \left[\arctan \left(\frac{t \sinh^2 \beta \mp \rho}{R_{\pm}} \right) + \frac{\pi}{2} \right], \quad (6.5.63)$$

and

$$R_{\pm}^2 = (t \pm \rho)^2 \sinh^2 \beta + b^2 \cosh^2 \beta. \quad (6.5.64)$$

We also have

$$\tilde{\chi}_-^{(2)} = \frac{1}{\cosh^2 \beta} \left[(t + \rho) S_+^{(2)} - (t - \rho) S_-^{(2)} \right], \quad (6.5.65)$$

$$\tilde{\chi}_+^{(2)} = S_+^{(2)} - S_-^{(2)}, \quad (6.5.66)$$

where

$$S_{\pm}^{(2)} = \frac{1}{6\rho R_{\pm}^2} \left(\frac{t \sinh^2 \beta \mp \rho}{\sqrt{\rho^2 + t^2 \sinh^2 \beta + b^2}} + \cosh \beta \right). \quad (6.5.67)$$

Let us illustrate the motion of the brane in the case $n = 3$, and $k = 2$. The parametric equations for the brane in isotropic coordinates are

$$X^0 = t \cosh \beta - 2R_0^3 \sinh^4 \beta \cosh \beta \tilde{\chi}_-^{(2)}, \quad (6.5.68)$$

$$X^1 = x^1, \quad X^2 = x^2, \quad X^3 = x^3, \quad (6.5.69)$$

$$X^4 = t \sinh \beta - 2R_0^3 \sinh^3 \beta \cosh^2 \beta \tilde{\chi}_-^{(2)}, \quad (6.5.70)$$

$$X^5 = b + 2b R_0^3 \sinh^2 \beta \tilde{\chi}_+^{(2)} . \quad (6.5.71)$$

Figures 6.2 and 6.3 show plots of χ_{\pm} for a particular choice of parameters. Both plots depict a disturbance of the brane developed around “time” $t = 0$ which travels at a speed of light outward from the point of the brane closest to the black hole.

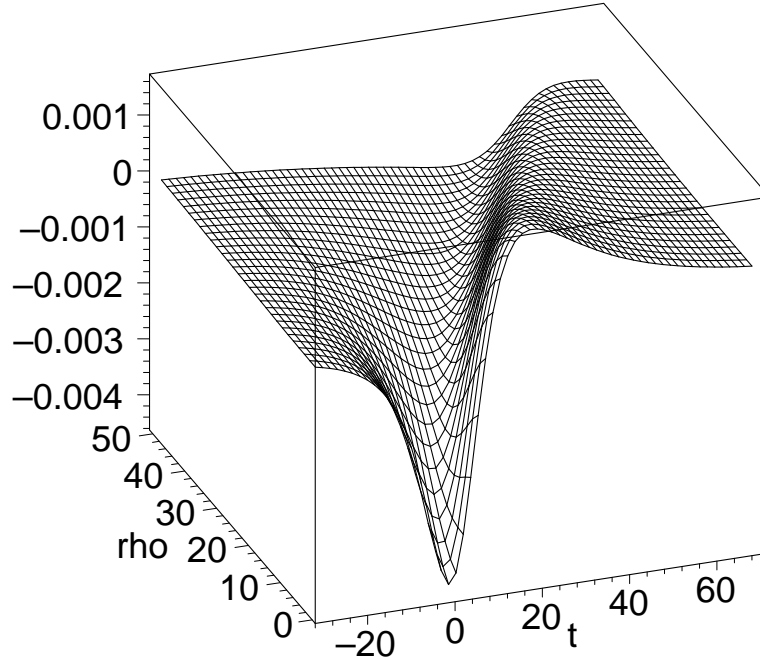


Figure 6.2: Plot of χ_- for $\beta = 1$, $R_0 = 1$, $b = 10$, $k = 2$.

6.5.3 Energy loss

As a result of the black hole action, the brane transforms from its initial state without excitations to a new excited state. The energy gained by the brane in this process is equal to the loss of the kinetic energy of the black hole. We calculate now this energy loss.

In the limit $t \rightarrow \infty$, $u = t - \rho = \text{const}$, the brane excitation amplitudes χ_{\pm}

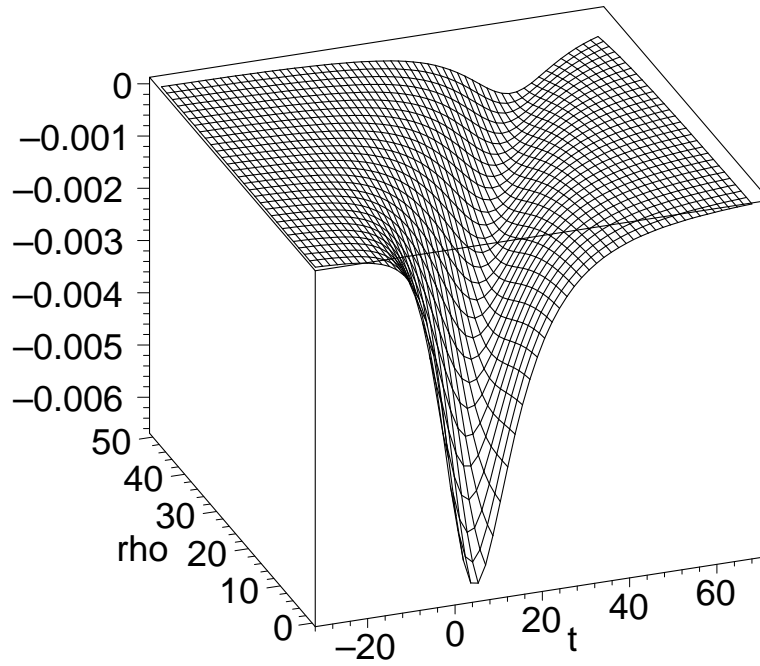


Figure 6.3: Plot of χ_+ for $\beta = 1$, $R_0 = 1$, $b = 10$, $k = 2$.

take the following form

$$\chi_{\pm} = \frac{\Phi_{\pm}(u)}{\rho}, \quad (6.5.72)$$

$$\Phi_- = \frac{2}{3} R_0^3 \sinh^3 \beta \frac{u}{u^2 \sinh^2 \beta + b^2 \cosh^2 \beta}, \quad (6.5.73)$$

$$\Phi_+ = -\frac{2}{3} R_0^3 b \cosh \beta \sinh^2 \beta \frac{1}{u^2 \sinh^2 \beta + b^2 \cosh^2 \beta}. \quad (6.5.74)$$

Figure 6.4 shows the typical shape of the functions Φ_{\pm} around $u = 0$.

In the asymptotic regime, when the gravitational field of the black hole can be neglected, the induced metric (6.4.30) is

$$\gamma_{\hat{\mu}\hat{\nu}} = \eta_{\hat{\mu}\hat{\nu}} + \chi_{,\hat{\mu}}^{\hat{m}} \chi_{\hat{m},\hat{\nu}}. \quad (6.5.75)$$

The linearized Nambu-Goto action is

$$I = \sigma \int \sqrt{-\gamma} d^n x = I_0 + I_2, \quad (6.5.76)$$

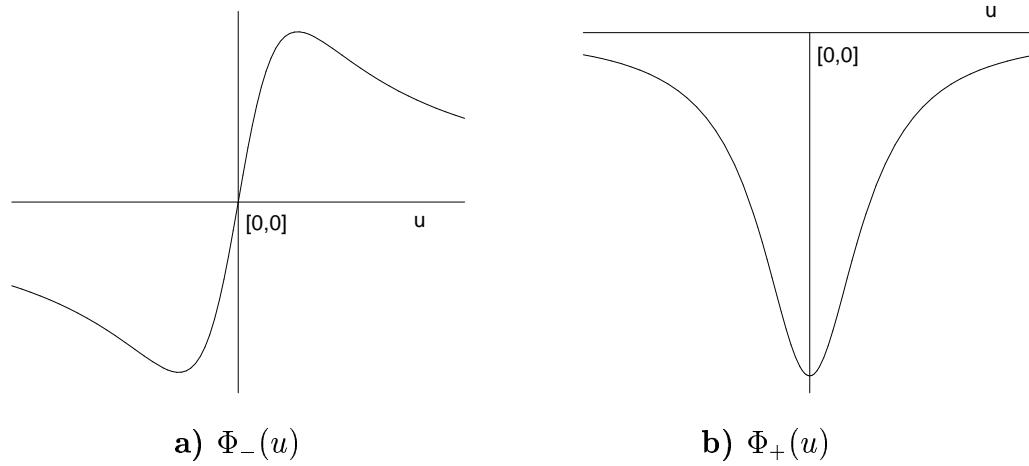


Figure 6.4: Asymptotic shape of the fields Φ_- and Φ_+ .

where σ is the tension of the brane, I_0 is a constant and

$$I_2 = -\frac{1}{2} \sigma \sum_{\hat{m}=n+1}^{n+k} \int (\nabla \chi^{\hat{m}})^2. \quad (6.5.77)$$

In our case the asymptotic excitations are described by two massless scalar fields with the Lagrangian density

$$\mathcal{L}_{\pm} = -\frac{1}{2} \sigma \partial_{\mu} \chi_{\pm} \partial^{\mu} \chi_{\pm}. \quad (6.5.78)$$

The energy flux \mathcal{E}_{\pm} calculated at the future null infinity is

$$\mathcal{E}_{\pm} = 4\pi \sigma \int_{-\infty}^{\infty} du (\Phi_{\pm,u})^2. \quad (6.5.79)$$

Simple calculations give

$$\mathcal{E}_- = \mathcal{E}_+ = \frac{4\pi^2 \sigma \sinh^5 \beta}{9 \cosh^3 \beta} \frac{R_0^6}{b^3}. \quad (6.5.80)$$

Thus the total energy lost by the black hole and gained by the brane is

$$\Delta E = \mathcal{E}_- + \mathcal{E}_+ = \frac{8\pi^2 \sigma \sinh^5 \beta}{9 \cosh^3 \beta} \frac{R_0^6}{b^3}. \quad (6.5.81)$$

Since extra dimensions are compactified, the black hole will be passing near the brane again and again. Because of the friction force connected with the energy loss, the black hole will slow down until it finally be at rest with respect to the brane.

6.6 ‘Shadow Matter’ Effect

We discuss now effects connected with the action of the black hole moving in the bulk on particles and fields localized on the brane. These effects arise because the bulk black hole modifies the metric on the brane.

The metric induced on a three-brane by a black hole moving in the $3 + k$ -dimensional bulk space is

$$ds^2 = - [1 + [1 - (k + 2) \cosh^2 \beta] \Psi] dt^2 + (1 + \Psi) [d\rho^2 + \rho^2 d\Omega_2^2] . \quad (6.6.82)$$

Particles and light on the brane are moving along geodesics in this metric. If an observer on the brane does not know about the existence of extra dimension and uses the standard four-dimensional Einstein’s equations he would arrive to the conclusion that there exists some distribution of matter on the brane responsible for this gravitational field. Since this matter is not connected with any usual four-dimensional physical fields and particles we call it a ‘shadow matter’. We discuss now the properties of this matter.

The Einstein tensor $G_{\hat{\mu}\hat{\nu}} = R_{\hat{\mu}\hat{\nu}} - 1/2\gamma_{\hat{\mu}\hat{\nu}}R$ for the metric (6.6.82) takes the form (in spherical coordinates (t, ρ, θ, ϕ))

$$G_{\hat{0}\hat{0}} = \frac{R_0^{k+1}}{\sigma^{k+5}} [3t^2 \sinh^2 \beta - \rho^2 k + 3b^2] , \quad (6.6.83)$$

$$G_{\hat{1}\hat{1}} = \frac{R_0^{k+1}}{\sigma^{k+5}} [kt^2 \sinh^2 \beta + (\rho^2 + b^2)((3 + k) \cosh^2 \beta - 3)] , \quad (6.6.84)$$

$$G_{\hat{0}\hat{1}} = -\frac{t\rho R_0^{k+1}(3 + k) \sinh^2 \beta}{\sigma^{k+5}} , \quad (6.6.85)$$

$$G_{\hat{2}\hat{2}} = \frac{G_{\hat{3}\hat{3}}}{\sin^2 \theta} = \frac{R_0^{k+1} \rho^2}{2\sigma^{k+5}} [k[2t^2 \sinh^2 \beta + \rho^2(2 - (3 + k) \cosh^2 \beta)]$$

$$+2b^2((3+k)\cosh^2\beta-3)] . \quad (6.6.86)$$

Figure 6.5 shows plots of the various non-zero components of the Einstein tensor $G_{\mu\nu}$ which is proportional to the stress-energy tensor $T_{\mu\nu}$ measured by observers living on the brane. The thick line on figure 6.5a marks the border between the positive and negative energy density.

In the simplest case when the bulk black hole is not moving ($\beta = 0$) these expressions simplify and non-vanishing components of the Einstein tensor are (at $t = 0$)

$$G_{\hat{0}\hat{0}} = \frac{R_0^{k+1}}{\sigma^{k+5}} [-\rho^2 k + 3b^2] , \quad (6.6.87)$$

$$G_{\hat{1}\hat{1}} = \frac{R_0^{k+1}}{\sigma^{k+5}} k(\rho^2 + b^2) , \quad (6.6.88)$$

$$G_{\hat{2}\hat{2}} = \frac{G_{\hat{3}\hat{3}}}{\sin^2\theta} = \frac{R_0^{k+1}\rho^2 k}{2\sigma^{3+k}} [-\rho^2(k+1) + 2b^2] . \quad (6.6.89)$$

Suppose a brane observer uses the Einstein's equations to describe the gravitational field on the brane. In this case he would come to a conclusion that there exists some form of matter for which

$$T_{\hat{\mu}\hat{\nu}} = \frac{1}{8\pi G^{(4)}} G_{\hat{\mu}\hat{\nu}} , \quad (6.6.90)$$

where $G^{(4)}$ is a 4-dimensional Newtonian coupling constant. For a static black hole this spherically symmetric distribution of matter is of the form

$$T_{\hat{\mu}}^{\hat{\nu}} = \text{diag}(-\varepsilon, p_\rho, p_{\theta\perp}, p_{\phi\perp}) . \quad (6.6.91)$$

Since the total number of spatial dimensions is greater than three, i.e. $k > 0$, the energy density ε is positive at the center and changes its sign and becomes negative at $\rho > \rho_b = b\sqrt{3/k}$. The radial pressure p_ρ is always positive, while the transverse pressures $p_{\theta\perp}$ and $p_{\phi\perp}$ being positive at the center become negative at $\rho > b\sqrt{2/(k+1)}$.

Let us estimate the total positive mass m_b of the ‘shadow matter’ inside the sphere of the radius ρ_b . To define this mass one can use the relation

$$m(r) = 4\pi \int_0^r dr r^2 T_{\hat{0}\hat{0}}. \quad (6.6.92)$$

The radius coordinate r is related to the isotropic coordinate as

$$(1 + \Psi) \rho^2 = r^2. \quad (6.6.93)$$

Since we are considering only first order terms we can write

$$m(\rho) = \frac{1}{2G^{(4)}} \int_0^\rho d\rho \rho^2 G_{\hat{0}\hat{0}} = \frac{1}{2G^{(4)}} \frac{R_0 \rho^3}{(\rho^2 + b^2)^{\frac{k+3}{2}}} \quad (6.6.94)$$

In particular, we have

$$m_b = m(\rho_b) = \alpha(k) \frac{R_0}{G^{(4)}} \left(\frac{R_0}{b} \right)^k, \quad (6.6.95)$$

where

$$\alpha(k) = \frac{3\sqrt{3}}{2} \frac{k^{k/2}}{(k+3)^{(k+3)/2}}. \quad (6.6.96)$$

It is convenient to rewrite (6.6.95) as

$$m_b = \alpha(k) m_* \left(\frac{R_0}{R_*} \right)^{k+1} \left(\frac{R_*}{b} \right)^k. \quad (6.6.97)$$

Here $R_* = 1/M_*$ is the gravitational radius of the fundamental mini black hole, and $m_* = R_*/G^{(4)}$. For $M_* \sim TeV$ one has $m_* \sim 10^{11}g$! This is 100000 tons of “shadow matter” concentrated in the region of the size TeV^{-1} . However, this feature is visible only for a test particle whose wavelength is of order TeV^{-1} .

The mass m_b is surrounded by the negative mass distribution ε . For infinite size of extra dimensions, at far distances it exactly cancels the mass m_b , so that the total mass as measured at infinity vanishes. It happens because the induced gravitational field potential decays at infinity as is required by the $(3+k)$ -dimensional Newton’s law (i.e. $\sim G^{(4+k)}M/r^{1+k}$), while the standard

3-dimensional Newtonian gravitational potential of mass M at far distance is $G^{(4)}M/r$. For a finite size L of extra dimensions this cancellation is not complete. The gravitational field of the bulk mass M as measured by the brane observer at $r \gg L$ is $\sim G^{(4+k)}M/(L^k r) = G^{(4)}M/r$. In other words, the bulk masses at $r \gg L$ contribute to the gravitational field on the brane similarly to the matter on the brane.

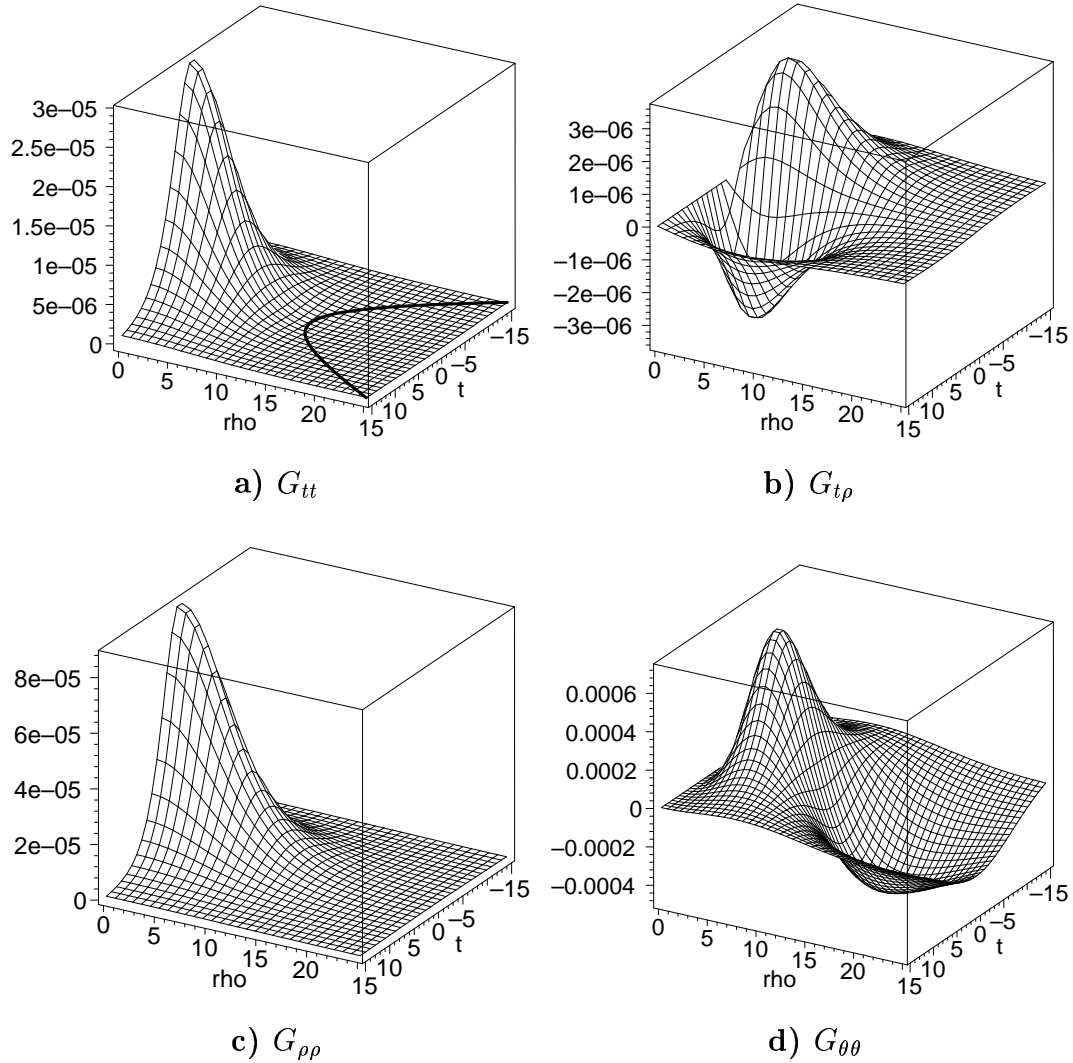


Figure 6.5: Plots of the components of the Einstein tensor of the induced geometry on the brane. The parameters are $R_0 = 1$, $\beta = 1$, $b = 10$, $k = 2$

One can easily check that for $\rho > \rho_b$ the ‘shadow matter’ distribution violates the weak energy condition ³: $\varepsilon \geq 0$ and $\varepsilon + p_i \geq 0$, ($i = 1, 2, 3$). This violation is apparent only for an observer located on the brane. The complete system (brane + bulk) does not violate any of the energy conditions. The violation of the weak energy condition in particular implies that an n -dimensional pencil of initially parallel null rays propagating on the brane and passing through the region with $\rho > \rho_b$ will be defocused, that is the n -dimensional area of its cross-section will increase. If on the other hand one consider the $(n + k)$ -dimensional pencil of initially parallel null rays propagating in the bulk, the area of its $(n + k)$ -dimensional cross-section will decrease. There is no contradiction between these two results, since the Weyl tensor of the bulk gravitational field does not vanish. As a result a shear is generated, and the expansion of the beam in the direction of the brane is compensated by the contraction of the beam in the bulk dimensions.

6.7 Deflection of Light

The ‘shadow-matter’ can affect the propagation of test particles and light on the brane. We consider now the deflection of a light ray passing in the region of influence of the ‘shadow-matter’. For simplicity we assume that the bulk black hole velocity vanishes. Again, we assume the brane to be three-dimensional.

Since the propagation of light is invariant under conformal transformation of the metric, we divide the metric (6.6.82) by $(1 + \Psi)$ and keep the leading order terms

$$d\hat{s}^2 = - [1 - (k + 2) \Psi] dt^2 + d\rho^2 + \rho^2 d\Omega_2^2, \quad (6.7.98)$$

where

$$\Psi = \frac{R_0^{k+1}}{(k + 1)[b^2 + \rho^2]^{(k+1)/2}}. \quad (6.7.99)$$

³In fact the dominant and strong energy conditions are also violated.

To simplify the notation further we rewrite (6.7.98) as

$$d\hat{s}^2 = \left[-1 + \frac{A}{[b^2 + \rho^2]^{(k+1)/2}} \right] dt^2 + d\rho^2 + \rho^2 d\Omega_2^2 \quad (6.7.100)$$

with

$$A = \frac{R_0^{k+1}(k+2)}{k+1} . \quad (6.7.101)$$

From here we follow the standard procedure. We assume motion in the equatorial plane $\theta = \pi/2$. The 4-momentum of the photon is defined as

$$p^\mu = \frac{dx^\mu}{d\lambda} , \quad (6.7.102)$$

where the affine parameter λ is defined through the equation

$$p^\rho = \frac{d\rho}{d\lambda} . \quad (6.7.103)$$

Let us define the conserved quantities

$$L = p_\phi , \quad (6.7.104)$$

$$E = -p_t . \quad (6.7.105)$$

We can now write (up to the first order in Ψ)

$$p^t = - \left(1 + \frac{A}{[b^2 + \rho^2]^{(k+1)/2}} \right) p_t = \left(1 + \frac{A}{[b^2 + \rho^2]^{(k+1)/2}} \right) E , \quad (6.7.106)$$

$$p^\phi = \frac{p_\phi}{\rho^2} = \frac{L}{\rho^2} , \quad (6.7.107)$$

$$p^\rho = \frac{d\rho}{d\lambda} , \quad (6.7.108)$$

$$p^\theta = 0 . \quad (6.7.109)$$

From the defining equation for a motion of light $p^\mu p_\mu = 0$ we get

$$\frac{d\rho}{d\lambda} = \pm L \sqrt{\left(1 + \frac{A}{[b^2 + \rho^2]^{(k+1)/2}} \right) \frac{1}{b_0^2} - \frac{1}{\rho^2}} , \quad (6.7.110)$$

where the impact parameter b_0 of the photon is defined as

$$b_0 = \frac{L}{E} . \quad (6.7.111)$$

The desired equation for $\frac{d\phi}{d\rho}$ is

$$\frac{d\phi}{d\rho} = \frac{p_\phi}{p_\rho} = \pm \frac{1}{\rho^2 \sqrt{\left(1 + \frac{A}{[b^2 + \rho^2]^{(k+1)/2}}\right) \frac{1}{b_0^2} - \frac{1}{\rho^2}}} = \pm \frac{u^2}{\sqrt{\frac{1}{b_0^2} - u^2 \left(1 - \frac{Du^{(k-1)}}{[1+b^2u^2]^{(k+1)/2}}\right)}} , \quad (6.7.112)$$

where

$$D = \frac{A}{b_0^2} \quad (6.7.113)$$

and

$$u = \frac{1}{\rho} . \quad (6.7.114)$$

Switching to the variable u

$$\frac{d\phi}{du} = \frac{\mp 1}{\sqrt{\frac{1}{b_0^2} - u^2 \left(1 - \frac{Du^{(k-1)}}{(1+b^2u^2)^{\frac{k+1}{2}}}\right)}} . \quad (6.7.115)$$

Next we perform a substitution

$$y = u \sqrt{1 - \frac{Du^{(k-1)}}{(1+b^2u^2)^{\frac{k+1}{2}}}} . \quad (6.7.116)$$

Note that this substitution makes sense only for $k \geq 1$. Then up to the first order in Ψ we obtain

$$\frac{d\phi}{dy} = \frac{\frac{d\phi}{du}}{\frac{dy}{du}} = \left(1 + \frac{Dy^{k-1}(k - y^2b^2)}{2(1+b^2y^2)^{(3+k)/2}}\right) / \left(\sqrt{\frac{1}{b_0^2} - y^2}\right) \quad (6.7.117)$$

(up to the first order $u = y$). The solution is obtained by integrating (6.7.117)

$$\Delta\phi = 2 \int_0^{\frac{1}{b_0}} \frac{d\phi}{dy} dy - \pi \quad (6.7.118)$$

After performing the integral in MAPLE and some simplification we obtain

$$\Delta\phi = b_0 D \sqrt{\pi} \frac{\Gamma(k/2)}{\Gamma((3+k)/2)} \frac{k}{4b^k} \left(H \left[\frac{k}{2}, \frac{1}{2}; -\frac{1}{2} \right] \left(-\frac{b_0^2}{b^2} \right) - \frac{b^{k+2}}{(b^2 + b_0^2)^{(k+2)/2}} \right), \quad (6.7.119)$$

where H is a generalized hypergeometric function defined as

$$H[n_1, \dots, n_p; m_1, \dots, m_q](z) = \sum_{k=0}^{\infty} \frac{\prod_{i=1}^p \frac{\Gamma(n_i+k)}{\Gamma(n_i)}}{\prod_{i=1}^q \frac{\Gamma(m_i+k)}{\Gamma(m_i)}} \frac{z^k}{k!}. \quad (6.7.120)$$

For our particular values we can write

$$H \left[\frac{k}{2}, \frac{1}{2}; -\frac{1}{2} \right] (z) = \frac{1 - (k+1)z}{(1-z)^{(k+2)/2}} \quad (6.7.121)$$

and thus (after restoring the constants) we get

$$\Delta\phi = b_0 R_0^{k+1} \sqrt{\pi} \frac{\Gamma(\frac{k}{2})}{4\Gamma(\frac{3+k}{2})} \frac{k(k+2)}{(b^2 + b_0^2)^{(k+2)/2}} = \frac{b_0 R_0^{k+1} \sqrt{\pi}}{(b^2 + b_0^2)^{(k+2)/2}} \frac{(k+2)\Gamma(1 + \frac{k}{2})}{(k+1)\Gamma(\frac{k+1}{2})}. \quad (6.7.122)$$

In particular, for the case of one and two extra dimensions one has

$$\Delta\phi^{(1)} = \frac{3}{4}\pi R_0^2 \frac{b_0}{(b^2 + b_0^2)^{3/2}}, \quad \Delta\phi^{(2)} = \frac{8}{3}R_0^3 \frac{b_0}{(b^2 + b_0^2)^2}. \quad (6.7.123)$$

For comparison, the standard (3 + 1)-dimensional case ($k = 0, b = 0$) is

$$\Delta\phi = \frac{2R_0}{b_0}. \quad (6.7.124)$$

The different functional dependence of the deflection angle on the impact parameter of light b_0 gives us opportunity to distinguish between the real matter on the brane and the bulk ‘shadow matter’ as a cause of deflection.

Chapter 7

Conclusions and Discussions

7.1 Summary of Findings

In this thesis we discussed two problems involving interaction of extended objects with black holes: we studied the dynamics of cosmic strings in Kerr spacetimes in both weak and strong field regimes and the interaction of an n -dimensional brane with a higher-dimensional Schwarzschild black hole.

First, we analyzed the problem of **scattering of a cosmic strings by a rotating black hole**. We examined a wide range of velocities and the whole spectrum of angular momenta of the black hole. We used numerical simulations to obtain the results. We found that using non-uniform grid which adapts itself to the string configuration was very beneficial and in fact necessary for running long simulations in order to obtain late time scattering data.

We demonstrated that qualitatively many general features of the weak field scattering are present in scattering of the cosmic string in the strong field regime. Displacement of the string in the Y -direction always has the form of a transition of the string from the initial phase (initial plane) to the final phase (final plane which is parallel to the initial one and displaced in the direction to the black hole

by distance κ). The boundary between these phases is a kink moving with the velocity of light away from the center. An important difference between weak and strong field scattering is in the dependence of κ on the impact parameter b and velocity v . In general, κ for strong field scattering is much greater than its value calculated by the weak field approximation. It is also always greater for retrograde scattering than for a prograde scattering. The explanation of this is quite simple. The retrograde string spends more time in the vicinity of the black hole than a prograde one. This effect is a result of the dragging of the string into rotation by the black hole.

Next we studied **capture and critical scattering of a cosmic string by a rotating black hole**. For this purpose we developed an advanced adaptive mesh refinement algorithm which automatically changes the computational grid based on the solution error estimate. These types of algorithms play an important role in other areas of computational physics, e.g., numerical relativity.

For capture and critical scattering of the string the effects connected with the rotation of the black hole are very profound. Partially, it is related to the fact that the dragging into rotation effect increases the velocity of the central part of the string (as seen by an external observer) for prograde scattering and decreases it for the retrograde scattering. Because it is easier to catch a slower moving object, the critical impact parameter b_c is greater for retrograde motion than for the prograde one. We calculated the critical impact parameter as a function of velocity of the string for black holes with different angular momenta. These plots have interesting features for v and a/M close to 1. In this regime the central part of the string can spend a considerable amount of time moving in the black hole vicinity before it gets captured or escapes. This makes such a regime of critical scattering highly complicated. Since the system is non-linear, and there are two qualitatively different final states (capture and scattering) one

can expect elements of chaotic behavior in this case. Such a chaotic behavior occurs for example in the axisymmetric case when a circular loop of a cosmic string moves in the Schwarzschild black hole metric [38].

One can also make the following observation. The internal geometry on the worldsheet of the string is described by a time dependent two-dimensional metric. When the string crosses the event horizon of the bulk black hole, a region on the string surface is formed where it is impossible to communicate with the parts of the string which are outside the bulk black hole event horizon. In other words, a two-dimensional black hole is created. The degrees of freedom living on the string surface, e.g. transverse string perturbations, propagate in this two-dimensional spacetime with a 2-D black hole in it [47, 48]. From this ‘2D point of view’ the scattering of the string with the critical impact parameter is an event at the threshold of the 2D black hole formation. One can make a conjecture that a formation of a 2D stringy hole obeys the scaling laws similar to the universal scaling laws numerically discovered by Choptuik [49] in the general theory of relativity. Similar effects for a world domain interacting with a black hole was discussed in [50, 51].

Finally, we studied **the interaction of an n -dimensional brane with a higher-dimensional Schwarzschild black hole.**

The $n = 1$ case corresponds to a cosmic string, $n = 2$ to a domain wall, while $n = 3$ can be interpreted as the observable universe in the context of brane world models. We derived the general form of the perturbation equations for an n -brane in the background of a $(n + k)$ -dimensional black hole in the weak field approximation.

For odd number of spatial brane dimensions by using convenient mathematical transformations we derived the closed form solution of the D’Alambert equation with a spherically symmetric source (see appendix B). We applied this

result to the most interesting case of a three-brane in a spacetime with extra dimensions where we obtained a general solution.

We calculated the induced geometry on the brane generated by a moving black hole. As considered by a brane observer this geometry can be obtained by solving $(n + 1)$ -dimensional Einstein's equations with a non-vanishing right hand side. We calculated the effective stress-energy tensor corresponding to this 'shadow-matter'. We showed that there exist regions where a brane observer sees an apparent violation of energy conditions. The 'shadow-matter' also affects the propagation of test particles and light on the brane. We demonstrated this by deriving results for deflection of light propagating in the induced spacetime metric on the brane. As expected, results are quite different from the $(3 + 1)$ -dimensional results. It would be interesting to study eventual observational tests which would indicate that the 'shadow-matter' and thus the extra dimensions influence the physics of our $(3 + 1)$ -dimensional world.

One of the possible interesting application of the 'shadow matter' effect might be the following. If there exists a diluted non-relativistic gas of stable elementary mini black holes in the extra dimensions, its gravitational action on the brane would be similar to the "observable" dark matter, provided the $(3 + k)$ -dimensional density of this gas is n_k where

$$\epsilon_{DM} \sim M_* n_k L^k. \quad (7.1.1)$$

Here ϵ_{DM} is the mass density of the dark matter. For $\epsilon_{DM} \approx 10^{-29} \text{g/cm}^3$ one has

$$n_k \sim 10^{-6+2k} 1/\text{cm}^{3+k}. \quad (7.1.2)$$

Since the average distance between the bulk black holes, $n_k^{-1/(3+k)}$, is much larger than the black hole radius R_* , with a very high accuracy one can consider such gas to be very diluted and neglect the gravitational interaction between the

black holes. A distinguishing property of this model is that there are no physical particles on the brane responsible for the dark matter.

7.2 Future Research

The numerical solver we used for the simulations proved to be capable of evolving cosmic strings in variety of situations including critical scattering. However, in the present state the solver is not capable to evolve a captured string for any reasonable amount of time. The problem is that the part of the string inside the event horizon quickly plunges into the singularity and the simulation necessarily crashes. Since the part of the string inside the horizon can not affect the part of the string outside, we can, in principle, ignore the part of the string inside. This effectively introduces an artificial boundary at the horizon which must be dealt with appropriately. We have experimented a bit with some prescriptions but the results were not satisfactory. Unfortunately time constraints did not allow us to pursue this topic further.

Similar situations are encountered in numerical relativity. The methods developed to deal with them are commonly called singularity excision techniques. We believe that some of the prescriptions used there might help to find the solution to the problem.

Another possible project is to use numerical methods to simulate scattering of n -branes by the higher dimensional black holes in the strong field regime. Because of the spherical symmetry this is effectively a $(1 + 1)$ -dimensional problem. We feel that the numerical solver used for string simulation should be able to perform the simulations without major modifications.

Appendix A

Details of the Numerical Scheme

In this appendix we describe the details of the numerical scheme used in our simulations of the cosmic string scattering and capture. As already mentioned in subsection 3.2.4 we exploit the symmetry of our problem and simulate only one half of the string corresponding to the non-positive values of the Z coordinate. At each parametric time τ the string segment is parametrized by an internal coordinate $\sigma \in [-\sigma_{\max}, 0]$. In what follows we will call the part of the string around the $\sigma = 0$ (corresponding to the center of symmetry) the “center” of the string and we refer to the end of the string corresponding to $-\sigma_{\max}$ as the “leftmost” part.

A.1 Coordinate Choice

For numerical simulations we use two types of coordinates. For non-critical scattering we use the Kerr ingoing coordinates (3.1.5). These coordinates behave well everywhere but have one significant flaw near the Z -axis ($\theta = 0$). The problem is caused by the $\cot \theta$ terms present in the expressions for the Christoffel symbols. Since for non-critical scattering the string does not come too close to

the Z -axis those coordinates can be safely used. During the critical scattering or capture simulations, however, the string often crosses the Z -axis so we must use a modified coordinate system. For this purpose we “cartesianized” the coordinate system (3.1.5), i.e., we transformed the spatial coordinates $(r, \theta, \tilde{\phi})$ into $(\tilde{X}, \tilde{Y}, \tilde{Z})$ by standard formulas

$$\tilde{X} = r \sin \theta \cos \tilde{\phi}, \quad (\text{A.1.1})$$

$$\tilde{Y} = r \sin \theta \sin \tilde{\phi}, \quad (\text{A.1.2})$$

$$\tilde{Z} = r \cos \tilde{\theta}. \quad (\text{A.1.3})$$

A.2 Discretization of the Equations of Motion

The equations of motion for a cosmic string in the conformal gauge have the form (2.5.44)

$$-\frac{\partial^2 X^A}{\partial \tau^2} + \frac{\partial^2 X^A}{\partial \sigma^2} + \Gamma^A{}_{BC}(X^A) \left\{ -\frac{\partial X^B}{\partial \tau} \frac{\partial X^C}{\partial \tau} + \frac{\partial X^B}{\partial \sigma} \frac{\partial X^C}{\partial \sigma} \right\}. \quad (\text{A.2.4})$$

It is a system of four semi-linear hyperbolic differential equations of second order. We solved the equations numerically by using the finite difference method.

The idea behind the finite difference method is to replace the continuous computational domain by a discrete lattice of grid of points (in our case two-dimensional). Each grid point has coordinates (τ_i, σ_j) and therefore it is uniquely identified by a pair of integer numbers (i, j) . We demand that the equations of motion are satisfied at each grid point. The dependent field variables $X^A(\tau, \sigma)$ are replaced by $X^A(\tau_i, \sigma_j)$, and the derivatives are replaced by finite difference expressions based on Taylor series expansion. Our expressions for the spatial and temporal first and second derivatives use the field values of the two neighboring points in the appropriate direction. For example, the finite difference expressions

for the temporal derivatives are

$$\left(\frac{\partial X^A}{\partial \tau}\right)_{i,j} = \frac{1}{\Delta\tau_i + \Delta\tau_{i+1}} \left\{ \frac{\Delta\tau_i}{\Delta\tau_{i+1}} (X_{i+1,j}^A - X_{i,j}^A) + \frac{\Delta\tau_{i+1}}{\Delta\tau_i} (X_{i,j}^A - X_{i-1,j}^A) \right\}, \quad (\text{A.2.5})$$

$$\left(\frac{\partial^2 X^A}{\partial \tau^2}\right)_{i,j} = \frac{2}{\Delta\tau_i + \Delta\tau_{i+1}} \left\{ \frac{X_{i+1,j}^A - X_{i,j}^A}{\Delta\tau_{i+1}} - \frac{X_{i,j}^A - X_{i-1,j}^A}{\Delta\tau_i} \right\}. \quad (\text{A.2.6})$$

Here

$$X_{i,j}^A \equiv X^A(\tau_i, \sigma_j), \quad (\text{A.2.7})$$

$$\Delta\tau_i \equiv \tau_i - \tau_{i-1}. \quad (\text{A.2.8})$$

If the distance to the two neighboring points is equal the formulas (A.2.5) – (A.2.6) reduce to the well known second order centered expressions. For the spatial derivatives the formulas read

$$\left(\frac{\partial X^A}{\partial \sigma}\right)_{i,j} = \frac{X_{i,j+1}^A - X_{i,j-1}^A}{2h}, \quad (\text{A.2.9})$$

$$\left(\frac{\partial^2 X^A}{\partial \sigma^2}\right)_{i,j} = \frac{X_{i,j+1}^A - 2X_{i,j}^A + X_{i,j-1}^A}{h^2}, \quad (\text{A.2.10})$$

where h is the lattice spacing.

Figure A.1 shows three different grid points together with all its neighbors used to calculate all the derivatives. Notice the two points at the border of the zones with different grid spacing. We show different *stencils* for calculating the derivatives. We can calculate the spatial derivatives for the point (5, 5) using not the direct right neighbor (5, 6) but the neighbor having the same distance from the grid point — (5, 7). In this way we can always use the simplified formulas (A.2.9)–(A.2.10) for the spatial derivatives.

Suppose we know $X_{i,j}^A$ and $X_{i-1,j}^A$ for all j -s. After substituting the appropriate expressions into equations of motion we obtain a system of coupled quadratic equations for the unknown value $X^A(\tau_{i+1}, \sigma_j)$ for each j . These we solve numerically using the Newton-Raphson method for non-linear systems of equations

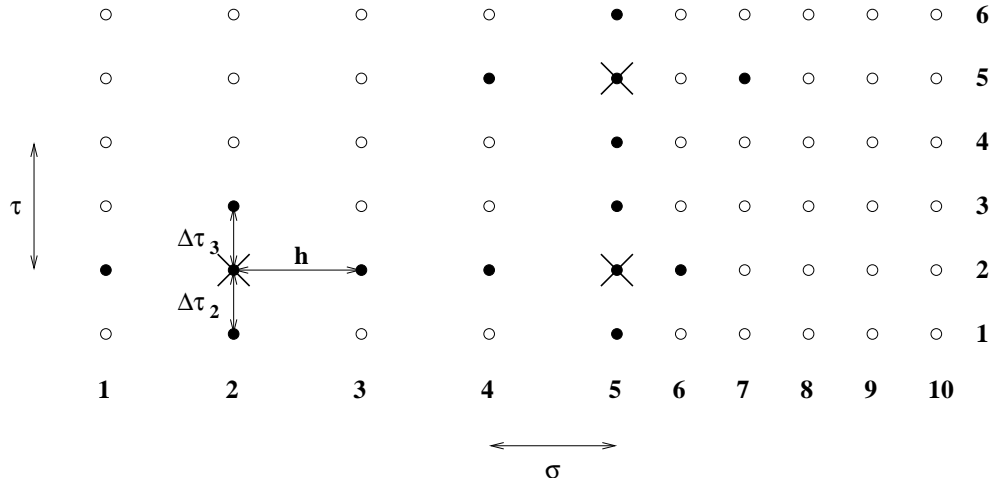


Figure A.1: An example of a (non-uniform) grid. It highlights three grid points (marked by a cross) together with all the points needed for the calculation of the derivatives (marked by full circles).

(see e.g.[52]). Repeating the whole procedure again and again we advance the solution into the future.

Since the equations for different j -s are independent this procedure is well suited for parallelization. It was implemented using the OpenMP application program interface. This is a natural choice since the algorithm is medium grained and thus not suited for the more general Message Passing Interface (MPI).

Note that we run into a problem at the first grid point since it does not have a left neighbor needed to calculate the spatial derivatives. Therefore we either prescribe certain *boundary conditions* or lose one grid point each time step. We experimented with both approaches and we chose the latter for the actual calculations. It requires a longer string segment but it does not suffer from artifacts related to the only approximate boundary conditions.

The constraint equations also play an important role in the numerical simulations. Although we do not need them to solve the equations of motion we can use

them as an indicator of the accuracy of the solution. In principle, the constraints should be satisfied at all times for all the grid points. However, since our initial conditions are not exact and due to a solution error necessarily introduced by any numerical procedure the constraints tend to be less and less satisfied as we advance the solution further. We monitor the constraints at every time step and when they exceed certain threshold we restart the solution with parameters that should reduce the solution error (e.g., we use denser grid).

A.3 Structure of the Numerical Grid

In our experimentation with the numerics we found that a uniform grid (or mesh) is not suitable for simulations of scattering with small impact parameters and relativistic velocities, especially for prograde scattering by a black hole with large angular momentum. The reason for this is that during the scattering the string develops regions with high (extrinsic) curvature (e.g., at the kinks) where the finite difference formulas might be not accurate. Also the string can numerically “stretch”, i.e., the physical distance between two neighboring points can significantly increase.

Typically, these regions constitute only small fraction of the simulated σ -domain and the rest of the string is relatively “straight”. One solution to this problem would be to increase the number of grid points thus decreasing the grid spacing. This is, however, not feasible from practical point of view — the calculation would take an incredible amount of time. Another solution is to make the grid denser only at the place where it is needed, i.e., to use a *non-uniform* mesh.

One important feature of the solution is that the critical regions are moving. This means that the mesh must be appropriately adjusted as the simulation advances. The procedure is called *adaptive mesh refinement*.

A.3.1 Mesh refinement for non-critical scattering

In our simulations we used two different adaptive techniques. First is a technique used for simulating non-critical scattering when we know the qualitative features of the solution, i.e., a kink propagating with the speed of light away from the center of the string. Figure A.2 schematically shows the structure of the grid.

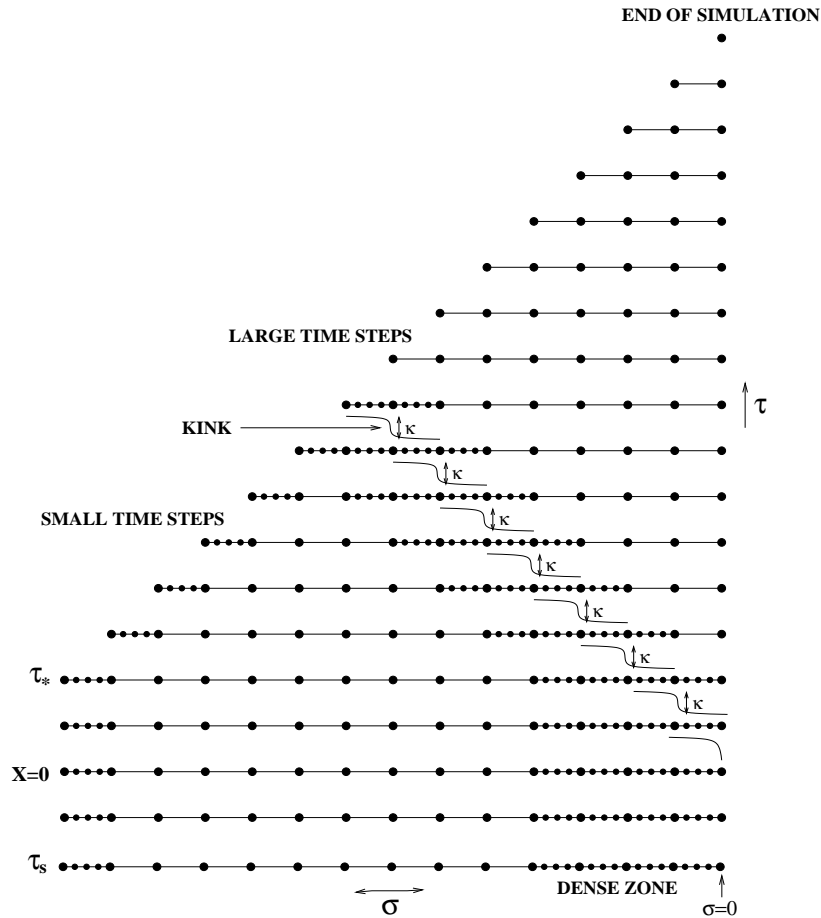


Figure A.2: Structure of the numerical grid

At the beginning of the simulation the dense zone is located at the center of the string where the kink is going to be created after the scattering at $X = 0$. The width of the dense zone is taken to be approximately twice the width of the

kink. As demonstrated in subsection 4.2.2 we can estimate the width of the kink by

$$w \approx 7 \frac{b}{v}. \quad (\text{A.3.11})$$

The density of the dense zone also depends on the width of the kink—in our simulation the ratio of the dense to the “normal” zone density ranged from 4 to 32. After the scattering we periodically monitor the position of the kink within the dense zone. As soon as it reaches a prescribed distance from the end of the dense zone we shift the dense zone toward the end of the string. Note that there is another (shorter) dense zone at the edge of the string. The purpose of this second dense zone is to prevent “cutting” off the string too quickly (every time step we lose one grid point).

Changing the grid structure involves a creation of *new* grid points. This means that we have to assign appropriate values of X^A to the newly created grid points. To do that we use cubic spline interpolation using all the points of the (old) grid. Because of the symmetry $\sigma \rightarrow -\sigma$ we know that either the first or the second derivatives with respect to σ identically vanish at $\sigma = 0$. At the leftmost end of the string we choose the “natural” spline condition, i.e., we choose the second derivatives for all X^A to vanish there.

A.3.2 Mesh refinement for capture and critical scattering

Critical scattering possess a great challenge for numerical simulation. As can be seen from figure 5.6 for certain input parameters the shape of the string can be quite complicated and the computational grid must reflect this fact. Since in this case we do not have any prior knowledge of the solution the mesh refinement algorithm must be able to adjust the grid automatically according to some well defined criteria.

Our treatment is in spirit similar to the Berger and Olinger algorithm [53].

We estimate the solution error at regular intervals and then adjust the grid accordingly. It may happen that at the “checkpoint” we find the error to be larger than a certain tolerance level. No remeshing at this point can reduce that error since the error is already there. What we need to do is to return back to the previous checkpoint and use a denser grid at places which can influence the part of the grid with the intolerable solution error. This situation certainly occurs when the string passes the black hole. Suppose that the n -th checkpoint was before the scattering occurred. At this stage our grid is relatively sparse and the error check passes without any need of remeshing. However, the $(n + 1)$ -th checkpoint occurs after the scattering when the string is distorted and stretched in the region around the center. Obviously, the estimated solution error will be very large so we restart the calculation from the position at the n -th checkpoint. This time however, we adjust the part of the mesh causally connected to the large error region. In a sense the first string pass served as a probe trying to find out what lies ahead. It may happen that even after the adjustment the solution will not pass the $(n + 1)$ -th checkpoint and the procedure will have to be repeated several times until the conditions for successful checkpoint are met.

As important as making the grid denser at regions with high solution error is the opposite process — the rarefication of the grid. This happens after a successful checkpoint at regions with the estimated solution error lower than the tolerance. In practice we introduce a limit to the process so that the distance between two adjacent grid points can not become too large.

A.3.3 Practical implementation of adaptive mesh refinement

In order to implement the adaptive mesh refinement as described in the previous subsection we have to be able to estimate the solution error. Suppose our

numerical method is second order accurate. This (roughly speaking) means that an exact solution $u(\tau, \sigma)$ can be written in terms of an approximate solution $u^h(\tau, \sigma)$ obtained from the discretized form of the equations on mesh with the grid spacing h as

$$u^h(\tau, \sigma) = u(\tau, \sigma) + h^2 e_2(\tau, \sigma) + O(h^4) . \quad (\text{A.3.12})$$

This is known as the Richardson ansatz. On coarser grid with a double spacing $2h$ we have

$$u^{2h}(\tau, \sigma) = u(\tau, \sigma) + (2h)^2 e_2(\tau, \sigma) + O(h^4) . \quad (\text{A.3.13})$$

Therefore we can estimate the solution error $e^h = u - u^h$ at a particular grid point as

$$e^h \sim u^{2h} - u^h . \quad (\text{A.3.14})$$

Once the error estimate at every (second) grid point is calculated we compare it with a prescribed tolerance level ϵ and decide whether the grid should be made denser or sparser around that point. In practice we divide the whole grid in the σ -direction into equal zones. At the beginning of the simulation the grid is uniform and each zone contains equal number of grid points (a power of 2). A zone is the smallest “chunk” of the grid we can remesh. The grid within each zone remains uniform during the whole simulation. In our approach we always increase or decrease the density of grid points by factor of 2 so that the number of grid points always remains a power of 2. Since our method is second order accurate when we double the number of grid points we expect the solution error to decrease by a factor of 4.

Suppose the error estimate at the i -th grid point is e_i . In order to achieve the prescribed accuracy the grid around the i -th grid point should be 2^{n_i} times denser (or sparser for $n_i < 0$), where n_i is defined via

$$\frac{\epsilon}{e_i} = \left(\frac{1}{4}\right)^{n_i} . \quad (\text{A.3.15})$$

Therefore

$$n_i = \frac{\log e_i - \log \epsilon}{\log 4} . \quad (\text{A.3.16})$$

Since we require n_i to be an integer we choose¹

$$n_i = \text{floor} \left(\frac{\log e_i - \log \epsilon}{\log 4} + 1 \right) . \quad (\text{A.3.17})$$

Let us now summarize the adaptive mesh refinement algorithm. It is repeated at every checkpoint. A checkpoint is invoked after we cut the last l number of zones, where²

$$l = \text{int} \left(\frac{(\Delta\sigma)_{\min}}{(\Delta\tau)_{\min}} \right) . \quad (\text{A.3.18})$$

This guarantees that a signal can travel at most one zone between two consecutive checkpoints. Here is the algorithm:

1. Calculate the solution error estimate for every second grid point using (A.3.14) and the related n_i -s using (A.3.17) .
2. Calculate the maximal n_k^{\max} and the suggested number of points N_k^s for each zone as

$$N_k^s = 2^{n_k^{\max}} N_k^{\text{old}} , \quad (\text{A.3.19})$$

where N_k^{old} is the present number of grid points in the k -th zone.

3. If all the solution errors are within the tolerance we can continue the calculation after setting

$$N_k^{\text{new}} = N_k^s \quad (\text{A.3.20})$$

4. If in some zone the solution error estimate exceeds the tolerance ϵ we must restart the calculation from a previous checkpoint. The number of grid points in each zone N_k^{new} at the restart point is chosen by the formula

$$N_k^{\text{new}} = \max(N_{k-1}^s, N_k^s, N_{k+1}^s) . \quad (\text{A.3.21})$$

¹The function floor is defined as the greatest integer less than or equal to a number.

²The function int truncates a number to the next nearest integer towards zero.

This reflects the fact that signal can propagate at most across one zone.

Every time we change the mesh structure we adjust the leftmost l zones so they have the same density as the most dense zone. This assures that we do not lose grid points too quickly. Of course, the time step is also adjusted according to the most dense zone.

A.4 Calculating κ_1 and κ_2

In subsection 4.2.1 we explained that the the dependence of the displacement parameter κ on the rotation parameter $\alpha = a/M$ can be well approximated by the quadratic formula (4.2.9). In order to calculate the κ_1 and κ_2 we must obtain the first and second order corrections $\mathcal{X}^A(\tau, \sigma)$ and $\mathcal{X}^A(\tau, \sigma)$ to the solution for the non-rotating black hole $\mathcal{X}^A(\tau, \sigma)$.

We start with the equations of motion (2.5.44)

$$\square \mathcal{X}^A + \Gamma^A{}_{BC} \left\{ -\frac{\partial \mathcal{X}^B}{\partial \tau} \frac{\partial \mathcal{X}^C}{\partial \tau} + \frac{\partial \mathcal{X}^B}{\partial \sigma} \frac{\partial \mathcal{X}^C}{\partial \sigma} \right\} = 0 \quad (\text{A.4.22})$$

and then substitute the expansions

$$\mathcal{X}^A = \mathcal{X}^A{}^0 + \alpha \mathcal{X}^A{}^1 + \alpha^2 \mathcal{X}^A{}^2, \quad (\text{A.4.23})$$

$$\Gamma^A{}_{BC} = \Gamma^A{}_{BC}{}^0 + \alpha \Gamma^A{}_{BC}{}^1 + \alpha^2 \Gamma^A{}_{BC}{}^2 \quad (\text{A.4.24})$$

into the equation (A.4.22). After grouping together terms with the same power of α we get three set of equations

$$\square \mathcal{X}^A{}^0 + \Gamma^A{}_{BC}{}^0 \left\{ -\frac{\partial \mathcal{X}^B{}^0}{\partial \tau} \frac{\partial \mathcal{X}^C{}^0}{\partial \tau} + \frac{\partial \mathcal{X}^B{}^0}{\partial \sigma} \frac{\partial \mathcal{X}^C{}^0}{\partial \sigma} \right\} = 0, \quad (\text{A.4.25})$$

$$\square \mathcal{X}^A{}^1 + \Gamma^A{}_{BC}{}^1 \left\{ -\frac{\partial \mathcal{X}^B{}^0}{\partial \tau} \frac{\partial \mathcal{X}^C{}^0}{\partial \tau} + \frac{\partial \mathcal{X}^B{}^0}{\partial \sigma} \frac{\partial \mathcal{X}^C{}^0}{\partial \sigma} \right\}$$

$$+2\overset{0}{\Gamma}{}^A{}_{BC} \left\{ -\frac{\partial \overset{0}{\mathcal{X}}^B}{\partial \tau} \frac{\partial \overset{1}{\mathcal{X}}^C}{\partial \tau} + \frac{\partial \overset{0}{\mathcal{X}}^B}{\partial \sigma} \frac{\partial \overset{1}{\mathcal{X}}^C}{\partial \sigma} \right\} = 0, \quad (\text{A.4.26})$$

$$\begin{aligned} & \square \overset{2}{\mathcal{X}}^A + \overset{2}{\Gamma}{}^A{}_{BC} \left\{ -\frac{\partial \overset{0}{\mathcal{X}}^B}{\partial \tau} \frac{\partial \overset{0}{\mathcal{X}}^C}{\partial \tau} + \frac{\partial \overset{0}{\mathcal{X}}^B}{\partial \sigma} \frac{\partial \overset{0}{\mathcal{X}}^C}{\partial \sigma} \right\} \\ & + 2\overset{1}{\Gamma}{}^A{}_{BC} \left\{ -\frac{\partial \overset{0}{\mathcal{X}}^B}{\partial \tau} \frac{\partial \overset{1}{\mathcal{X}}^C}{\partial \tau} + \frac{\partial \overset{0}{\mathcal{X}}^B}{\partial \sigma} \frac{\partial \overset{1}{\mathcal{X}}^C}{\partial \sigma} \right\} \\ & + 2\overset{0}{\Gamma}{}^A{}_{BC} \left\{ -\frac{\partial \overset{0}{\mathcal{X}}^B}{\partial \tau} \frac{\partial \overset{2}{\mathcal{X}}^C}{\partial \tau} + \frac{\partial \overset{0}{\mathcal{X}}^B}{\partial \sigma} \frac{\partial \overset{2}{\mathcal{X}}^C}{\partial \sigma} \right\} \\ & + \overset{0}{\Gamma}{}^A{}_{BC} \left\{ -\frac{\partial \overset{1}{\mathcal{X}}^B}{\partial \tau} \frac{\partial \overset{1}{\mathcal{X}}^C}{\partial \tau} + \frac{\partial \overset{1}{\mathcal{X}}^B}{\partial \sigma} \frac{\partial \overset{1}{\mathcal{X}}^C}{\partial \sigma} \right\} = 0, \quad (\text{A.4.27}) \end{aligned}$$

The equation (A.4.25) is just the equation of motion for a string moving in a Schwarzschild spacetime. Note that the remaining two equations (A.4.26) and (A.4.27) are linear in $\overset{1}{\mathcal{X}}^A$ and $\overset{2}{\mathcal{X}}^A$, respectively.

In practical implementation we solve the equations in the order they were written. First we advance the solution for $\overset{0}{\mathcal{X}}^A$ one step. After that we are able to calculate all the derivatives of $\overset{0}{\mathcal{X}}^A$ entering the equations (A.4.26). After a discretization we are left with four linear equations for the four unknown $\overset{1}{\mathcal{X}}^A_{i+1,j}$ at each grid point j . We solve them using the LU decomposition method (see e.g. [52]). Similarly, after substituting the derivatives of $\overset{0}{\mathcal{X}}^A$ and $\overset{1}{\mathcal{X}}^A$ into (A.4.27) we obtain a system of linear equations for $\overset{2}{\mathcal{X}}^A_{i+1,j}$.

The initial conditions for $\overset{0}{\mathcal{X}}^A$ are chosen as always using the weak field approximation. We set the initial two time levels for $\overset{1}{\mathcal{X}}^A$ and $\overset{2}{\mathcal{X}}^A$ to be zero. This is reasonable since at far distances the angular momentum plays almost no role.

A.5 Obtaining the Real-time Profiles

Throughout the thesis we show various pictures of string profiles. Typically, we present the string configurations taken at a constant coordinate time T . In this section we discuss how we obtain the string configurations.

In the conformal gauge the worldsheet time-like parameter τ does not coincide with T . Therefore we can not simply take a “snapshot” of the string at certain value of the parameter τ but we must “gather” the grid points with constant T over many time steps. Moreover, the structure of the mesh is changing and the calculation can be restarted so the whole procedure is not completely trivial.

The strategy is as follows. The gathering begins when certain prescribed conditions are met. At that point we find the grid point with the minimum coordinate time T_{save} at time level 1. We use arrays $\text{AS}(1 : N_{\text{max}})$, $\text{AX}(1 : 3, 1 : N_{\text{max}})$ to store the string configuration³ The value of the σ parameter is stored in AS, and the X, Y, Z coordinates corresponding to that particular σ are stored in AX. A pointer P always points to the last filled position in the arrays. In the consequent time steps we compare the time coordinates T_1 and T_2 corresponding to the time levels 1 and 2, respectively, with T_{save} . If for some grid point $T_2 < T_{\text{save}} \leq T_1$ we store the values of σ and the coordinates X, Y, Z (after linear interpolation). Figure A.3 schematically shows the situation.

The gathering procedure ends when the coordinate time T at all the grid points is greater than T_{save} . However, we can not save the string configuration until we pass the next checkpoint since the calculation can be restarted. In general, when we successfully pass a checkpoint we validate all the points gathered thus far. This is done simply by saving the position of the last gathered point in a variable PVAL, i.e., $\text{PVAL} = \text{P}$. If, at a successful checkpoint, the gathering is finished we call the procedure which processes the arrays and saves the

³ N_{max} represents the largest number of points we expect to store during the simulation.

string configuration into a file. If, on the other end, the checkpoint is not successful and the calculation is restarted, we discard all the points which have not been validated yet and continue the gathering. This is done simply by setting $P = PVAL$.

In practice the situation is a little bit more complicated since it can happen that we want to start to gather points for another coordinate time T'_{save} while we are still in the process of gathering points for T_{save} . Therefore we add one more dimension to all the participating variables that indexes the concurrent active gatherings. The index is circular and its dimension restricts the number of concurrent active gatherings.

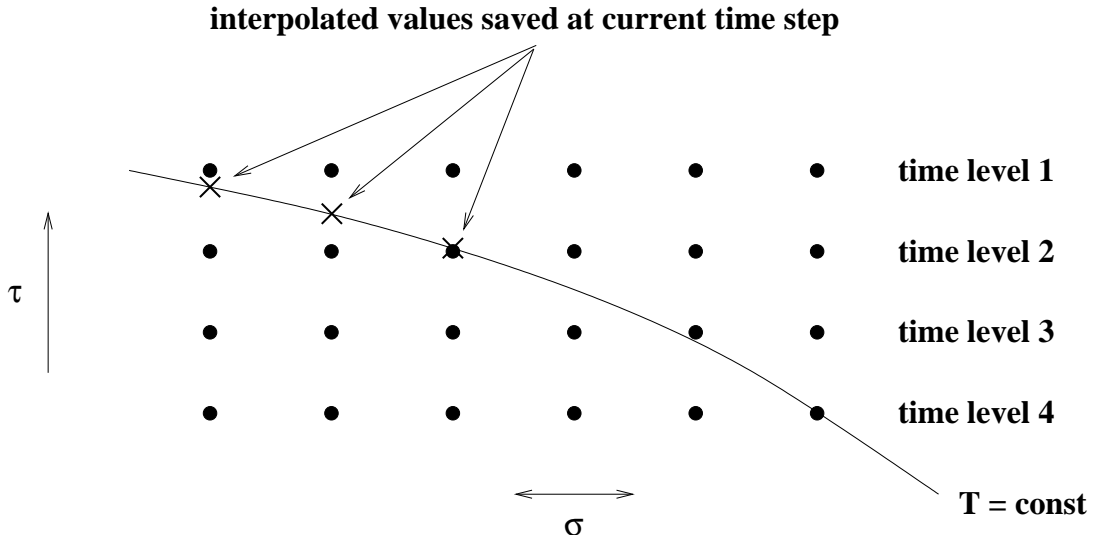


Figure A.3: Part of the numerical grid showing the $T = T_{save} = \text{const}$ line and the points stored in AS and AX at this time step.

Let us now describe how we process the arrays once the gathering is done. First of all we sort the array AS. The sorting procedure produces an index file which is then used for sorting AX. At this point we could simply save the arrays

into a file and be done with it. However, we do not need to save all the data when we just want to show the string profile. This would unnecessarily waste a lot of disk space and the data processing would be slow. We need to save only enough points to realistically picture the string profile. In particular, the task is to choose such points that, when connected by lines, realistically represent the string profile. It is intuitively clear that we need fewer points at places where the string is relatively straight and more points where the string twists and turns. We implemented the following algorithm (the number referencing a particular point is its index in the sorted AS array).

1. Set $NL = 1$ and $NR = 3$, save the first point.
2. Calculate the (Euclidean) distance from all the points $NL + 1, \dots, NR - 1$ to the line connecting the points NL and NR .
3. If the distance of some of the points exceeds a threshold value d we save the $(NR - 1)$ -th point, set $NL = NR - 1$, $NR = NL + 2$ and go to point 2.
4. If the distance from all points is less than d then we set $NR = NR + 1$ and go to point 2
5. Repeat until we reach the last point which we always save.

The smaller the parameter d the better the string profile is approximated but more points is saved.

Figure A.4 schematically shows part of the string before and after the application of the algorithm.

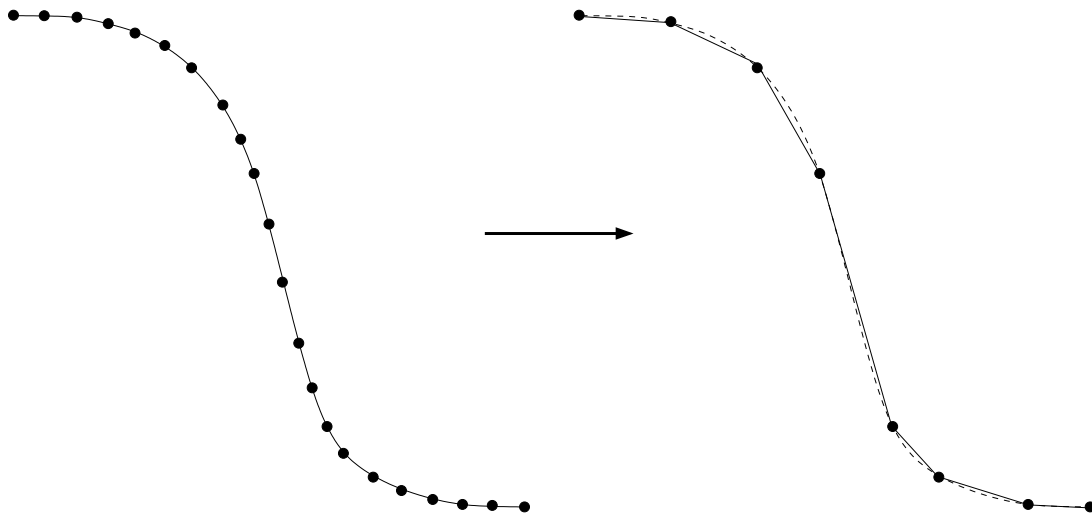


Figure A.4: The left profile represents a part of the string with all the grid points while the right profile represents the approximation with smaller number of grid points. In reality, of course, the string has a three-dimensional structure.

Appendix B

Spherically-Symmetric Solutions of D'Alambert Equation

A solution of the $(n + 1)$ -dimensional D'Alambert equation

$$\square^{(n+1)}p = f \quad (\text{B.0.1})$$

can be written by using a retarded Green's function

$$\square^{(n+1)}G_{n+1}^{ret}(x, x') = -\delta^{(n+1)}(x - x'). \quad (\text{B.0.2})$$

We assume that in the infinite past there were no incoming waves. The solution $p(x)$ is then completely generated by the external 'force' $f(x)$,

$$p(x) = - \int G_{n+1}^{ret}(x, x') f(x') dx'. \quad (\text{B.0.3})$$

The Green's function for odd $n = 2\nu + 1$, $\nu \geq 1$, can be written as [54]

$$G_{n+1}^{ret}(x, x') = \frac{(-1)^{\nu-1} \vartheta(t - t')}{(2\pi)^\nu} \left[\frac{d^{\nu-1}}{(RdR)^{\nu-1}} \delta((t - t')^2 - R^2) \right], \quad (\text{B.0.4})$$

where $R = |\mathbf{x} - \mathbf{x}'|$. For our convenience, we rewrite it in a slightly different form

$$G_{n+1}^{ret}(x, x') = \frac{\vartheta(t-t')}{2\pi^\nu} \left[\frac{d^{\nu-1}}{d\alpha^{\nu-1}} \delta(\lambda + \alpha) \right]_{\alpha=0}. \quad (\text{B.0.5})$$

Here

$$\lambda = (t-t')^2 - |\mathbf{x} - \mathbf{x}'|^2, \quad (\text{B.0.6})$$

$$|\mathbf{x} - \mathbf{x}'|^2 = \rho^2 + \rho'^2 - 2\rho\rho'z, \quad z = \cos\theta, \quad (\text{B.0.7})$$

and θ is the angle between n -dimensional vectors \mathbf{x} and \mathbf{x}' .

We are interested in spherically symmetric solutions of D'Alambert equation. Integrating over the angular variables we get

$$\hat{G}(t, \rho; t', \rho') = \Omega_{n-2} \int_{-1}^1 dz (1-z^2)^{(n-3)/2} G_{n+1}^{ret}(t, \rho; t', \rho'; z), \quad (\text{B.0.8})$$

where $\Omega_k = 2\pi^{\frac{k+1}{2}}/\Gamma(\frac{k+1}{2})$ is a volume of a k -dimensional unit sphere S^k . Here we made explicit that G_{n+1}^{ret} depends on the angle variables only through the parameter z .

Let us denote

$$F = \rho^\nu f, \quad P = \rho'^\nu p. \quad (\text{B.0.9})$$

Then in the absence of incoming waves the spherically symmetric solution of the equation (B.0.1) is

$$P(t, \rho) = - \int dt' d\rho' \mathcal{G}(t, \rho; t', \rho') F(t', \rho'), \quad (\text{B.0.10})$$

where

$$\mathcal{G}(t, \rho; t', \rho') = (\rho'\rho)^\nu \hat{G}(t, \rho; t', \rho'). \quad (\text{B.0.11})$$

Let us show that for odd n the representation (B.0.4) allows one to obtain the Green's function for this reduced equation. The reduced Green's function \mathcal{G} can be written as

$$\mathcal{G}(t, \rho; t', \rho') = \vartheta(t-t') \frac{(\rho'\rho)^\nu}{\Gamma(\nu)} B, \quad (\text{B.0.12})$$

where

$$B = \left[\frac{d^{\nu-1}}{d\alpha^{\nu-1}} \int_{-1}^1 dz (1-z^2)^{\nu-1} \delta(b(z+z_*)) \right]_{\alpha=0}, \quad (\text{B.0.13})$$

$$\lambda_0 = (t-t')^2 - \rho^2 - \rho'^2, \quad b = 2\rho\rho', \quad z_* = \frac{\lambda_0 + \alpha}{b}. \quad (\text{B.0.14})$$

By calculating the integral in (B.0.13) one gets

$$B = B_+ - B_-, \quad (\text{B.0.15})$$

$$B_{\pm} = \frac{1}{b} \left[\frac{d^{\nu-1}}{d\alpha^{\nu-1}} \left\{ (1-z_*^2)^{\nu-1} \vartheta(z_* \pm 1) \right\} \right]_{\alpha=0}. \quad (\text{B.0.16})$$

Now let us note that if any of the derivative over α is acting on the ϑ -function, the result vanishes because of the remaining factor $1-z_*^2$. Using Rodrigues' formula for Legendre polynomials ([55], relation 22.11.5)

$$P_n(x) = \frac{(-1)^n}{2^n n!} \frac{d^n}{dx^n} [(1-x^2)^n], \quad (\text{B.0.17})$$

one obtains

$$B_{\pm} = \vartheta(\lambda_{\pm}) \frac{(-2)^{\nu-1}}{b^{\nu}} (\nu-1)! P_{\nu-1}(\lambda_0/b), \quad (\text{B.0.18})$$

where

$$\lambda_{\pm} = (t-t')^2 - (\rho \mp \rho')^2. \quad (\text{B.0.19})$$

Combining the above expressions we obtain the following representation for the reduced Green's function

$$\mathcal{G}(t, \rho; t', \rho') = C_{\nu} P_{\nu-1} \left(\frac{\lambda_0}{b} \right) [\vartheta(\lambda_+) - \vartheta(\lambda_-)], \quad (\text{B.0.20})$$

where

$$C_{\nu} = \frac{(-1)^{\nu-1} (\nu-1)!}{2\Gamma(\nu)}. \quad (\text{B.0.21})$$

For $\nu = 1$, which corresponds to a $n = 3$ brane we have

$$p(t, \rho) = -\frac{1}{2} \int dt' d\rho' \frac{\rho'}{\rho} f(t', \rho') [\vartheta(\lambda_+) - \vartheta(\lambda_-)]. \quad (\text{B.0.22})$$

A similar procedure can be applied for the case of even n , i.e., odd number of spacetime dimensions. The expressions are more complicated, and we will not discuss them here.

Bibliography

- [1] A. Vilenkin and E. P. S. Shellard, *Cosmic Strings and Other Topological Defects*. (Cambridge Univ. Press, Cambridge) (1994).
- [2] L. A. Kofman and A. D. Linde, Nucl. Phys. **B282**, 555 (1987).
- [3] A. D. Linde and A. Riotto, Phys. Rev. **D56**,1841 (1997).
- [4] P. Binétruy, C. Deffayet and P. Peter, Phys.Lett. **B441**, 52 (1998).
- [5] L. Pogosian and T. Vachaspati, Phys. Rev. **D60**,083504 (1999).
- [6] C. R. Contaldi, E-print astro-ph/0005115 (2000).
- [7] N. Simatos and L. Perivolaropoulos, Phys. Rev. **D63**, 025018 (2001).
- [8] M. Landriau and E. P. S. Shellard, E-print astro-ph/0208540 (2002).
- [9] F. R. Bouchet, P. Peter, A. Riazuelo and M.Sakellariadou, Phys. Rev. **D65**, 021301 (2002).
- [10] J. Kormendy, L.C. Ho, E-print astro-ph/0003267 (2000).
- [11] J. Kormendy, E-print astro-ph/0306353 (2003).
- [12] J.A. Orosz, E-print astro-ph/0209041 (2002).
- [13] Roeland P. van der Marel, E-print astro-ph/0302101 (2003).

- [14] M. Snajdr, V.P. Frolov, and J.P. De Villiers, *Class. Quant. Gravity* **19**, 5987 (2002).
- [15] M. Snajdr and V.P. Frolov, *Class. Quant. Gravity* **20**, 1303 (2003).
- [16] V.P. Frolov, M. Snajdr and D. Stojkovic, E-print gr-qc/0304083 (2003), accepted for publication in *Phys. Rev. D*.
- [17] S. Lonsdale and I. Moss, *Nucl. Phys.* **B298**, 693 (1988).
- [18] J.P. De Villiers and V.P. Frolov, *Int. J. Mod. Phys.* **D7** No. 6, 957 (1998).
- [19] J.P. De Villiers and V.P. Frolov, *Phys. Rev.* **D58**, 105018(8) (1998).
- [20] D.N. Page, *Phys. Rev.* **D58**, 105026(13) (1998).
- [21] J.P. De Villiers and V.P. Frolov, *Class. Quant. Gravity* **16**, 2403 (1999).
- [22] D.N. Page, *Phys.Rev.* **D60**, 023510 (1999).
- [23] V.A. Rubakov, M.E. Shaposhnikov, *Phys. Lett.* **B125**, 136 (1983).
- [24] C. W. Misner, K.S. Thorne and J.A. Wheeler, *Gravitation*. (W.H. Freeman, San Francisco) (1973).
- [25] A.M. Polyakov, *Phys Lett.* **B103**, 207 (1981).
- [26] E.W. Kolb, M.S. Turner, *The Early Universe*. (Addison-Wesley Publishing Company) (1990).
- [27] E.N. Parker, *Ap.J.* **160**, 383 (1970).
- [28] A. H. Guth, *Phys rev.* **D23**, 347 (1981).
- [29] A. D. Linde, *Phys. Lett.* **B108**, 389 (1982).
- [30] P.J.E. Peebles and J.T. Yu, *Ap.J.* **162**, 815 (1970).

- [31] W. Hu and N. Sugiyama, Ap.J. **444**, 489 (1995).
- [32] W. Hu and M. White, Phys. Rev. Lett. **77**, 1687 (1996).
- [33] P. de Bernardis, *et al*, Nature **404**, 995 (2000).
- [34] S. Hanany, *et al*, Ap.J. **545**, L5 (2000).
- [35] N.W. Halverson, *et al*, Ap.J. **568**, 38 (2002).
- [36] H. Thirring and J. Lense, Phys. Z. **19**, 156(1918).
- [37] V.P. Frolov, I.D. Novikov, *Black Hole Physics: Basic Concepts and New Developments*. (Kluwer Academic Press) (1998).
- [38] A.V. Frolov and A.L. Larsen, Class.Quant.Grav. **16** 3717 (1999).
- [39] V.P. Frolov, D. Stojkovic, Phys. Rev. Lett. **89**, 151302 (2002).
- [40] V.P. Frolov, D. Stojkovic, Phys. Rev. **D66** 084002 (2002).
- [41] N. Arkani-Hamed, S. Dimopoulos and G. Dvali. Phys. Lett. **B429**, 263 (1998).
- [42] E.G. Adelberger, E-print hep-ex/0202008 (2002).
- [43] G. Landsberg, E-print hep-ph/0211043 (2002).
- [44] S. Dimopoulos and G. Landsberg, Phys. Rev. Lett. **87** 161602, (2001).
- [45] S.B. Giddings and S. Thomas, Phys. Rev. **D65**, 056010 (2002).
- [46] D. Stojkovic, Phys. Rev. **D67**, 045012 (2003).
- [47] V.P. Frolov and A.L. Larsen, Nucl.Phys. **B449**, 149(1995).
- [48] V.P. Frolov, S. Hendy and A.L. Larsen, Phys.Rev. **D54**, 5093 (1996).

- [49] M.W. Choptuik, Phys. Rev. Lett. **70**, 9 (1993).
- [50] M. Christensen, V.P. Frolov and A.L. Larsen, Phys.Rev. **D58**, 085008 (1998).
- [51] V.P. Frolov, A.L. Larsen and M. Christensen, Phys.Rev. **D59**, 125008 (1999).
- [52] W.H. Press, S.A. Teukolsky, W.T. Vetterling and B.P. Flannery, *Numerical Recipes in Fortran. The Art of Scientific Computing*. (Cambridge Univ. Press, 2nd ed.) (1992).
- [53] M.J. Berger and J. Olinger, J. Comp. Phys. **53**, 484 (1984).
- [54] D. Galtsov, Phys. Rev. **D66**, 025016 (2002).
- [55] M. Abramowitz and I. A. Stegun, *Handbook of Mathematical Functions* (Dover Publ. Inc., New York) (1972).